Spring 2019

Development of LiDAR assisted terrestrial radar interferometry for rock deformation monitoring

Ricardo Javier Romero Ramirez

DEVELOPMENT OF LIDAR ASSISTED TERRESTRIAL RADAR INTERFEROMETRY FOR ROCK DEFORMATION MONITORING

by

RICARDO JAVIER ROMERO RAMÍREZ

A DISSERTATION

Presented to the Faculty of the Graduate School of the

MISSOURI UNIVERSITY OF SCIENCE AND TECHNOLOGY

In Partial Fulfillment of the Requirements for the Degree

DOCTOR OF PHILOSOPHY

in

GEOLOGICAL ENGINEERING

2019

Approved by

Norbert Maerz, Advisor
Neil L. Anderson
J. David Rogers
Jeffrey D. Cawlfield
J. Erik Loehr

To my Family

ABSTRACT

Rock and soil slope movements cost millions of dollars annually. During the past few decades, engineers have relied on traditional methods to detect slope movements. These tools are valuable for small spatial areas but, may not be adequate or cost effective for large spatial areas. Remote sensing methods such as terrestrial laser scanning (TLS) and terrestrial radar interferometry (TRI) provide excellent spatial coverage, and with adequate post-data-processing software, sub-millimetric scale deformation sensitivity can be achieved.

This work will present a comparative experimental study between TLS and TRI. The comparative experimental study will allow us to achieve the two main objectives of this research: 1. The development of a methodology to correct repositioning errors of the TRI during discontinuous measurement campaigns. 2. The development of a methodology to use TLS as an independent measurement device to constrain the results of the TRI when rock displacements exceed multiple wavelengths of the instrument or displacements exceed one quarter of the wavelength of the instrument.

Results from the measurement campaigns show that sub-millimetric displacements can be detected with both TLS and TRI systems. Furthermore, TLS systems are widely available, cheaper, lighter, and easier to operate than TRI systems. Data can also be reduced faster, and the results more easily interpreted than with TRI systems. These advantages make TLS systems ideal for rock slope evaluation for highway projects, especially when time, cost, and public opinion are major concerns for the state's Department of Transportation.

ACKNOWLEDGMENTS

I am very grateful to my research advisor, Dr. Norbert Maerz, for his advice and patience in sharing his knowledge and support through my doctoral studies at Missouri S&T.

I also wish to acknowledge my colleagues: Benjamin Hill, Chengxun Lu, Ruiyang Zhang, Denise Mathews, Javad Galinmoghadam, and especially Kenneth Boyko, for sharing his knowledge on terrestrial laser scanning and post-processing algorithms.

I would also like to express my sincere appreciation to the other members of my graduate committee: Dr. Neil Anderson, Dr. J. David Rogers, Dr. Jeffrey D. Cawlfield, and Dr. J. Erik Loehr.

I would also like to acknowledge the Puerto Rico Highway Authority for granting me a leave of study.

Finally, special thanks to my family for their patience, understanding, and support during my doctoral studies.

TABLE OF CONTENTS

Page

LIST OF ILLUSTRATIONS

Figure Page

LIST OF TABLES

1. INTRODUCTION

Rock and soil slope movements cost local departments of transportation millions of dollars annually. In addition, slope movements can cause loss of private property and in some cases loss of human life. During the past few decades, geotechnical and geological engineers have relied on traditional methods to detect slope movements, such as traditional survey tools (total stations), inclinometers, extensometers, etc. These tools are valuable for small spatial areas, but may not be adequate or cost effective for large spatial areas. Remote sensing methods such as terrestrial laser scanning (TLS) and terrestrial radar interferometry (TRI) provide excellent spatial coverage, and with adequate post-data-processing software, sub-mm scale deformation sensitivity can be achieved.

This work will present a comparative experimental study between TLS and TRI. To accomplish this objective, steel targets of different sizes will be constructed and mounted on a rock displacement simulator (RDS) capable of simulating sub millimetric rock movements. The Leica Scan Station of the Missouri University of Science and Technology (Missouri S&T) and the Gamma Portable Ground Interferometric Radar (GPIR) of the University of Missouri at Columbia (MU) will be the main equipment for this study. The comparative experimental study will allow us to achieve the two main objectives of this research: 1. The development of a methodology to correct repositioning errors of the TRI during discontinuous measurement campaigns; and 2. The development of a methodology to use TLS as an independent measurement device to constrain the results of the TRI when rock displacements exceed multiple wavelengths of the instrument or displacements exceed one half of the wavelength of the instrument.

1.1. PROBLEM STATEMENT

According to Rosenblad et al. (2016), detecting sub-mm scale movements of objects is a difficult measurement problem and one that is important for geotechnical applications. The authors used TLS to measure movements of boulders on a site previously surveyed with TRI. They found that TLS could detect cm scale movements, but it was unable to detect millimeter scale movements.

On the other hand, Maerz et al. (2016) have been able to measure sub-mm movements using TLS in conjunction with proprietary post-processing software developed at Missouri S&T. Their research shows that movements as little as 0.3 mm can be detected with the appropriate equipment and software.

Wujanz et al (2013) pointed out that even when the precision of TRI systems can be assumed to be less than 1 mm, such precision cannot be attained during discontinuous measurements campaigns. The authors mentioned two reasons responsible for this problem: 1. The dependence of TRI on a single standpoint; and 2. The problem of solving ambiguities when displacements exceed half the wavelength ($\lambda/2$) of the instrument.

From the findings of the authors mentioned above, and from the findings of several researchers which will be presented in the next section, more research is needed to evaluate the capabilities of TLS and TRI to detect precursory rock movements. This work will shed some light on the use of both TLS and TRI for detecting precursory rock movements. Finally, it will present a methodology to overcome some of the problems of TRI during discontinuous measurement campaigns, and when displacements exceed multiple wavelengths or exceed half the wavelength of the instrument.

1.2. OBJECTIVES

The specific objectives of this research are the following:

- To construct target plates of various sizes, and to mount them on a rock displacement simulator, developed at Missouri S&T, capable of simulating sub-mm scale movements of rocks.
- To perform TLS and TRI measurements in a controlled environment using target plates of various size. We propose to use mine adits in Springfield, MO, to achieve a very controlled environment in order to avoid errors from atmospheric conditions.
- To compare TLS and TRI measurements to determine their accuracy in detecting sub-mm scale movements of rocks. The TLS data will be post-processed with the proprietary Missouri S&T LiDAR software developed by Boyko (2014).
- To install a compact TLS on the TRI to acquire additional data during discontinuous measurement campaigns.
- To use the compact TLS data into the post-processing TRI software in order to overcome its single standpoint problem and to solve ambiguities when rock displacements exceed multiple wavelengths or exceed one half the wavelength of the TRI.

1.3. RESEARCH QUESTIONS

The research at hand intends to answer the following questions:

- Can TLS detect sub-mm movements of rocks?

- Does the post processing Missouri S&T LiDAR software give a better accuracy of rock movements?
- Can TRI detect sub-mm movements of rocks?
- Do TLS and TRI measurements correlate with ground truth data?
- Can the compact TLS data be used to overcome the single standpoint problem of the TRI?
- Can the compact TLS data provide additional information to help solve ambiguities when rock displacements exceed multiple wavelengths or exceed one half the wavelength of the TRI?

1.4. RESEARCH HYPOTHESIS

Since the TRI method has a theoretical finer resolution than the TLS (sub mm), and does not require special targets like the TLS does to achieve its finest resolution, and since the TRI method has difficultly related to repositioning and measuring movements greater than one half the wavelength of the instrument, could TLS measurements be used to calibrate the TRI method when repositioning and in identifying the approximate range of the target to a resolution of less than the ambiguity range of one half the wavelength of the TRI?

2. LITERATURE REVIEW

TLS and TRI are becoming increasingly useful in the fields of geological and civil engineering, to which the problem of deformation analysis is associated. The last two decades have been dominated by TLS, which can be used to obtain high-density digital elevation models (DEM), and to detect precursory rock movements from small- to medium-range distances (less than 300 m). During the last decade, attempts have been made to use TRI in the field of deformation monitoring to extend the capabilities of TLS to long-range distances (up to 5 km). Although great developments have been made during the last two decades with regard to measurements using both TLS and TRI scanning methods, room for improvement still exists. This section presents a state of the art review of TLS and TRI used in geological and civil engineering applications to detect or predict precursory rock movements.

2.1. TLS AND TRI TECHNOLOGY: STATE OF THE ART

In 2005, Rosser et al. presented a methodology to monitor the coastal cliff erosion process using TLS. Their methodology allowed the quantification of failures, ranging in scale from the detachment of blocks of a few centimeters in dimension through to large rock, debris, falls, slides, and flows over 1000 m^3. TLS allowed the authors to collect data on-site in a fast way and hence was a cost-effective method, which provided a detailed description of the process of coastal cliff erosion.

Lingua et al. (2008) carried out measurements using both TRI and TLS in order to assess the hazard of a quarry in Baveno in the Italian Alps that is subject to ground instabilities. The equipment used by the authors is shown in Figures 2.1 and 2.2. The

authors claimed that continuous monitoring using TRI can achieve sub-millimetric accuracy (± 0.70 mm). However, in the case of interrupted measurement campaigns, it was not possible for the authors to reach sub-millimetric accuracy due to phase decorrelation. On the other hand, the TLS technique allowed accurate measurements during interrupted campaigns of the monitored area. Furthermore, TLS scans taken at different times can be used to compute volume changes of the observed rock or soil mass, which provides 3D displacement measurements, while TRI scans can only detect displacements parallel to the line of sight of the instrument. The authors concluded that integration of TRI and TLS can be a powerful tool for remote monitoring of slopes.

Figure 2.1. The GB-InSAR instrument used by Lingua et al. (2008).

Figure 2.2. The Riegl LMS-Z420 terrestrial laser scanner used by Lingua et al. (2008).

Alba et al. (2008) used TRI to measure deformations of an arch-gravity dam. The TRI used in their study is named IBIS-L and is shown in Figure 2.3. They compared the displacement measured with a "coordinatometro" (Italian for reference card or Romer) installed on the central section of the dam (see Figure 2.4) to the measurement obtained from the TRI. The authors found that TRI-measured displacements were within ±1 mm of the readings from a "coordinatometro". However, the authors recommended further experimental and theoretical research in the field of TRI.

Figure 2.3. TRI, named IBIS-L, installed on a concrete foundation and used by Alba et al. (2008).

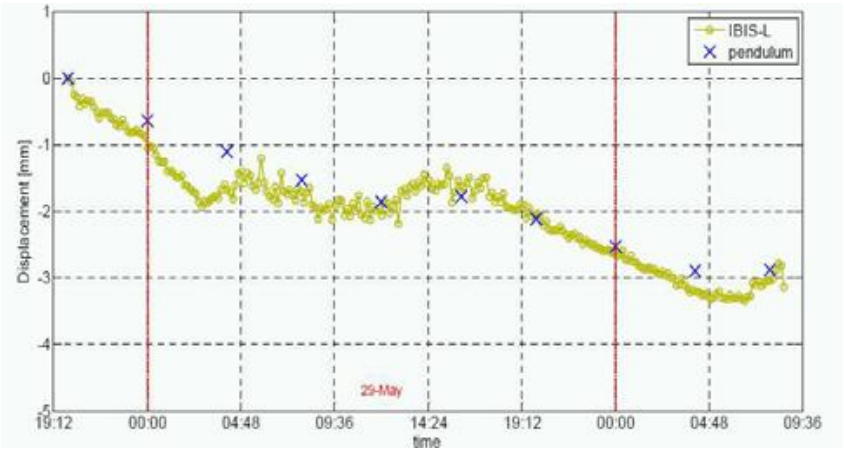

Figure 2.4. TRI single pixel displacement (green circles) on the middle of the dam crest, compared to a "coordinatometro" measurements observation (from Alba et al., 2008).

Abellán et al. (2009) performed an experiment to determine whether the TLS instrumental error was small enough to detect millimetric displacements. This consisted of ground truth displacements of three objects (see Figure 2.5). The authors found that millimetric changes cannot be detected by the analysis of unprocessed TLS point cloud

data. However, by applying the nearest neighbor (NN) averaging technique to the TLS point cloud data, displacement measurements were improved considerably, reducing the error (1σ) up to a factor of 6. The NN technique was applied to a rockfall event at Castellfollit de la Roca, Spain. The authors showed that precursory millimetric displacements can be detected using TLS by applying the NN averaging method. The authors recommended more research on the detection of precursory displacements at different ranges and for variable displacement directions.

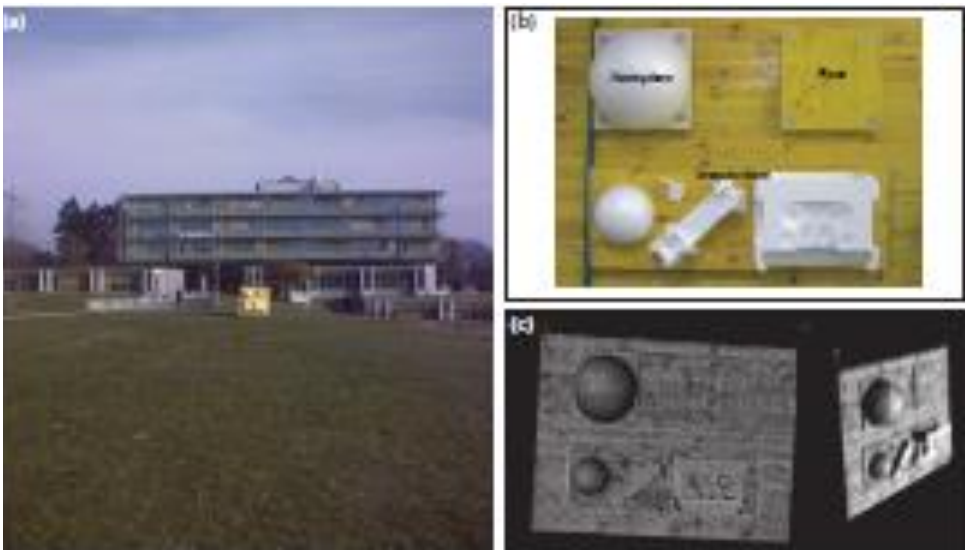

Figure 2.5. (a) Experimental setup at 50 m, (b) Close up of the scanned area showing the three moving objects, and (c) Perspective views of the TLS point cloud (from Abellán et al., 2009).

Tapete et al. (2013) integrated TRI and TLS to obtain three-dimensional interferometric radar point clouds to evaluate the displacements affecting archeological monuments. The authors carried out measurements of targets located in the central

archeological area of Rome, Italy. The site and the equipment used by the authors are shown in Figure 2.6. The TRI used in the tests was the Lisamobile, which is manufactured by LiSALab. On the other hand, the TLS used in their study was the RIEGL LMS-Z420i. The integration of both scanners (TRI and TLS) provided useful information about the stability of the archeological structures. The authors recommended future research on the use of the TRI for modelling the structural behavior of the monitored surfaces in order to predict stresses and finally to plan appropriate countermeasures.

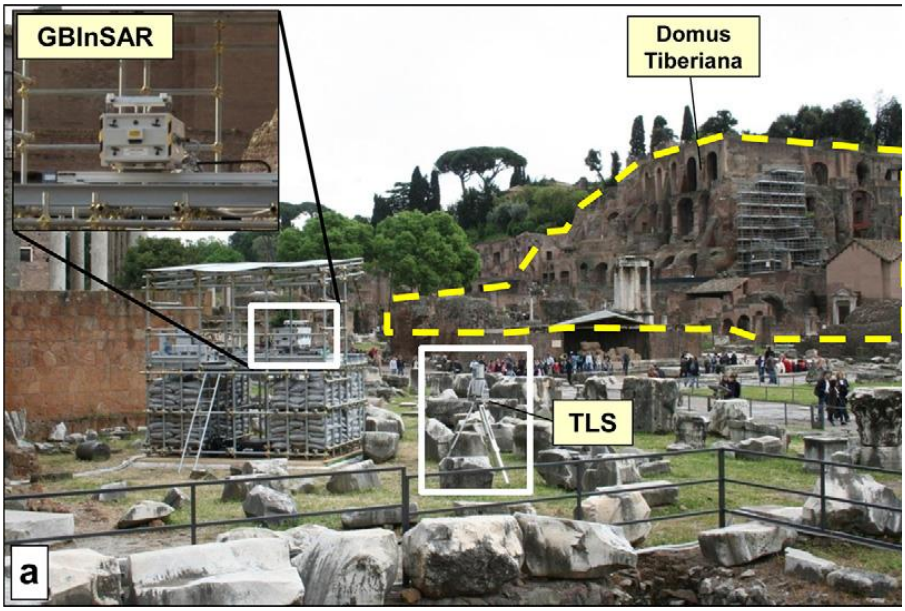

Figure 2.6. The TRI mounted on a platform, with view centered on the Domus Tiberiana site, and the TLS (from Tapete et al., 2013).

Wujanz et al. (2013) carried out a comparative experimental study between TRI and TLS. According to the authors, a major limitation of TRI is the comparison of data collected at different measurements campaigns. The two main reasons for this problem are:

1. The dependence of radar techniques on a certain standpoint; and 2. The issue related to solving ambiguities when deformations exceed half of the wavelength of the instrument. The equipment used in their study is shown in Figure 2.7. The authors carried out their experiment in a quarry where topographic changes were deliberately made. These changes produced false results during the phase unwrapping process. The authors concluded that TRI alone cannot be used for deformation monitoring due to ambiguities. In order to solve this problem, the authors introduced TLS data into the TRI post-processing software. They called this methodology assisted Ground Based Radar (aGBRadar). The authors conclude their paper by recommending more research of the procedure and expansion of their methodology to distances larger than 45 m.

Figure 2.7. To the left is the TLS and to the right is the TRI used by Wujanz et al. (2013).

Jenkins (2013) performed a study using a TRI manufactured by Gamma at a site of previous major rockfall events located in Glenwood Canyon, Colorado. The site and the

equipment used by the author are shown in Figure 2.8. Measurements were performed over two-week intervals for a duration of about 6 weeks. The results from this study appeared to show no movements occurring over this time span. However, the findings regarding the capabilities of the GBIR were inconclusive since it was not known if movements were occurring at the site. The author recommended to perform more measurements at sites where reliable ground truth data is available.

Figure 2.8. Rock slope in Glenwood Canyon, CO, (center) and GBIR (left) (from Jenkins, 2013).

Crosetto et al. (2014) stated in their paper that TRI offers a convenient deformation monitoring tool, and it has been implemented in the past to monitor dams, landslides, subsidences, glaciers, volcanoes, avalanches, and snow. According to the authors, sub-millimetric displacements of good targets can be detected. However, TRI measurements are largely affected by the configuration method used during measurement campaigns. The

most common method used in measurement campaigns is the continuous mode, where the TRI is installed and left on site during the entire campaign. This method has the lowest impact on the measurements. The other method used in measurements campaigns is the discontinuous mode, where the TRI is removed from the site and installed again when revisiting the site of interest. This method of taking TRI measurements has a high impact on data quality.

Monserrat el al. (2014) presented a review of TRI systems. The authors explained that TRI is based on the concept of a coherent radar system, which measures both the amplitude and the phase of the received radar signal. When applying interferometric techniques to the phase measurements, deformation of the measured scene can be obtained. TRI is advantageous because it is very sensitive to small displacements, its range is in the order of kilometers, and it has the ability to obtain a relatively large number of deformations. On the other hand, TRI is ambiguous to large displacements, which can be problematic for discontinuous mode measurement campaigns.

Caduff et al. (2015) carried out a review of the use of TRI for the detection of surface mass movement. The authors described several TRI systems and data acquisition methodologies. Some radar sensors use real aperture and other use synthetic aperture for radar image formation. Some case studies were presented to illustrate applications in TRI for displacement detection. In general, detection of very slow (mm to cm per year) displacements in rock walls to very fast (~50 m per year) displacements of mass movements has been documented.

Kromer et al. (2015) presented an algorithm to post-process TLS point cloud data. According to the authors, the algorithm has the capability to detect displacements at the

sub-mm scale, which can be used to study precursory rock movements. The authors implemented the algorithm in synthetic and experimental cases. The results indicated that an improvement of one order to two orders of magnitude in the level of displacement detection can be achieved compared to existing point cloud techniques.

Daud and Abdullah (2016) conducted an accuracy assessment using TLS, airborne light detection and ranging (ALiDAR), and TRI. ALiDAR data elevation accuracy was between 15 to 20 cm, while TRI elevation accuracy was between 5 to 10 m. Based on their results, the authors concluded that TLS has better accuracy when compared to ground truth data rather than ALiDAR and TRI.

Rosenblad et al. (2016) presented observations from recent studies of the application of TRI to diverse slope stability issues. The authors presented three cases: 1. Continuous short-term monitoring of a slow-moving landslide; 2. Periodic monitoring of a potential rockfall site; and 3. A controlled study simulating detection of precursory rock movements. In the first case, the average moving rate was approximately 50 cm per month and movements as small as 0.5 mm were detected using TRI. The second case consisted of detecting small and localized movements within a rock face. However, the authors were no able to discern small and localized movements of rocks within a rock slope using TRI. The third case consisted of a controlled study to evaluate the capability of TRI to detect movements of individual boulders in a landscape to detect precursory rock movements. Boulders ranging from 0.5 to 5 m were moved using pry bars and airbag jacks in increments of a few to several mm. Two identical TRI scanners were used to scan a region covering approximately 20,000 m^2 after each boulder movement. Ground truth measurements were also performed after each boulder movement. The results from this third case study showed

that displacements of boulders larger than 2 m were detectable for range offset distances from about 75 to 150 m. Displacements as small as 1.7 mm were measured on these larger boulders. Based on these results, the authors concluded that the ability to detect movements of boulders less than 2 m in nominal dimension was inconclusive in their study.

Maerz et al. (2016) presented a TLS scanning approach to determine the slip surface as well as measuring the extent and direction of small slip movements. They mounted spherical targets on rigid rods driven to the ground placing the targets above the vegetation (see Figure 2.9). In addition, the use of two spherical targets on each rod was used to measure rotation of the target rods, thus giving insight into the nature of the below grade failure. To increase the accuracy of measurement, the authors repeated the measurement multiple times and computed an average of all observations. The authors used this principle to achieve sub-mm precision with TLS data. Their results showed the ability of TLS to measure movements of as little as 0.3 mm based on temporal scanning.

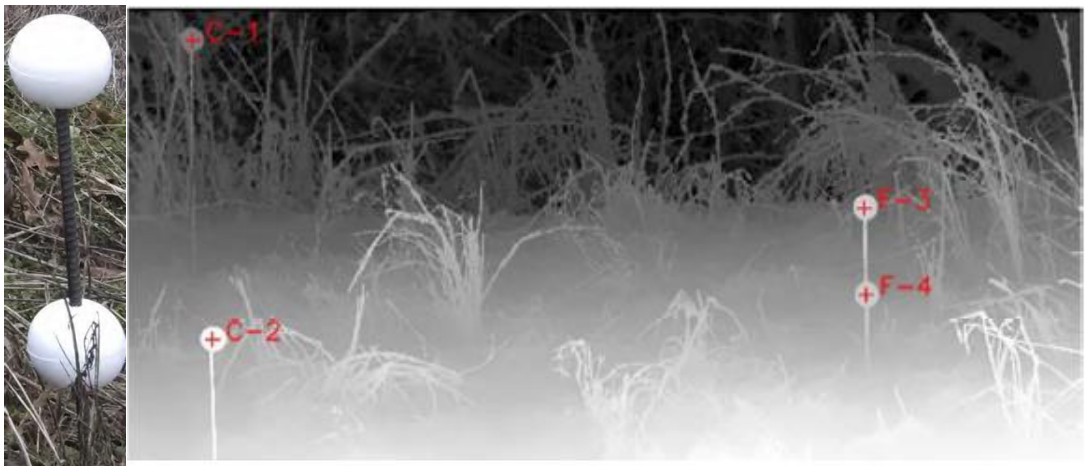

Figure 2.9. Rebars driven into the ground with 100 mm Styrofoam balls (from Maerz et al., 2016).

Intrieri et al. (2016) monitored a rockslide located at Cantoniera in Vetto Municipality (Reggio Emilia Province, Central Italy) by means of a TRI and a TLS in order to monitor its displacements and to provide both an early warning system and a feedback for the restoration works. The radar furnished near real-time displacement maps that were integrated with 3D models of the slope reconstructed through the laser scanner. The integration between the two techniques permitted the reconstruction of a high-resolution 3D displacement map of the rockslide also in the areas where profiling works created disturbance to radar data.

Kromer et al. (2017) developed an automated TLS system capable of detecting deformations in near real-time. Their system is shown in Figure 2.10 and was named automated terrestrial laser scanning (ATLS). The main purpose of the ATLS was to provide a high temporal resolution alternative to TRI. Their ATLS was light, portable, and less expensive than available TRI. In order to evaluate the capacities of their ATLS, the authors carried out a six-week measurement campaign on the Séchilienne Landslide in France. During the measurement campaign, the authors detected flux of talus and precursory rock displacements. The accuracy of the ATLS was between 2 to 10 mm at distances greater than 1000 m. The authors concluded that their system can be used effectively to monitor landslides and rockfall processes at high levels of temporal resolution.

2.2. SUMMARY

As presented in the previous section, more research is needed to evaluate the accuracy of TLS in conjunction with post-processing software to detect sub-millimetric precursory movements of rocks. Also, more research is needed to evaluate the feasibility of TRI to detect sub-millimetric precursory movements of rocks with facial dimensions

smaller than 2 m, to evaluate the feasibility of TRI for campaign-wise deformation monitoring, and to detect movements greater than one half the wavelength of the instrument.

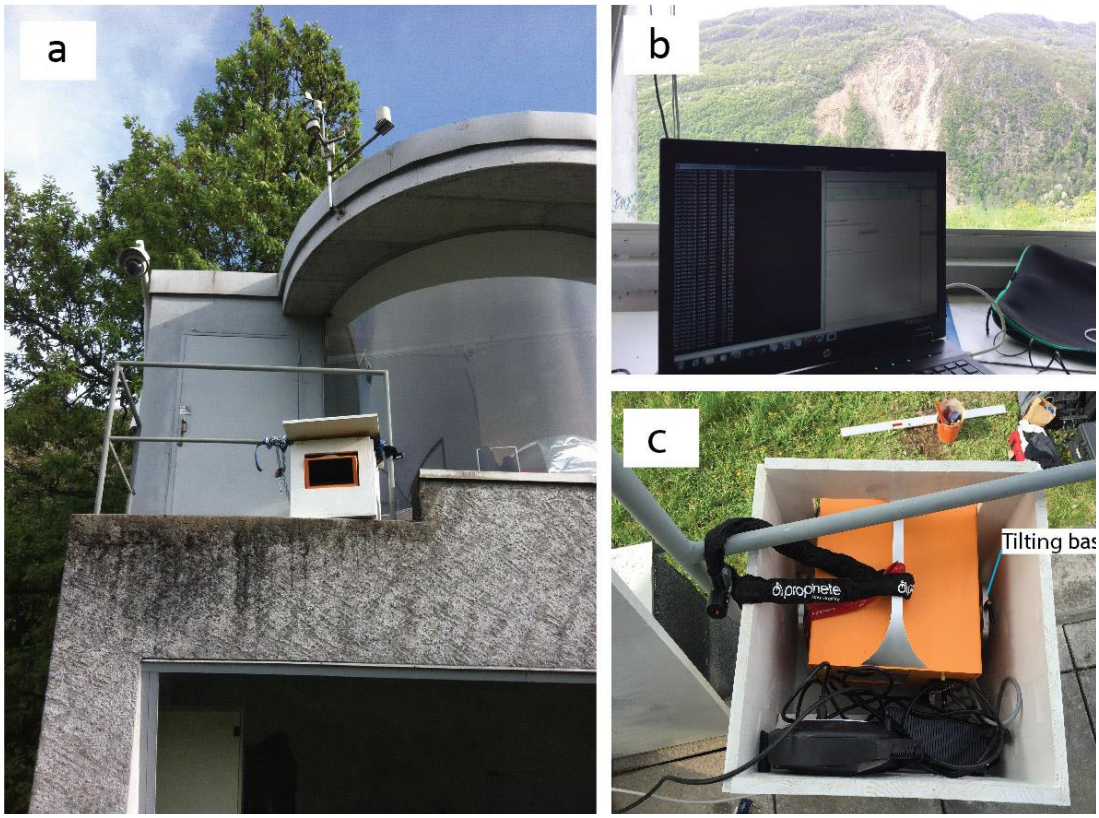

Figure 2.10. Automated TLS system which consisted of: (a) A TLS system encased in a protective housing which was installed on a roof; (b) A laptop installed inside a room; and (c) TLS tilting base and battery backup installed inside the protective housing (from Kromer et al., 2017).

3. RADAR BACKGROUND

According to Richards (2014) the word “radar” was originally an acronym, RADAR, for radio detection and ranging”. Radar was developed by many nations for military use before and during World War II. Radar systems are so common today that the acronym lost its capitalization and became an English noun.

This section will present the main components of radar systems, their basic principles of operation, and data interpretation. The intent is to give geological engineers and civil engineers with majors in geotechnical engineering a fundamental understanding of radar concepts that will be utilized in this study.

3.1. BASIC RADAR CONCEPTS

Richards et al. (2010) explain that a radar is a device capable of transmitting electromagnetic (EM) waves toward a point in space and capable of detecting these electromagnetic waves when they are reflected from that point in space. The main components of a radar system (see Figure 3.1) are the following: a transmitter, an antenna, a receiver, and a signal processing unit. The component that generates EM waves is the transmitter. The antenna is the component that takes the EM waves generated by the transmitter and propagates them through the environment to the target. The transmitter is connected to the antenna through a component called a T/R device. The T/R device has two functions: 1. It provides a simultaneous connection of the receiver and the transmitter to the same antenna; and 2. It protects the receiver of the high-powered transmitted signals. The propagated EM wave induces currents on the target, generating and radiating secondary EM waves. Some of these secondary EM waves reach the antenna and are

captured by the receiver component, which is connected to the antenna. The subcomponents of the receiver amplify the received signal, convert the received signal to an intermediate frequency (IF), convert the signal from analog form to digital form (A/D), and finally relay the signal to the processor. The detector, shown in Figure 3.1, is the subcomponent of the receiver that removes the carrier from the modulated received signal in a way that data from the target can be analyzed by the signal processor.

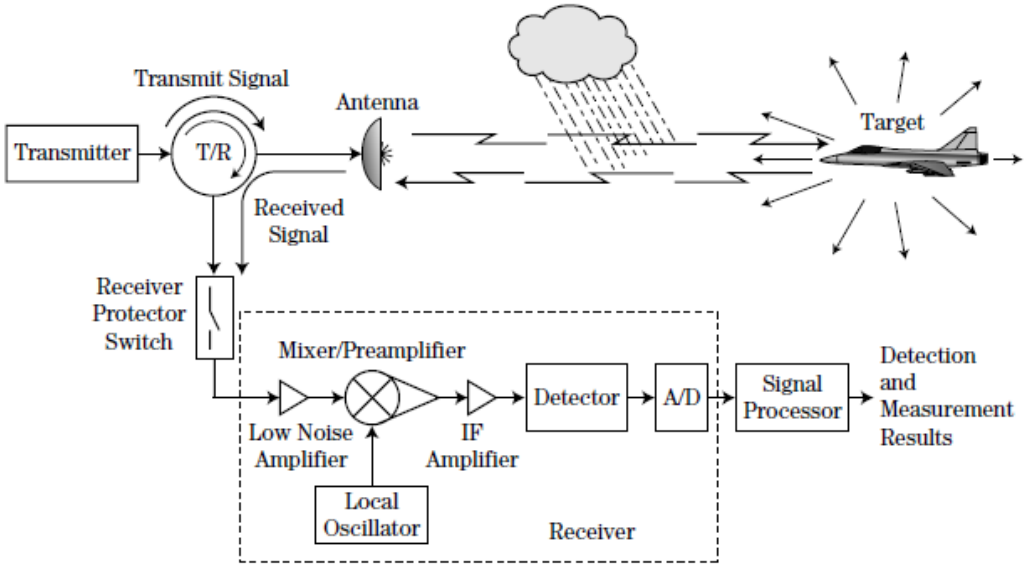

Figure 3.1. Major elements of the radar transmission/reception process (Richards et al., 2010).

As explained above, radar systems are very sophisticated devices that can be used to detect a target of interest. Some of the applications of radars are the following: target tracking, target imaging, target classification, and determining the target range distance (R) between the radar and an object. This is accomplished by using the speed of light

(c~3x10^{8}m/s) and measuring the two-way travel time of the radar signal (ΔT). The equation to calculate the range distance is:

$$R = \frac{c\Delta T}{2}. \quad (3.1)$$

3.1.1. Electromagnetic Waves. The concept of electromagnetic (EM) waves was introduced in the previous section without a former description of this concept, which is important to understand how radar systems work. Richards et al. (2010) define EM waves as electric and magnetic field waves that oscillates at a given frequency. The electric, ***E***, field is in one plane, and the magnetic, ***B***, field is perpendicular to the ***E***, field. EM waves propagate through space perpendicular to the plane described by the ***E*** and ***B*** fields. In Figure 3.2, the ***E*** field is defined along the *y*-axis, the ***B*** field along the *x*-axis, and the direction of propagation of EM waves along the *z*-axis.

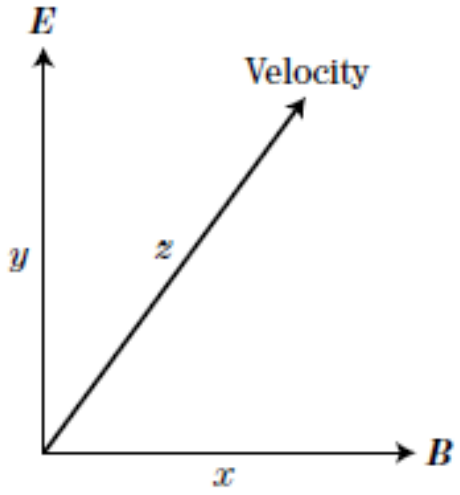

Figure 3.2. Orientation of the electric and magnetic fields and their velocity vector (Richards et al., 2010).

The amplitude of a wave is a measure of its change over time. The amplitude of the *x* or *y* component of the electric field (***E***) of an electromagnetic wave (EM) propagating along the *z*-axis can be expressed as

$$E = E_o cos(kz - \omega t + \phi) \tag{3.2}$$

where E_o is the peak amplitude, and ϕ is the initial phase.

The wave number, *k*, and the angular frequency, ω are related by

$$k = \frac{2\pi}{\lambda} \text{ radians/m}, \qquad \omega = 2\pi f \text{ radians/sec} \tag{3.3}$$

where λ is the wavelength in meters, and *f* is the frequency in hertz.

3.1.2. Wavelength. According to Richards et al. (2010), the amplitude of the electric field (***E***), of a linearly polarized electromagnetic wave propagating in space and measured at a single point in time, has a sinusoidal shape as shown in Figure 3.3. The points on the sinusoid can be computed by holding *t* constant in Equation (3.2) and varying *z*. The distance from any point on the sinusoid to the next corresponding point (i.e., peak to peak or trough to trough) is known as the wavelength, λ, of the wave, as shown in Figure 3.3.

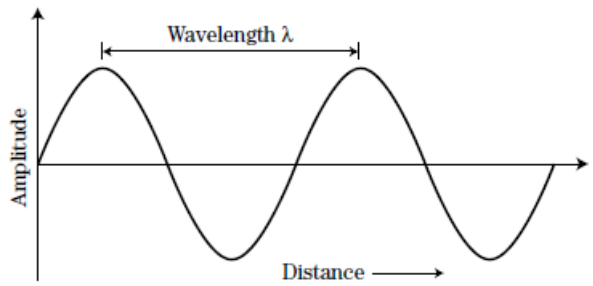

Figure 3.3. The wavelength of a sinusoidal electromagnetic wave (Richards et al., 2010).

3.1.3. Frequency. Richards et al. (2010) explain that if a fixed point in space is selected and the amplitude of the electric field is observed as a function of time at the selected point, the result will be a sinusoid as a function of time as shown in Figure 3.4. Any point on the sinusoidal curve can be computed by holding *z* constant in Equation (3.2) and letting *t* vary. The time from any point on the sinusoid to the next corresponding point (i.e., peak to peak or trough to trough) is known as the wave period, T_0. In other words, the period is the time it takes an electromagnetic wave to go through one cycle. The inverse of the period is known as the wave's frequency, *f*, and it represents the number of cycles the electromagnetic wave travels in one second. Frequency can be expressed mathematically as

$$f = \frac{1}{T_o}. \tag{3.4}$$

Frequency is expressed in hertz; 1 Hz equals one cycle per second.

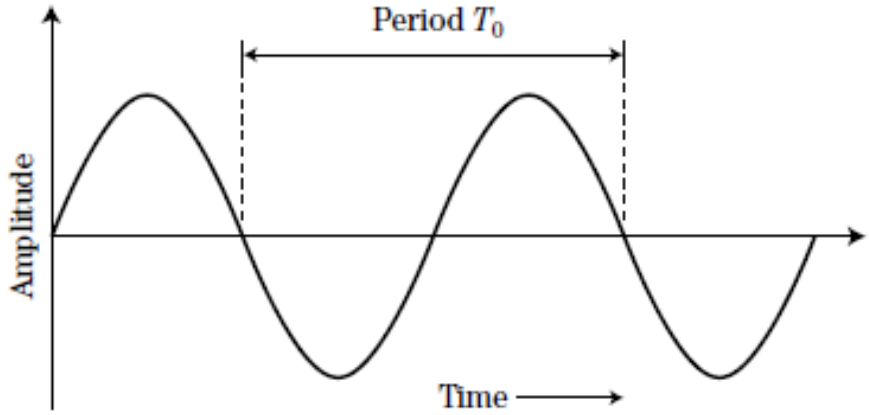

Figure 3.4. The period of a sinusoidal electromagnetic wave (Richards et al., 2010).

The product of wavelength and frequency of an electromagnetic wave is known as the speed of light, *c*, and can be expressed mathematically as:

$$\lambda f = c\,. \tag{3.5}$$

Different types of electromagnetic waves as a function of frequency are shown in Figure 3.5. As can be seen in Figure 3.5, radar bands are defined between 3 MHz to 300 GHz. According to Richards et al. (2010), most radars operate between 300 MHz and 35 GHz. The wavelengths of the radar bands shown in Figure 3.5 were calculated using Equation 3.5 and are shown in Table 3.1.

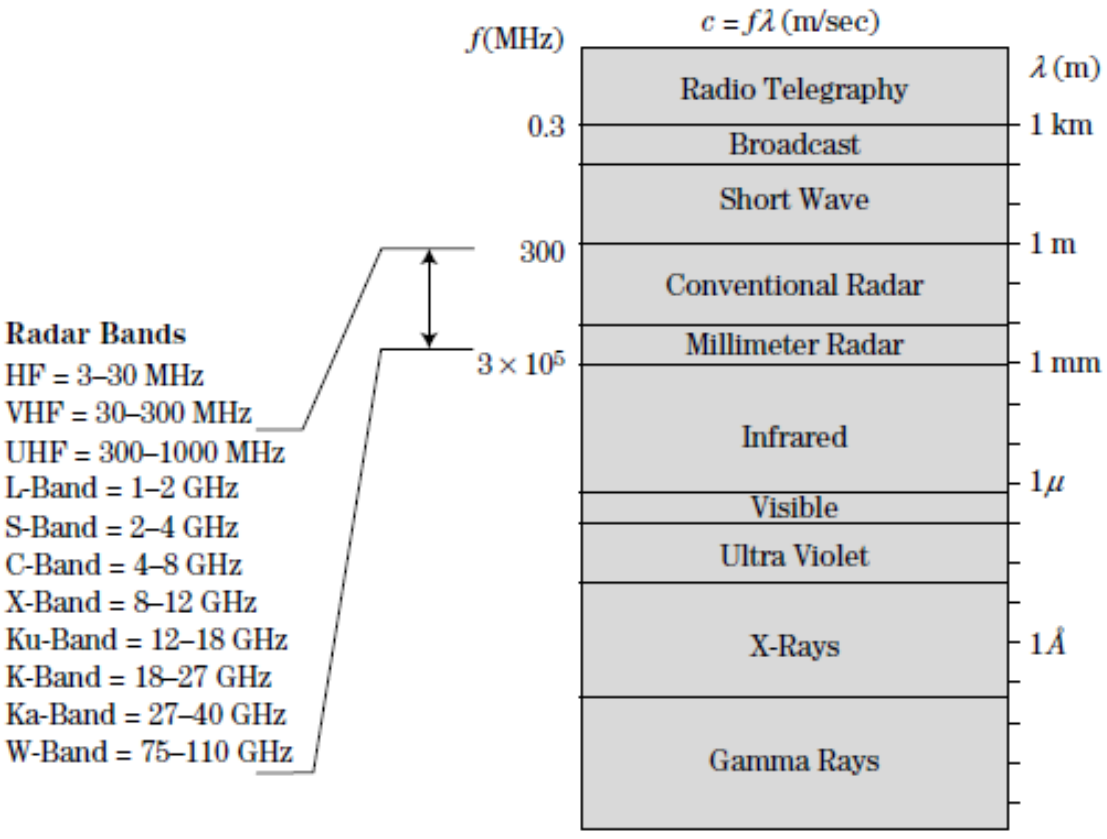

Figure 3.5. Electromagnetic wave types (Richards et al., 2010).

Table 3.1. Radar Bands designation for different microwave frequencies and corresponding wavelengths.

Band	**Frequency Range**	**Wavelength Range**
High frequency (HF)	3 – 30 MHz	100m – 10 m
Very high frequency (VHF)	30 – 300 MHz	10m – 1m
Ultra high frequency (UHF)	300 MHz – 1 GHz	1 m – 0.3 m
L	1 – 2 GHz	30 cm – 15 cm
S	2 – 4 GHz	15 cm – 7.5 cm
C	4 – 8 GHz	7.5 cm – 3.75 cm
X	8 – 12 GHz	3.75 cm – 2.5 cm
Ku (“under” K-band)	12 – 18 GHz	2.5 cm – 1.67 cm
K	18 – 27 GHz	1.67 cm – 1.11 cm
Ka (“above” K-band)	27 – 40 GHz	1.11 cm – 0.75 cm
V	40 – 75 GHz	7.5 mm – 4 mm
W	75 – 110 GHz	4 mm – 2.73 mm
mm	110 – 300 GHz	2.73 mm – 1 mm

3.1.4. Phase. Richards et al. (2010) pointed out that the variable ϕ in Equation 3.2 is commonly known as the initial phase, and it depends on the initial conditions of the electric field. If the electric field (E) is zero at both time (t) and distance (z) zero, then $\phi = \pm\pi/2$ radians. On the other hand, the phase of an electromagnetic wave is the argument of the cosine function, $kz - \omega t + \phi$, and it depends on position (z), time (t), and initial conditions.

The relative phase of an electromagnetic wave is defined as the phase difference between two waves. Two electromagnetic waves are in phase when their phase difference is zero. However, the two electromagnetic waves can become out of phase if the travelled length is different. Two electromagnetic waves out of phase by $\Delta\phi/\omega$ seconds are shown in Figure 3.6.

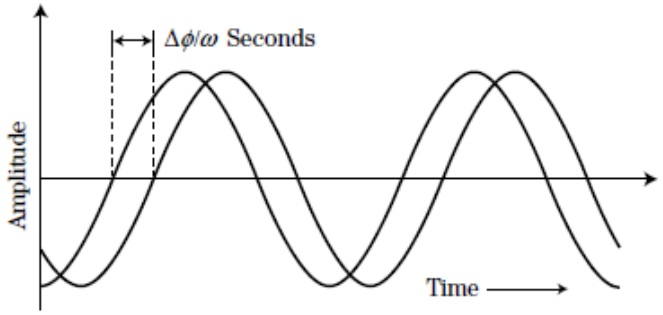

Figure 3.6. Two waves with the same frequency but a phase difference $\Delta\phi/\omega$ (Richards et al., 2010).

3.1.5. Superposition. Richards et al. (2010) define superposition as the complex sum of two or more electromagnetic waves that have the same frequency and are present at the same place and time in space. Two superposition cases can occur: 1. Construction interference is when two in-phase waves produce a wave having an amplitude that is the sum of each wave; and 2. Destructive interference, which occurs when two out-of-phase waves produce a resultant wave with an amplitude less than the sum of the two amplitudes. As a matter of fact, two electromagnetic waves that have the same amplitude but are out of phase by π radians (180^o) will produce a null wave.

3.1.6. Intensity. Intensity, *Q*, of an electromagnetic wave is defined by Richards et al. (2010) as the power per unit area of the propagating wave. Let us consider an isotopically radiating source (antenna) emitting an electromagnetic wave of power *P* in all directions as shown in Figure 3.7. The wave front in this case will be a sphere, and any point along the wave front will have the same amplitude and same power. We can define the wavelength, λ, as the distance between concentric spheres. Then, we can mathematically express the intensity, *Qt*, as:

$$Q_t = \frac{P_t}{4\pi R^2} \tag{3.6}$$

where *R* is the distance from the isotropic source. We can see in Equation 3.6 that the intensity of an electromagnetic wave decay is $1/R^2$.

If the electromagnetic waves are far away from the isotropically radiating source, then the spherical waves can be approximated as planar wave fronts, as shown in Figure 3.7. If the curvature of the wave front is less than $\lambda/16$ over a given area of dimension *D*, then the wave can be considered planar. This condition is usually met if the distance from the radiating source to the target is at least $2D^2/\lambda$. This is known as the far-*field* approximation.

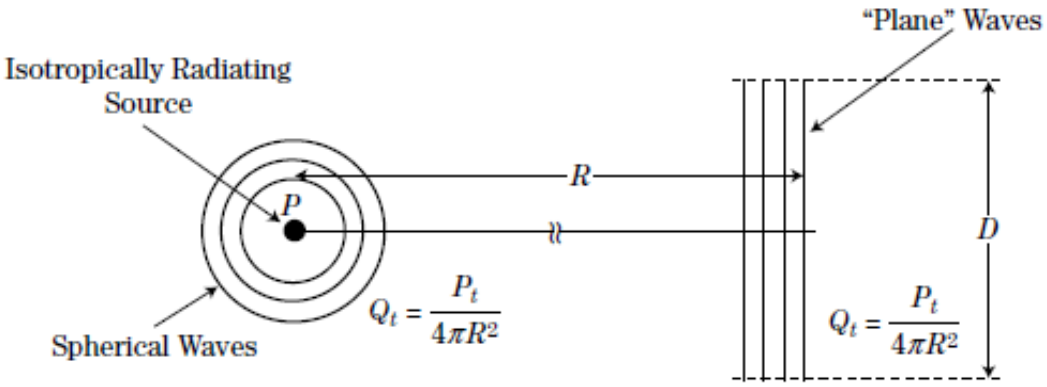

Figure 3.7. Intensity of spherical waves (Richards et al., 2010).

3.1.7. Basic Radar Configurations and Waveforms. Richards et al. (2010) mention two types of radar antenna configuration: 1. Bistatic where one antenna is used to transmit electromagnetic waves and another antenna is used to receive the backscattered wave; and 2. Monostatic where one antenna is used to transmit electromagnetic waves and

receive the backscattered wave. The two types of radar antenna configuration are shown in Figure 3.8. The presence of two antennas in a radar system does not classify the system as monostatic or bistatic. Radar systems constructed with two very close antennas can be considered monostatic. Radar systems are only considered bistatic if the antennas are far apart from each other.

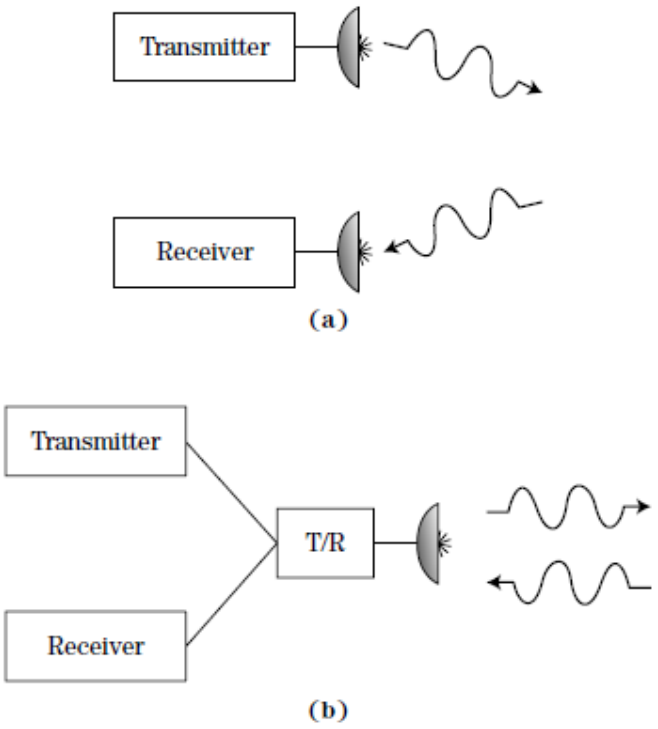

Figure 3.8. Radar antenna configurations: a. Bistatic, and b. Monostatic (Richards et al., 2010).

As can be seen in Figure 3.9, radar waveforms can be divided into two general classes: continuous wave (CW) and pulsed. In the CW case the radar transmitter is continually radiating an electromagnetic wave, and the radar receiver is continually

receiving the backscattered wave. In the pulsed case the radar transmitter emits pulses of finite duration. When the transmitter is turned off, the radar receiver is turned on and backscattered waves can be detected.

Another type of radar waveform is Frequency Modulated-Continuous Wave (FM-CW). According to Jenkins (2013), FM-CW systems operate by using a linear modulation technique, where the operating frequency of the radar is swept over a certain range. FM-CW devices perform well at close ranges where the reflected signal is received during transmission of the signal. These systems typically use a bistatic antenna configuration.

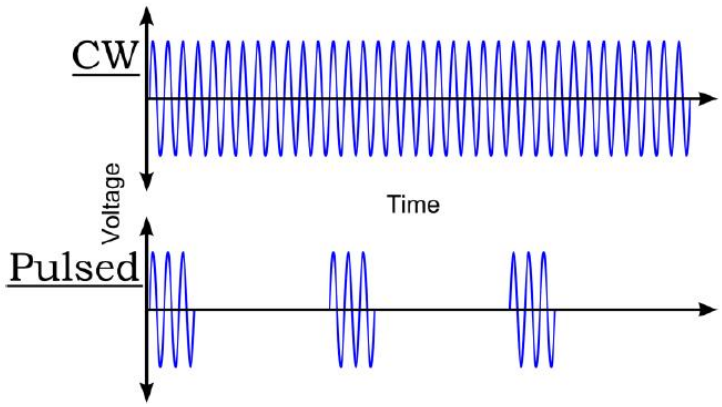

Figure 3.9. Continuous wave (CW) versus pulsed (Davis, 2011).

3.1.8. Radar Main Lobe and Beamwidth. According to Richards et al. (2010), most radar antennas emit electromagnetic waves in patterns known as lobes. Depending on the radiating direction and strength of the electromagnetic wave, they are known as the main lobe or main beam, side lobe, and back lobe. The different types of lobes are shown in Figure 3.10. The main lobe is the lobe that contains the higher power. Side lobes are

usually unwanted electromagnetic radiation that propagates in undesired directions. Radiation emitted towards the back of the antenna is within the back lobe. Beamwidth is the angle between the points on the main lobe where the power has fallen to half (-3 dB) of its maximum value. As shown in Figure 3.11, beamwidth is usually expressed in degrees for a horizontal plane.

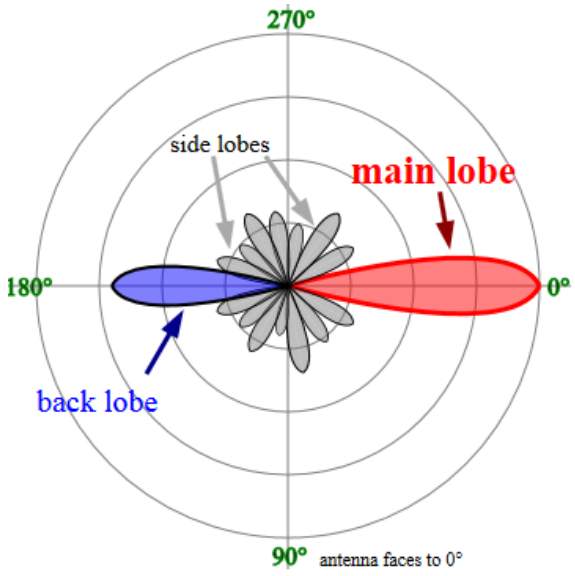

Figure 3.10. Polar antenna radiation diagram. The radial distance from the center represents signal strength (Truckle, 2008).

3.1.9. Radar Measurements. Once a target has been detected by a radar system, its position in cartesian space (x_o,y_o,z_o) must be specified, as shown in Figure 3.12. This can be determined by knowing the azimuth, θ, and the elevation angle, ϕ, measured from the antenna main beam when the target is detected. The distance between the target and

the antenna, R, can be determined by the two-way travel time of the electromagnetic wave as discussed in Section 3.2.

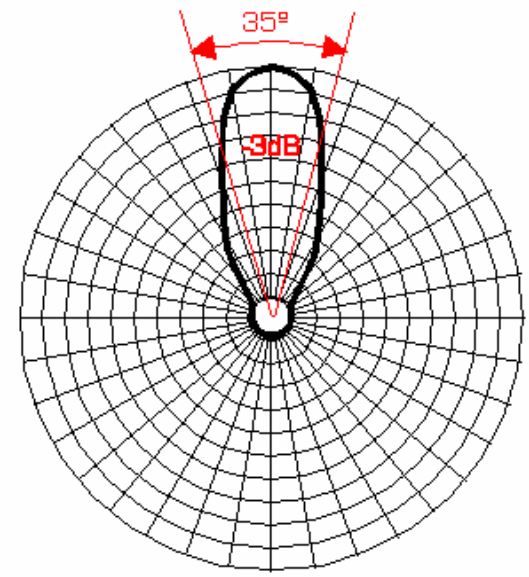

Figure 3.11. Polar diagram showing beamwidth (Hoeksma, 2007).

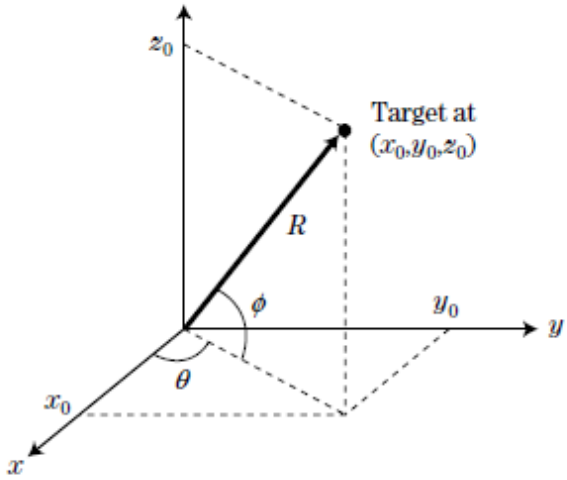

Figure 3.12. Spherical coordinate system used to specify target position (Richards et al., 2010).

3.1.10. Resolution. Richards (2014) defines range resolution as the capability of a radar system to distinguish two or more targets that are closely positioned in space. Figure 3.13.a shows a radar antenna emitting a radio frequency (RF) pulse of width τ (typically 0.1 to 10 microseconds) that is backscattered from two reflectors separated by a distance ΔR. If ΔR is greater than $\tau c/2$, two reflected signals will be detected by the radar's receiver system as shown in Figure 3.13.b. In this case the point reflectors are said to be resolved in range. If ΔR is less than $\tau c/2$, the two reflected signals overlap, as shown in Figure 3.13.c. In this case, the two reflectors are not resolved in range. Furthermore, depending on the space between the point reflectors, the tw0-backscattered signals can superimpose constructively, destructively, or in some intermediate way. However, for the receiver to resolve in range, the point reflectors ΔR must be at least equal to $\tau c/2$, as shown in Figure 3.13.d. ΔR is known as the range resolution of the radar, and it can be expressed mathematically as

$$\Delta R = \frac{c\tau}{2}. \tag{3.7}$$

Angular resolution is another important concept described by Richards et al. (2010). Angular resolution, both in azimuth and elevation, is determined by the antenna beamwidth in the same plane. Let us consider again two reflectors located at the same range but with different azimuth or elevation as shown in Figure 3.14. In this case the point reflectors will backscatter an electromagnetic wave if they are within the antenna main lobe and are both irradiated at the same time. As explained in Section 3.1.3, the main lobe width is known as θ_3 and is typically taken to be 3-dB the beam width of the antenna. The distance between the point reflectors, which are located at 3-dB edges of the beam, is known as the cross-range resolution (ΔCR) of the radar and can be expressed mathematically as:

$$\Delta CR = 2Rsin\left(\frac{\theta_3}{2}\right) = R\theta_3 \tag{3.8}$$

where R is the distance or radius between the radar and the point reflectors. Typically, for a circular antenna, the main lobe width can be estimated using the following equation:

$$\theta_3 \approx \frac{1.3\lambda}{D} \text{ radians} \tag{3.9}$$

where λ is the wavelength, and D is the diameter of the circular antenna. The equations listed above can be used to determine both the azimuth and elevation resolution. Contrary to range resolution, which is constant with distance, cross range resolution increases linearly with distance.

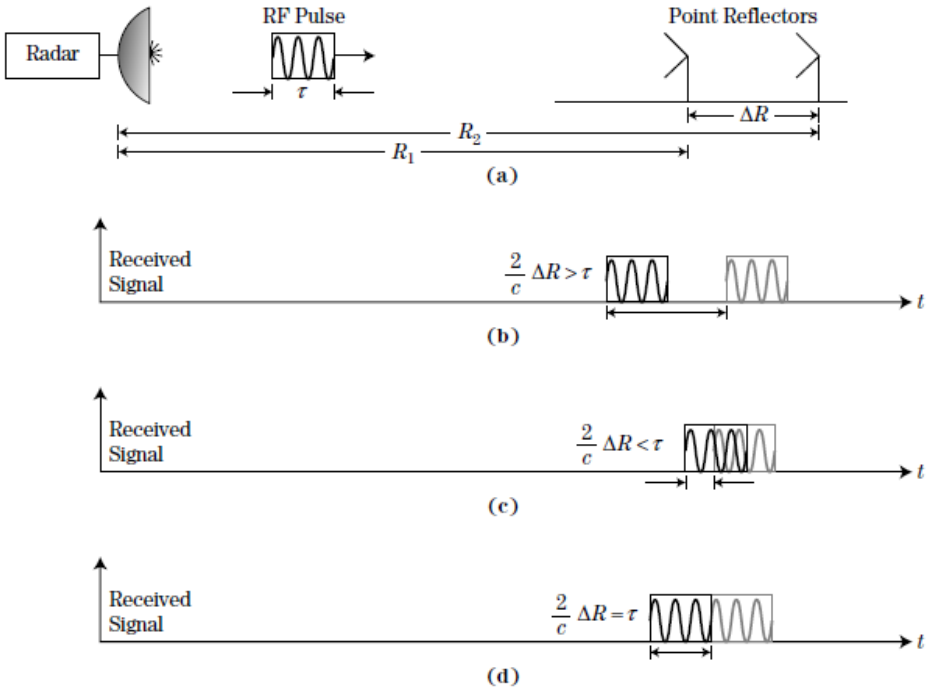

Figure 3.13. Concept of range resolution: (a) RF pulse and point reflectors; (b) Receiver output for point reflectors resolved in range; (c) Receiver output for point reflectors unresolved in range; and (d) Receiver output for defining range resolution (Richards et al., 2010).

3.1.11. Radar Imaging. Richards (2014) states that most radars in use today are used to perform three functions: 1. detection; 2. tracking; and 3. imaging. Only the last function will be presented in more detail in this work.

Imaging is the methodology used to obtain information on one or more targets or to obtain the information of wide areas. The methodology is a two-step process: 1. a high-resolution range profile of the target or area of interest must be developed; and 2. a high-resolution azimuth and elevation profile must be developed.

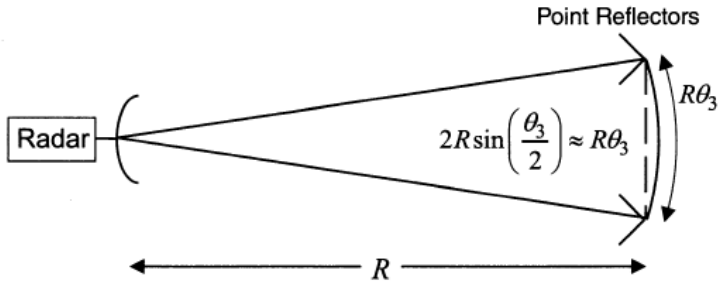

Figure 3.14. Angular resolution concept (Richards, 2014).

In the beginning radar systems were used to create two-dimensional images of an area of interest. Over the last few decades, interferometric radar techniques have been developed for generating three-dimensional images of targets or areas of interest. The next section will present a summary of radar interferometry.

3.1.12. Type of Instruments. According to Caduff et al. (2015), radar used for imaging areas or targets of interests differs by the type of antenna incorporated in its design. Three types of radar systems available today are presented in Figure 3.15. Type I systems

have a dish antenna, which emits a narrow, pencil shaped beam. Type II systems have a long antenna and emit a very narrow, fan-shaped beam in the azimuth direction. Type III systems have a horn antenna, which moves along a rail and produces a wide, cone-shaped beam. Type III systems are known as synthetic-aperture radars (SAR) because they synthetize a longer antenna. Several commercially available radar systems and their specifications are listed in Table 3.2. Note that the Gamma Ground Portable Radar Interferometer (GPRI-II), which will be used in this research, is a Type II TRI.

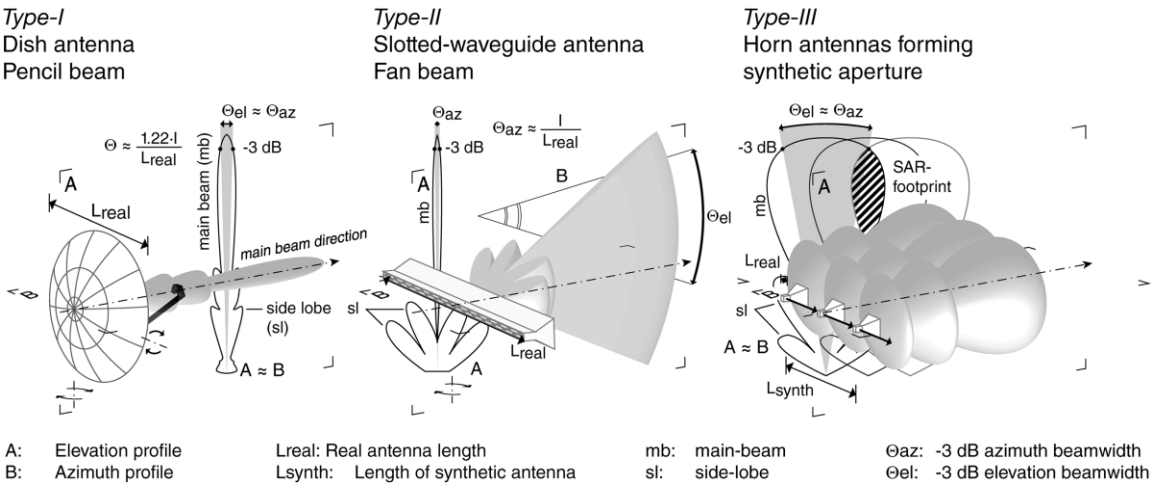

Figure 3.15. Types of antenna used in radar systems and their real aperture radiation pattern (Cadduf et al., 2015).

3.1.13. Interferometry. Caduff et al. (2015) explain that interferometry is the comparison of two radar images where the phase image is subtracted from a phase image taken at an earlier time. In this process, only phase differences can be calculated, because

the total number of phase cycles along the line of sight (LOS) between the radar and the reflector point is unknown due to phase ambiguities.

Table 3.2. List of commercially available radar systems and their specifications (modified from Caduff et al., 2015)

Device	Type	Radar band	Acquisition time	r_{sg_slant}	r_{az} (@1000 m)	Maximum range	Scene coverage
			(min)	(m)	(m)	(m)	(°hz; °vt)
MSR	I	X	N/S	N/S	N/S	2500	N/S
SSR	I	X	25 min per 4000 px	1·5	35	3500	270; 122
GPRI	II	Ku	10°/sec	0·9	8	10000	360; 35
LISA	III	Ku, C	10–60	3-5	N/S	N/S	20; N/S
IBIS-L/M	III	Ku	5–10	0·75	4·4	4000	17; 15
Gb-SAR	III	X	2–3	ns	N/S	N/S	30; N/S
FastGbSAR	III	Ku	<0·2	0·75	4·5	4000	N/S

Figure 3.16 was presented by Caduff et al. (2015) to graphically present the differential interferometry process. As can be seen in this figure, the ambiguous phase differences of two images are the sum of topographic ($\Delta\varphi_{topo}$), atmospheric ($\Delta\varphi_{atmo}$), displacement ($\Delta\varphi_{disp}$), and system noise ($\Delta\varphi_{noise}$) contribution. However, for most displacement detection tasks, only the displacement phase contribution ($\Delta\varphi_{disp}$) is of interest. To isolate the displacement phase contribution, the other terms mentioned before must be determined and subtracted from the total differential interferogram. In the case of continuous monitoring, where the antenna does not change position between image acquisitions, the topographic phase contribution ($\Delta\varphi_{topo}$) is zero. However, for interrupted

monitoring campaigns instrument repositioning errors can occur, which introduce a baseline error. For small repositioning errors, this baseline error can be corrected in the same way as the atmospheric phase ($\Delta\varphi_{atmo}$) component. If the repositioning error is relatively large, greater than one centimeter, then the resulting phase variations can only be corrected with digital elevation models.

Monserrat et al (2014) presented the principles of TRI interferometry for deformation measurements. According to the authors, TRI is a sensor used for imaging. The technique provides a complex number for each pixel in the acquired image. This complex number contains the in-phase (*I*) and quadrature (*Q*) of the received signal. The signal phase (φ) and amplitude (*A*) phase can be obtained from *I* and *Q*.

The signal phase is used for deformation measurements of the area of interest. On the other hand, the amplitude can be used for scene interpretation and for backscattering analysis. Contrary to satellite interferometry, deformation measurements by terrestrial radar interferometry are usually carried out from a zero-base line configuration. As will be presented later in this section, this is only true for continuous measurements campaigns performed from the same point of observation. For example, in a deformation measurement campaign where the area of interest has been scanned twice by a TRI, the phases of two pixels of the same target at different times can be computed as shown in Equations (3.10) and (3.11):

$$\varphi_1 = \varphi_{geom-1} + \varphi_{scatt-1} = \frac{4\cdot\pi\cdot R_1}{\lambda} + \varphi_{scatt-1} \tag{3.10}$$

$$\varphi_2 = \varphi_{geom-2} + \varphi_{scatt-2} = \frac{4\cdot\pi\cdot R_2}{\lambda} + \varphi_{scatt-2} \tag{3.11}$$

where R_1 and R_2 are the instrument-to-target distances at each acquisition, φ_{scatt} is the phase shift generated during the interaction between the microwaves and the target, λ the

wavelength of the instrument, and the factor 4π is related to the two-way path of radar-target-radar. Then, the interferometric phase $\Delta\varphi_{21}$, which is the main TRI observation, can be computed using Equation (3.12):

$$\Delta\varphi_{21} = \varphi_2 - \varphi_1 = \frac{4\cdot\pi\cdot(R_2 - R_1)}{\lambda} + (\varphi_{scatt-2} - \varphi_{scatt-1}) \tag{3.12}$$

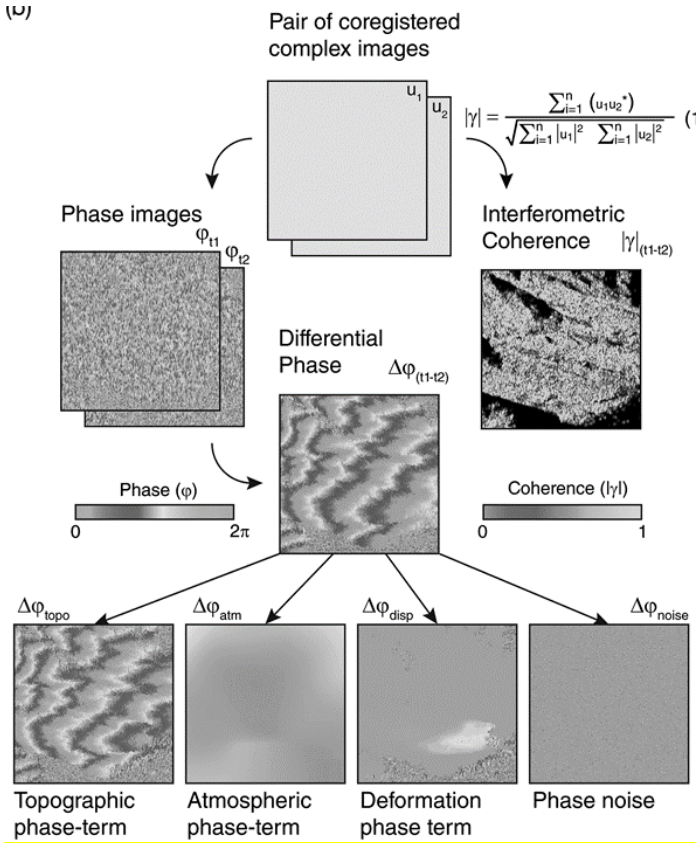

Figure 3.16. Phase components of the differential phase and coherence of the interferogram (modified from Caduff et al., 2015).

If the phase shift components $\varphi_{scatt-2}$ and $\varphi_{scatt-1}$ do not change between two measurements (i.e., insignificant variation over time), $\Delta\varphi_{21}$ is directly related to the

distance difference (R_2-R_1) and hence to the target displacement. However, in real case scenarios, four other terms must be accounted for, as shown in Equation (3.13):

$$\Delta\varphi_{21} = \varphi_2 - \varphi_1 = \varphi_{defo} + (\varphi_{atom2} - \varphi_{atom1}) + \varphi_{geom} + \varphi_{noise} + 2 \cdot k \cdot \pi \quad (3.13)$$

where φ_{defo} is the component related to the displacement; ($\varphi_{atmo2} - \varphi_{atmo1}$) is the phase component effect due to the atmospheric conditions present at the time of data gathering; φ_{geom} is the geometric phase component due to repositioning errors between two acquisitions; φ_{noise} is the phase component related to the term ($\varphi_{scatt-2}$ - $\varphi_{scatt-1}$) and other noise sources (i.e., instrument noise); and $2 \cdot k \cdot \pi$ is used because $\Delta\varphi_{21}$ is wrapped, where k is an integer. Equation 3.13 is the main observation of TRI deformation measurements. In satellite base interferometry, the term φ_{geom} corresponds to the orbital phase component. As mentioned before, Equation 3.13 does not contain the topographic phase component (φ_{topo}). This is only true if the TRI measurements are carried out from the same observation point, which is known as a zero-baseline configuration.

The first objective of this research is to correct repositioning of the instrument during discontinuous campaigns. We propose that a geometric phase component that occurs due to repositioning errors between two image acquisitions (φ_{geom}), as explained by Caduff et al. (2015) and by Monserrat et al (2015), can be determined with a compact laser measurer device. In real-life scenarios, inexpensive targets can be permanently installed to the front or to the rear of the TRI to measure repositioning offsets with a compact TLS unit, and the repositioning offsets measured with the compact TLS unit can be used as a geometric phase component in Equation 3.13.

3.1.14. Phase Unwrapping. According to Monserrat et al. (2014), the term *k* in Equation 3.13 must be correctly estimated for accurate deformation measurements. The term *k* is used to reconstruct the full phase value by adding integer numbers of cycles to the wrapped phase. This is known in radar interferometry as phase unwrapping. This is perhaps the main limitation of TRI for deformation monitoring, as *k* has infinite solutions. The majority of phase unwrapping techniques assume that the full interferometric phases (i.e., the unwrapped phases) vary smoothly over a given interferogram and satisfy this condition as expressed mathematically in Equation (3.14):

$$\left|\Delta\varphi_{12\_unwr}(i,j) - \Delta\varphi_{12\_unwr}(k,l)\right| < \pi \tag{3.14}$$

where (*i*,*j*) and (*k*,*l*) represent two adjacent coherent pixels. If Equation 3.14 is not satisfied, phase unwrapping errors that are multiples of 2π can occur. This introduces severe errors in deformation measurements. Considering that 2π corresponds to a displacement of half the wavelength of the instrument (i.e., $2\pi = \lambda/2$), the above condition in terms of displacements can be expressed using Equation (3.15):

$$|Defo\_\Delta t(i,j) - Defo\_\Delta t(k,l)\,| < \frac{\lambda}{4} \tag{3.15}$$

where λ is the wavelength of the TRI, and *Defo_Δt* is the deformation between two observations. This condition is critical for discontinuous measurement campaigns. It may require adjusting the observation time to meet this condition. However, it is not always possible to adjust the observation time between measurements (i.e., in the case of very fast displacement rates).

According to Cadduf et al. (2015), phase unwrapping is performed to correct errors in the determination of the absolute differential phase when displacements exceed multiple wavelengths or when phase differences per pixel of two adjacent pixels are greater than

one quarter the wavelength ($\lambda/4$) of the radar. To avoid ambiguities, a sampling interval below $\lambda/4$ should be defined. The authors concluded that the confirmation of any ambiguity can be used to constrain the results by using an independent survey method with accuracy below the radar wavelength (λ).

As explained in the last two paragraphs, phase unwrapping is a critical issue in terrestrial radar interferometry. One of the main objectives of this research is to use an independent measurement device, such as a compact lidar, to constrain the results when displacement exceeds one quarter the wavelength ($\lambda/4$) of the instrument or when displacement exceeds multiple wavelengths.

3.1.15. Coherence. Coherence means that two electromagnetic waves recorded at different times have the same frequency, same waveform, and a constant phase difference. Interferograms require interferometric coherence as a fundamental prerequisite (Caduff et al., 2015). Temporal decorrelation may be significant during TRI campaigns and may be caused by random movements of a single scatter in the imaging area. Vegetation and wind high displacement gradient may cause decorrelation.

3.2. TERRESTRIAL RADAR INTERFEROMETER

The University of Missouri at Columbia (MU) possesses a TRI known as the Ground Portable Radar Interferometer (GPRI), which is a Ku-band real-aperture radar system manufactured by Gamma Remote Sensing in Switzerland. A photograph showing the GPRI system is shown in Figure 3.17. Table 3.3 presents operational and performance specifications for the GPRI system. Werner et al. (2012) indicated that the sensitivity of the GPIR, with a signal-to-noise ratio of 30 dB, is equivalent to 0.04 mm of deformation.

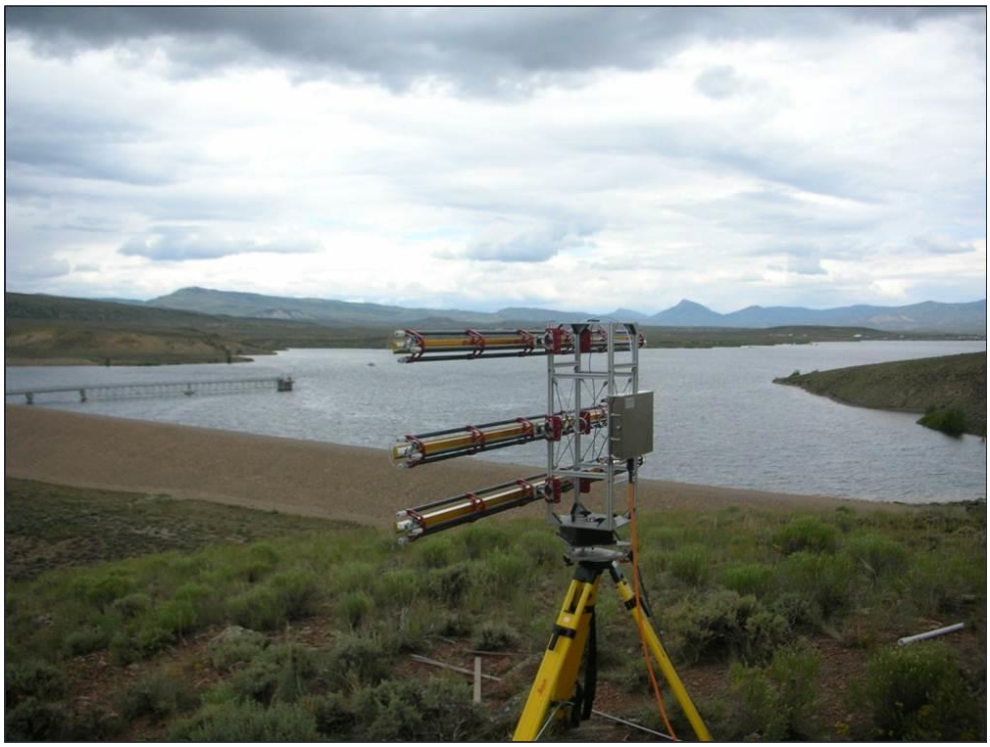

Figure 3.17. Photograph of the Ku-band system at MU (Gillian, 2015).

Table 3.3. Specifications for the Ku-Band GBIR System (modified from Gillian, 2015)

Type	Ku-Band
Radar Type	FM-CW
Frequency	17.1-17.3 GHz
Chirp Duration	0.25 - 8 ms
Acquisition Mode	Single Polarization 2m Antennae (VV)
	Single Polarization Horn Antennae (HH, HV, VH, VV)
Transmit Power	100 mW (+20dBm)
Power Consumption	65 W, 110-220 V(AC) or 24 V(DC)
Chirp Bandwidth	200 MHz
Azimuth Scan Time	20 sec. for 180° sweep
2m Antennae Pattern	38°, 3dB Elevation Beamwidth
	0.5°, 3dB Azimuth Beamwidth
Antennae Polarization	Single Polarization (V)
Radar Operation Range	50m - 10km
Azimuth Resolution	~0.70 at 100m Range Distance
Range Resolution	1 m with Kaiser Weighting
	0.75 m without Kaiser Weighting

3.3. ADVANTAGES AND LIMITATIONS OF TRI

The following sections will present a summary of the advantages and the limitations of TRI systems.

3.3.1. Advantages of TRI Systems. Lingua et al. (2008) reported the following advantages of TRI systems:

1. Sub-millimetric displacements can be measured during continuous measurement campaigns;
2. Long-range monitoring can be achieved reducing risks to technicians in the case of ground instabilities;
3. Near real-time monitoring can be carried out;
4. Measurement campaigns can be conducted independently of weather conditions;
5. Displacement maps generated through the interferometric process are easily and immediately interpretable; allowing a macro evaluation of the area of interest;
6. Digital elevation models (DEM) of the monitored area can be generated within an accuracy of a few meters.

According to Monserrat et al. (2014), TRI systems have the following advantages:

1. This technique can be used to monitor a wide range of deformation rates, from millimeters per year to meters per hour;
2. They can be used to measure millimetric and sub-millimetric displacements;
3. Long-range measurements, in the order of kilometers, can be taken independently of the atmospheric conditions;

4. Images can cover an area of 1 to 2 km^2, which provides a dense measurement coverage of the area of interest;
5. Monitoring can be automated and used for an early warning system.

3.3.2. Limitations of TRI. TRI systems' negative aspects have been reported by Lingua et al. (2008). Some of the limitations are the following:

1. Only displacements parallel to line of sight between the TRI and the area of interest can be detected;
2. The azimuthal resolution of TRI images decreases with range distance, resulting in pixels of some square meters at a range of 200 meters. This limits the application of the TRI systems for rock slope movements;
3. High coherence of the area of interest is necessary to obtain good results;
4. TRI systems are relatively heavy and cumbersome, which requires all terrain vehicles or helicopters to transport them to the observation point;
5. The systems must be installed in such way that no metal objects are in a range of 10 to 20 meters between the TRI and the area of interest. Otherwise, the high reflectivity of metal objects may saturate the radar images, and therefore they cannot be used for deformation monitoring. Furthermore, passing vehicles, thick vegetation, and water bodies can create similar problems.
6. Millimetric changes in the position of the instrument during discontinuous measurement campaigns can dramatically reduce the accuracy of the measurements.

Alba et al. (2008) found that TRI is only capable of monitoring higher frequency deformations at a lower spatial resolution, while TLS can detect lower frequency deformations with a higher point density.

Wujanz et al. (2013) presented the following TRI limitations:

1. The interferometric technique is ambiguous for displacements larger than $\lambda/4$;
2. Data post-processing is complex;
3. The instrument is linked to one standpoint, which limits its application for continuous measurement campaigns;
4. The systems suffer from low spatial resolution.

Monserrat et al. (2014) discussed the following limitations of TRI:

1. TRI interferometry requires coherent data, which is a critical issue during discontinuous measurement campaigns.
2. Ambiguities in the interferometric phases, especially in areas with large displacements, can lead to biased deformation estimates. This limitation is very problematic to discontinuous measurement campaigns.
3. The technique is limited to detect only line of sight displacements (1D deformations). Contrary to terrestrial laser scanners, which can be used to measure 3D displacement, TRI systems cannot be used to monitor vertical displacements.
4. Correct estimation of the atmospheric phase component (φ_{atmo}) requires the presence of stable areas adjacent to the area being monitored. This requirement cannot be satisfied in some situations, which limits the measurement capacity of TRI systems.

Intrieri et al. (2016) pointed out that TRI measures along line-of-sight movements and is not able to measure abrupt and remarkable changes because of loss of coherence and phase ambiguity.

3.4. SUMMARY

This section provided a general overview of radar and the fundamentals of differential interferometry for deformation measurements, subjects that are not generally familiar to a civil/geotechnical/geological engineering audience. This was followed by a presentation of the interferometric technique that will be used in this research, and finally some advantages and limitations of TRI, as discussed by others, were presented.

4. LIDAR BACKGROUND

A laser as a device which emits light through a process of optical amplification. It was first built in 1960 by Theodore H. Maiman based on the theoretical work of Charles H. Townes and Arthur L. Schawlow (Hecht, 2008). The word *laser* is an acronym for "light amplification by the stimulated emission of radiation." Laser devices are so common today that the acronym lost its capitalization and became an English noun.

According to Heritage and Large (2009), lidar was developed shortly after the invention of the laser as a surveying tool. Lidar (also stylized LIDAR and LiDAR) is an acronym for "laser induced detection and ranging," or more commonly, "light detection and ranging." According to Ring (1963), lidar was originally a combination of the words *light* and *radar*. As a matter of fact, the Oxford English Dictionary defines lidar as a "detection system which works on the principle of radar, but uses light from a laser." The term lidar is referred to in some other references as a terrestrial laser scanner (TLS), the in-situ 3D-laser scanner (3D TLS), terrestrial lidar, ground-based laser scanner, or ground-based lidar. The generic term TLS will be adopted in this research.

This section provides a summary of the basic concepts of TLS systems. The intent is to give geological engineers and geotechnical engineers a fundamental understanding of TLS concepts utilized in this study.

4.1. TERRESTRIAL LASER SCANNER COMPONENTS

Heritage and Large (2009) explain that TLS systems have the following three main components: 1. a transmitter; 2. an opto-mechanical device; and 3. a receiver/recorder unit. All three main components are incorporated in the TLS unit as shown in Figure 4.1. The

transmitted laser pulse travels from the TLS unit to the target of interest, where some of the energy is reflected to the TLS unit and recorded by the receiver/recorded unit. Then, the recorded data is analyzed to determine the position of the target of interest in space.

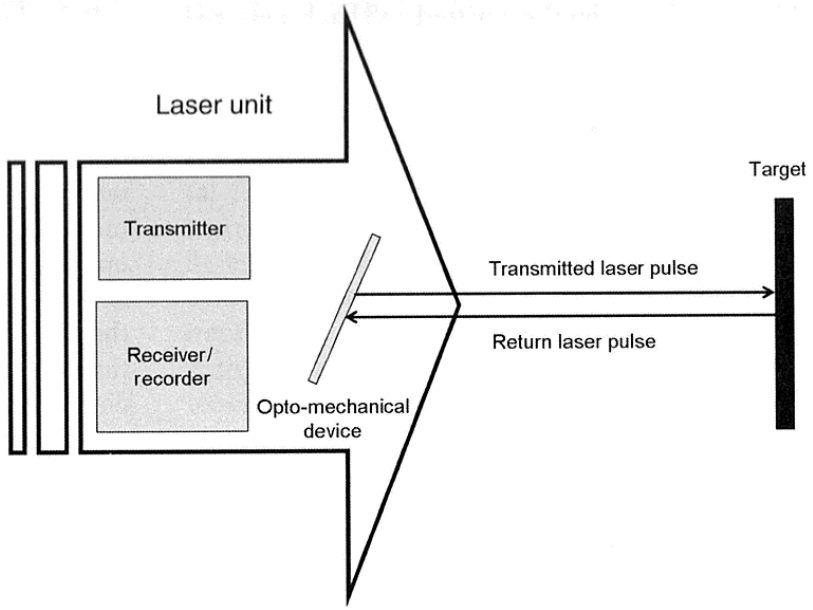

Figure 4.1. Basic components of a TLS instrument (Heritage and Large, 2009).

4.2. POINT CLOUD PRODUCED BY TLS

As mentioned previously, TLS transmits a laser pulse to a target of interest, where some of the energy is reflected to the recorder unit. In the same way, this process is continuous until TLS finishes scanning the whole surface of the target of interest. Aqeel (2012) pointed out that this process can acquire millions of points in a short time with an accuracy rate in the range of 3-5 mm. The closer the points are together, the higher the

resolution of the image, and thus the more the image resembles a photograph, as shown in Figure 4.2.

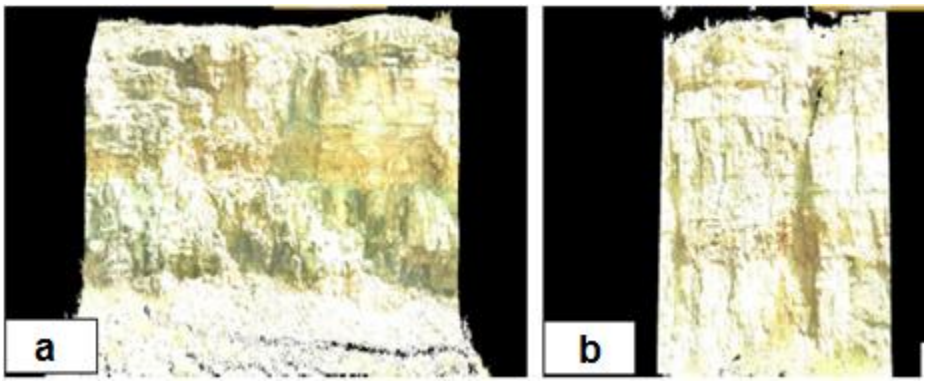

Figure 4.2. The closer the points are together, the higher the resolution of the image and thus the more the image resembles a photograph. (a) A scanned rock cut that has 9.5 million points, while (b) is the same rock cut but with less detail and only 8.2 million points (Otoo, 2012).

According to Otoo et al. (2012), the resultant points are identified by local *xyz* coordinates related to the scanner position. This is performed by measuring the horizontal and vertical angles and the distance between the center of the scanner and the surface of interest. These *xyz* coordinates and their associated intensity of reflectivity from the surface are known as a "point cloud." By measuring the geographical coordinates in the field for at least one point for each scan, the local coordinates of the TLS data set "point cloud" can be transformed into a geographical coordinate system that is able to locate any point in real 3D space. As shown in Figure 4.3, the *xyz* coordinates of the object of interest can be computed as shown in Equations (4.1), (4.2), and (4.3), respectively:

$$x = \sin \alpha_h d \tag{4.1}$$

$$y = \cos \alpha_h d \tag{4.2}$$

$$z = \sin \alpha_v d \tag{4.3}$$

where α_h is the horizontal angle of the laser pulse, α_v, is the vertical angle of the laser pulse, and *d* is the distance from the TLS to the object.

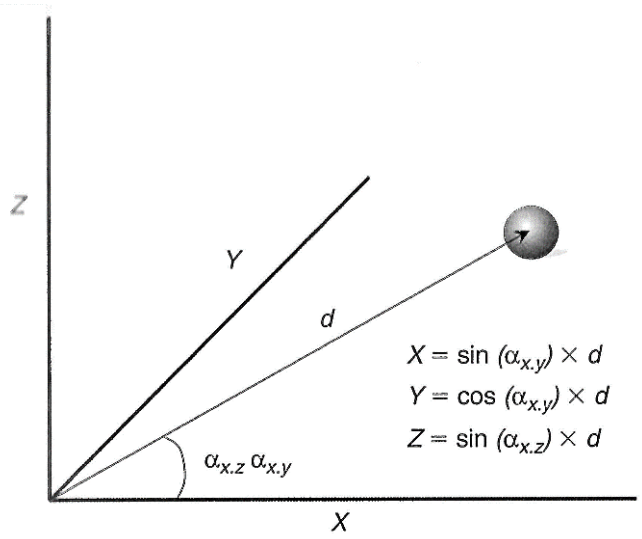

Figure 4.3. Illustration of the ability of TLS systems to position remote objects in 3D space (Heritage and Large, 2009).

Otoo (2012) explains that TLS data collection depends on the system's design and its components. Three basic TLS data collection methodologies are point data (*XYZ*); point and intensity (*XYZI*); and point, intensity, and mapped color (*XYZRGB*). Point data (*XYZ*) generates relatively small files that are easier to store and process by digital computers than the other two methodologies. However, point data (XYZ) is the harder of the three methodologies for human visualization. The *XYZ* values are the coordinates of the point.

The point and intensity data (*XYZI*) include the coordinates of the point, plus an intensity value that is directly related to the reflectivity of the scanned object. Intensity is the percentage of the light returned in terms of light emitted. Intensity introduces a photographic quality into the point cloud, making the data relatively easier to visualize. The point, intensity, and mapped color data (*XYZRGB*) consist of points and colors matching the red, green, and blue properties of a colored digital image. These data are the easiest to visualize for humans. TLS systems with internal digital cameras allow automatic association of the point data with colors from a corresponding optical image. The three basic point cloud data are shown in Figure 4.4.

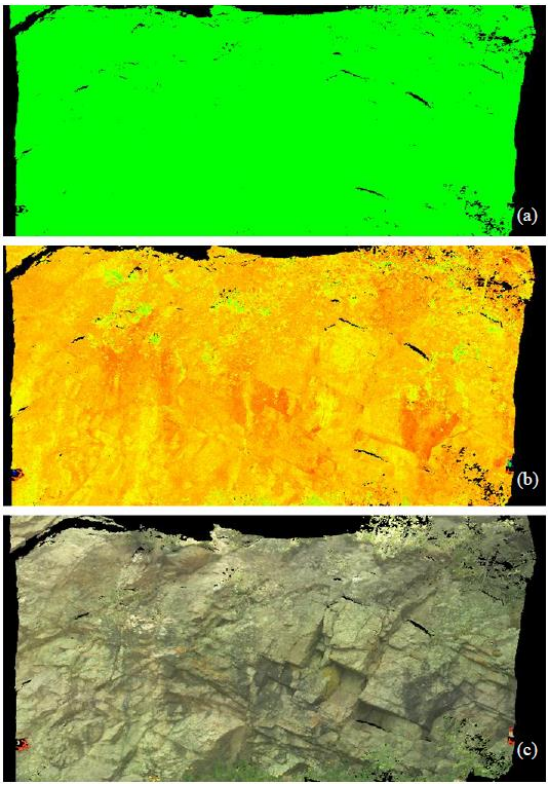

Figure 4.4. Three basic point cloud data of a rock cut: a. point data, b. point and intensity, c. point, intensity, and mapped color (Otoo, 2012).

4.3. CLASSIFICATION OF TLS SYSTEMS

Fröhlich and Mettenleiter (2004) mentioned that it is very difficult to classify TLS systems due to the wide variety of systems available in the market. According to the authors, TLS systems can be classified based on either the distance measurement principle employed by the systems or based on the technical specification of the systems. The authors pointed out that there is no one universal laser scanner that can be used for all imaginable applications. Laser scanners can be designed for short-range applications (up to a few meters), for medium-range applications (up to 100 m), and for long-range applications (up to 1000 m). The most common classification of TLS systems is based on the principle of the distance measurement system, because it takes into consideration both the range and accuracy of the TLS system. Accordingly, TLS systems can be classified into time-of-flight or "pulsed" scanners, phase-based scanners, and triangulation-based scanners.

4.3.1. Time of Flight. According to Fröhlich and Mettenleiter (2004), the most commonly used measurement system for laser scanners is the-time-of flight principle. This scanner can be used to take long-range measurements with reasonably accuracy. This type of scanner was used in this research.

Otoo (2012) explains that time-of-flight laser scanners operate under the principle that light travels at a constant speed in space, and that based on the travel time the distance to the target of interest can be computed using Equation (4.4):

$$Distance = \frac{Speed\ of\ Light\ x\ Time\ of\ Flight}{2} \tag{4.4}$$

Figure 4.5 is an illustration of the distance measurement from a time-of-flight sensor.

4.3.2. Phase Shift. Fröhlich and Mettenleiter (2004) explain that phase shift is another technique that can be used for medium-range distances. The typical range for phase

shift systems is less than 100 meters. These systems can achieve accuracies in the order of millimeters.

According to Otoo (2012), phase-shift scanners have a sensor that compares the phase of the emitted light to the phase of the received reflected light. Then, the time-of-flight can be calculated using Equation 4.5:

$$Time\ of\ Flight = \frac{Phase\ Shift}{2\pi\ x\ Modulation\ Frequency} \quad (4.5)$$

Figure 4.6 is an illustration of a phase shift sensor and a target.

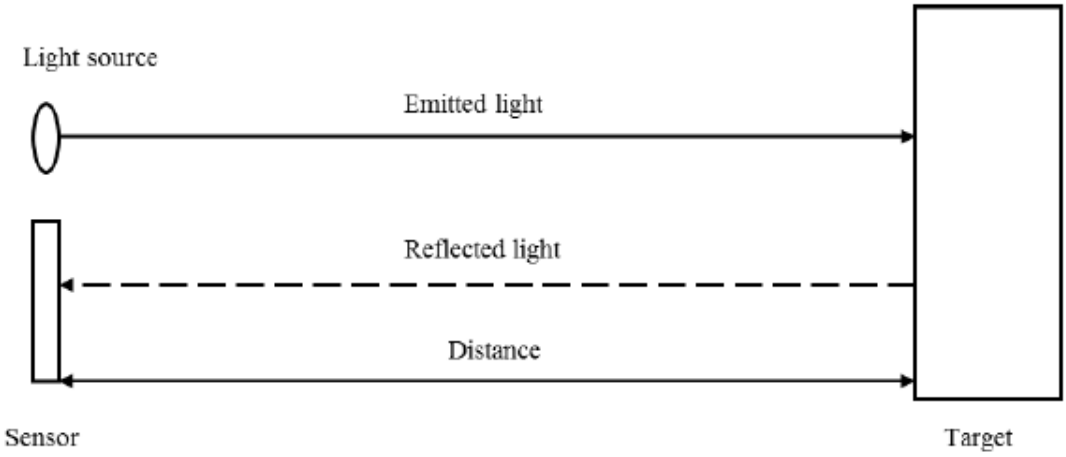

Figure 4.5. Schematic of a time-of-flight sensor and a target (Otoo, 2012).

4.3.3. Optical Triangulation. Fröhlich and Mettenleiter (2004) mention that a triangulation-based laser scanner is a scanner that can be used for distance ranges up to few meters (typically less than 5 m) with high accuracy down to some microns of a meter. However, this type has limited applications and is more commonly used in industrial applications.

4.4. TLS DATA PROCESSING

Point cloud data collected from the field must be processed to extract the needed measurements or information. Many commercially available software packages for point cloud processing exist today. Most of these software tools, however, were developed by scanner manufacturers for general projects. According to Fröhlich and Mettenleiter (2004), the most advanced software packages are: Cyclone from Leica, 3D IPSOS from Mensi, and Light Form Modeller (LFM) from Zoller and Fröhlich.

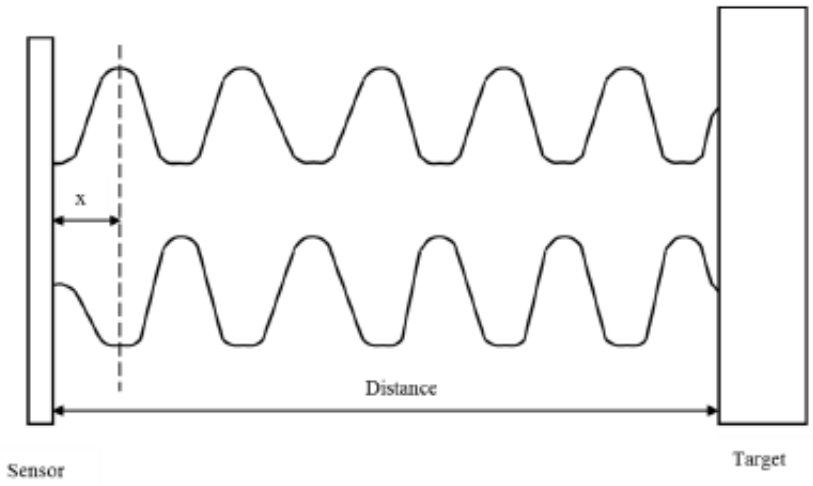

Figure 4.6. Schematic of a phase shift sensor and a target; *x* is the distance corresponding to the differential phase (Otoo, 2012).

The TLS post processing software that will be used in this research was developed at Missouri S&T by Boyko (2014). The software is composed of a series of seven C++ programs that execute recursive algorithms. Each of these programs is executed through the command prompt line. These programs have the ability to mesh, bin, sort, clip, and

finally output the results for interpretation. The following programs were used in this research: findminmax, load, and view2surf. Findminmax is used to find the minimum and maximum *xyz* coordinates of the point cloud, and it creates a file that is used by the next program. Load reads the file created by findminmax and bins all the acquired points into a predefined mesh resolution. View2surf displays duplicates images of the scanned area and allows the user to label objects with a number and with a specific role. View2surf is also used to estimate the distance from the TLS to the target of interest.

4.5. ADVANTAGES AND LIMITATIONS OF TLS

The following sections will present a summary of the advantages and the limitations of TRI systems.

4.5.1. Advantages of TLS. Aqeel (2012) presented the following advantages of using TLS systems:

1. The technique allows the acquisition of data both at the base and top of the rock outcrop, providing a more statistically representative sample;
2. Steep and high rock slopes can be surveyed;
3. The survey can be undertaken remotely, which reduces risks and hazards for workers in terms of traffic accidents and or rock falls;
4. The ability to build databases for surveyed rock slope face that can be used and updated anytime.

Positive aspects of using TLS to detect slope movements were presented by Lingua et al. (2008). They are as follows:

1. TLS systems can quickly acquire millions of points of the monitored area and provide a 3D model of the area of interest;

2. Displacements and volume changes computations of the area of interest can be determined;
3. TLS are typically lighter and less cumbersome than TRI systems, making it possible to transport them without all-terrain vehicles or helicopters;
4. TLS techniques can be used to generate dense digital elevation models of the monitored area. This allows detection of displacement of small areas or objects within the monitored area and not in pixels of several square meters of dimensions as in the TRI system;
5. Repeated or discontinuous measurement campaigns can be carried out without concerns for changes in the position of the instrument, because the reference system of the models is "fixed" on the markers.
6. The measurement range varies for different instruments; typically, it can vary from a few meters for short-range systems to kilometers for long-range systems.
7. Comparison between multitemporal scans allows detection of 3 D displacements.

4.5.2. Limitations of TLS. Lingua et al. (2008) reported that TLS campaigns must be performed during good weather conditions (i.e., no rain), and that good illumination of the area of interest is necessary when digital images (photographs) are needed.

4.6. ADVANTAGES AND LIMITATIONS OF TLS AND TRI SYSTEMS

Table 4.1 presents a summary of the advantages and limitations of TLS and TRI systems as presented in Section 3.3 and Section 4.5.

Table 4.1. Advantages and Limitations of TLS and TRI.

System	Advantages	Disadvantages
TLS	Systems can quickly acquire millions of points of the area and provide a 3D model of the area.	Campaigns must be performed during good weather conditions (i.e., no rain), and good illumination of the area of interest is necessary when digital images (photographs) are needed.
	Displacements and volume changes computations of the area of interest can be determined.	
	Lighter and less cumbersome than TRI systems, making it possible to transport them without all-terrain vehicles or helicopters.	
	Can be used to generate dense digital elevation models of the monitored area. This allows detection of the displacement of small areas or objects within the monitored area.	
	Repeated or discontinuous measurement campaigns can be carried out without concerns for changes in the position of the instrument.	
	The measurement range varies for different instruments; typically, it can vary from a few meters for short-range systems to kilometers for long-range systems	
	Comparison between multitemporal scans allows detection of 3 D displacements.	
TRS	Sub-millimetric displacements can be measured during continuous measurement campaigns.	Only displacements parallel to line of sight between the TRI and the area of interest can be detected
	Long-range monitoring can be achieved reducing risks to technicians in the case of ground instabilities	The azimuthal resolution of TRI images decreases with range distance, resulting in pixels of some square meters at a range of 200 meters.
	Near real-time monitoring can be carried out.	High coherence of the area of interest is necessary to obtain good results
	Measurement campaigns can be conducted independently of weather conditions.	Relatively heavy and cumbersome, which requires all terrain vehicles or helicopters to transport them to the observation point.
	Displacement maps generated through the interferometric process are easily and immediately interpretable, allowing a macro evaluation of the area of interest.	The systems must be installed in such a way that no metal objects are in a range of 10 to 20 meters between the TRI and the area of interest.
	Digital elevation models of the monitored area can be generated within an accuracy of a few meters.	Millimetric changes in the position of the instrument during discontinuous measurement campaigns can dramatically reduce the accuracy of the measurements
		The interferometric technique is ambiguous for displacements larger than $\lambda/4$.
		Data post-processing is complex
		Low spatial resolution.
		Linked to one stand-point, which limits its application for continuous measurement campaigns.

4.7. TLS SPECIFICATIONS

The Leica Scan Station II, property of Missouri University of Science and Technology, which will be used in this research, is shown in Figure 4.7, and its specifications are listed in Table 4.2. It consists of hardware and an accompanying software program (Cyclone). The hardware components include the scanner unit and a connected laptop to run, operate, and drive the scanner unit to scan the target of interest and to record and store the range, angle, and intensity of reflection data for each reflected and detected laser pulse via a network connection. The installed Cyclone program is used for data set processing either in the field or in an office.

Figure 4.7. A back view for the Leica-ScanStation2 which was used in this research (Aqueel, 2012).

Table 4.2. Specification of the Leica Scan Station 2 (Aqeel, 2012).

Laser scanning type		Pulsed
Color		Green
Range		300 m at 90%; 134 at 18% albedo
Scan Rate		Up to 50,000 points/seconds maximum instantaneous rate
Scan Resolution	Spot size	From 0 – 50 m: 4 mm (FWHH-based); 6 mm (Gaussian-based)
	Selectability	Independently, fully selectable vertical and horizontal point-to-point measurement spacing
	Point spacing	Fully selectable horizontal and vertical < 1 mm minimum spacing, through full range; single point dwell capacity
	Maximum sample distance	< 1 mm
Field of view (FOV)	Horizontal (deg.)	Up to 360
	Vertical (deg.)	Up to 270
	Aim/Sighting	Optical sighting using Quick-Scan bottom
	Scanning optics	Single mirror, panoramic, front and upper window design
	Digital imaging	Low, medium, high automatically spatially rectified
Camera		Integrated high-resolution digital camera
Scanner dimensions (mm)		265 x 370 x 510 without handle and table stand
Weight		18.5 kg
Power supply		36 V, AC or DC

The Faro Laser Scanner Focus 3D X 130, property of Missouri University of Science and Technology, will be used in the first experiment of this research. The instrument is presented in Figure 4.8 and its specifications are presented in Table 4.3. The Focus 3D X 130 uses the phase shift method to measure the distance. The scanner emits constant waves of infrared light of varying length. These waves are reflected from the object back to the scanner. The distance from the scanner to the object is determined as explained in Section 4.3.2.

Figure 4.8. Faro Laser Scanner 3D X130 (from Faro, 2015).

Table 4.3. Specification of the Faro Laser Scanner 3D X130 (Faro, 2019).

Laser scanning type		Phase shift
Color		Invisible – infrared (1550 nm)
Range		300 m at 90%; 134 at 18% albedo
Scan Rate		Up to 50,000 points/seconds maximum instantaneous rate
Scan Resolution	Spot size	From 0.6 – 130 m
	Selectability	N/A
	Point spacing	N/A
	Maximum sample distance	N/A
Field of view (FOV)	Horizontal (deg.)	Up to 360
	Vertical (deg.)	Up to 300
	Aim/Sighting	N/A
	Scanning optics	N/A
	Digital imaging	N/A
Camera		Up to 70 megapixel color
Scanner dimensions (mm)		240 x 200 x 100
Weight		5.2 kg
Power supply		19 V (power supply), 14.4 V (battery)

The Leica Scan Station P40 (see Figure 4.8), property of Missouri University of Science and Technology, will be used in the last experiment of this research. The specifications of the Leica Scan Station P40 are listed in Table 4.3.

Figure 4.9. Leica Scan Station P40 (from Leica, 2019).

4.8. SUMMARY

This section provided a general overview of TLS fundamentals, concepts that are not generally familiar to a geotechnical/geological engineering audience. Advantages and limitations of TRI and TLS systems were summarized in Table 4.1. The next section will present the proposed methodology for this dissertation.

Table 4.4. Specifications of the Leica Scan Station P40 (Leica, 2019).

Laser scanning type		Time-of-flight
Color		Invisible
Range		Minimum 0.4 m. Max 270 m at 34%reflectivity
Scan Rate		Up to 1,000,000 points/seconds maximum
Scan Resolution	Spot size	Less than 3.5 mm (FWHH-based)
	Selectability	N/A
	Point spacing	N/A
	Maximum sample distance	N/A
Field of view (FOV)	Horizontal (deg.)	Up to 360
	Vertical (deg.)	Up to 290
	Aim/Sighting	N/A
	Scanning optics	N/A
	Digital imaging	Low, medium, high automatically spatially rectified
Camera		4 megapixels per each 17° × 17° colour image
Scanner dimensions (mm)		238 × 358 × 395
Weight		12.25 kg
Power supply		24 V DC

5. METHODOLOGY

The experimental part of this research was performed at three different sites. Controlled movements of targets were carried out to document and evaluate the capabilities of both TLS and TRI systems for detecting and monitoring precursory rock movements on the sub-millimetric scale for various sizes and offset distances from the instruments. This section presents descriptions of the field site, the equipment, the experimental setup, and the data collection procedures, the data processing methods, and the proposed methodology to overcome both the single standpoint problem of TRI during campaign-wise deformation monitoring and the ambiguity of the interferometric phase when a target suffers displacement greater than one quarter of its wavelength ($\lambda/4$).

5.1. SITE DESCRIPTION

The first measurement campaign was carried out at Springfield Underground, located at 3510 East Kearney Street, Springfield, Missouri, on November 6, 2017. Figure 5.1 is a Google Earth satellite image showing the location of Springfield Underground. This site was selected due to its constant temperature and because the measurement campaign was not subjected to weather conditions.

The second measurement campaign was carried out at Stephens Lake Park, located at 2001 East Broadway, Columbia, Missouri, on April 5, 2018. Figure 5.2 is a Google satellite image showing the location of Stephens Park. This site was selected due to its wide-open areas and clear field of view of more than 200 m.

The third measurement campaign was carried out at the Missouri S&T Student Recreation Center, located at 705 W. 10th St., Rolla, Missouri, on January 8, 2019. Figure

5.3 is a Google Earth satellite image showing the location of the Student Recreation Center. As in the first measurement campaign, this site was selected due to its constant temperature and because the measurement campaign was not subjected to weather conditions.

Figure 5.1. Google Earth map showing the location of Springfield Underground.

5.2. EQUIPMENT

The main equipment used in this research consisted of a rock displacement simulator, steel targets, compact lidar units, two TLS, and a TRI. These will be described in more detail in the following sections.

5.2.1. Rock Displacement Simulator. The rock displacement simulator (RDS) described by Alzahrani (2017) was employed in this work to simulate precursory rock

movements. The device allows the researcher to estimate the accuracy of both the TRI and the TLS by means of known displacements. The RDS was used in every measurement campaign carried out in this research. This device is composed of the following components: target plate, linear actuator, actuator frame, control circuit, and software control. A brief description of each component will be presented in the following paragraphs.

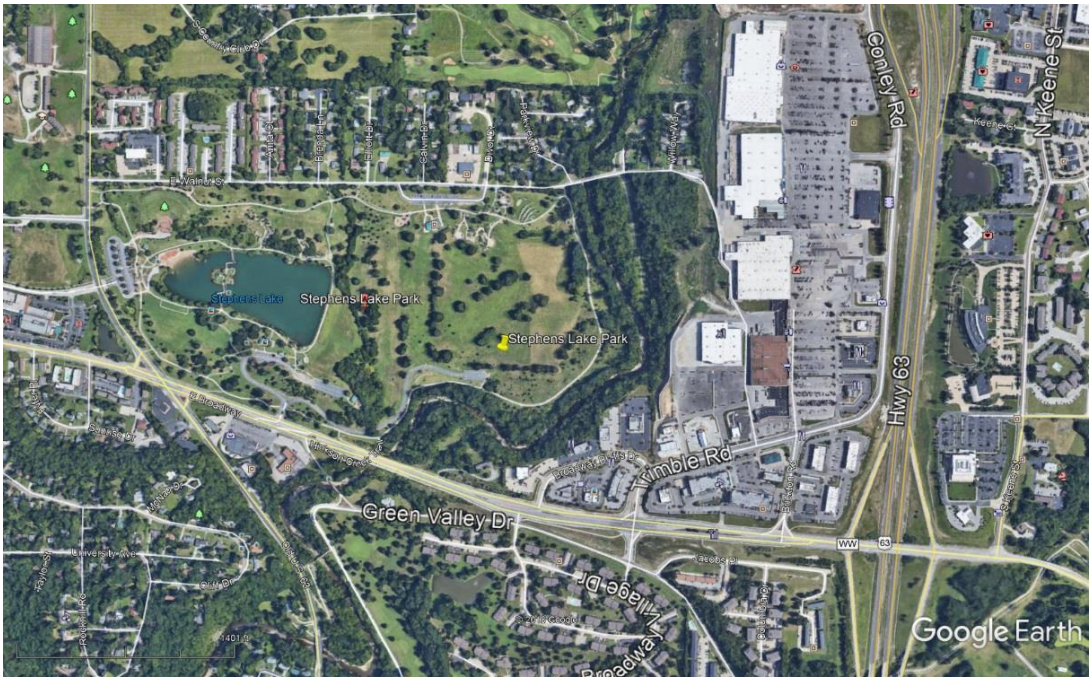

Figure 5.2. Google Earth map showing the location of Stephens Lake Park.

Rectangular aluminum and steel plates were used as targets (i.e., rocks) in the measurement campaigns. The plates were cut to the following dimensions: 20 x 20, 46 x 31, 61 x 61, and 106 x 76 cm. Figure 5.4 shows a 46 by 61 cm target.

Figure 5.3. Google Earth map showing the location of the Missouri S&T Student Recreation Center.

The device used to move the targets was a linear motion actuator. This device works on the principle of the screw mechanism, which generates very precise movements. This type of movement is achieved by a ball screw that is rotated by a motor to a specified position. The linear motion actuator can be used to push or pull the targets. The linear motion actuator is shown in Figure 5.5. It was manufactured by Oriental Motors under model number EZ Limo EZC4-05M.

This EZ Limo was mass produced with a linear movement accuracy up to 0.06 mm and ± 0.02 mm repetitive position accuracy. However, the EZ Limo was driven by a micro-stepping controller to provide a linear movement resolution of 0.00375 mm (Alzahrani, 2017).

Figure 5.4. Rectangular steel plate 61 cm high by 46 cm wide (Alzahrani, 2017).

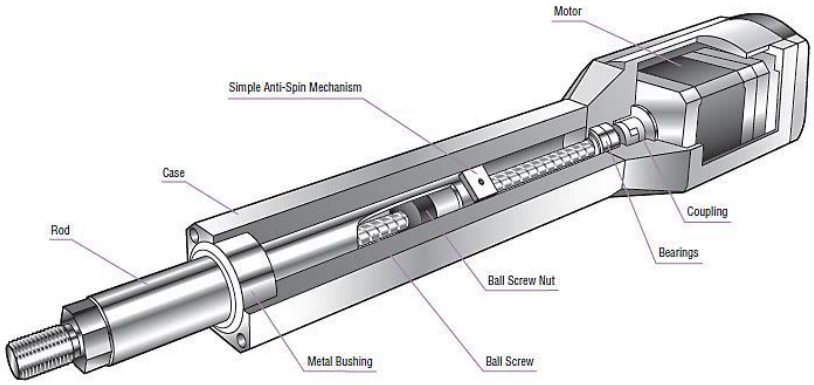

Figure 5.5. EZ Limo EZC4-05M manufactured by Oriental Motors (Alzahrani, 2017).

Two rigid steel frames were designed and constructed (Alzahrani, 2017). These frames provided a very stable platform for the linear motion actuator to which the targets are bolted. The short steel frame and tall steel frame are shown in Figure 5.6 and 5.7, respectively.

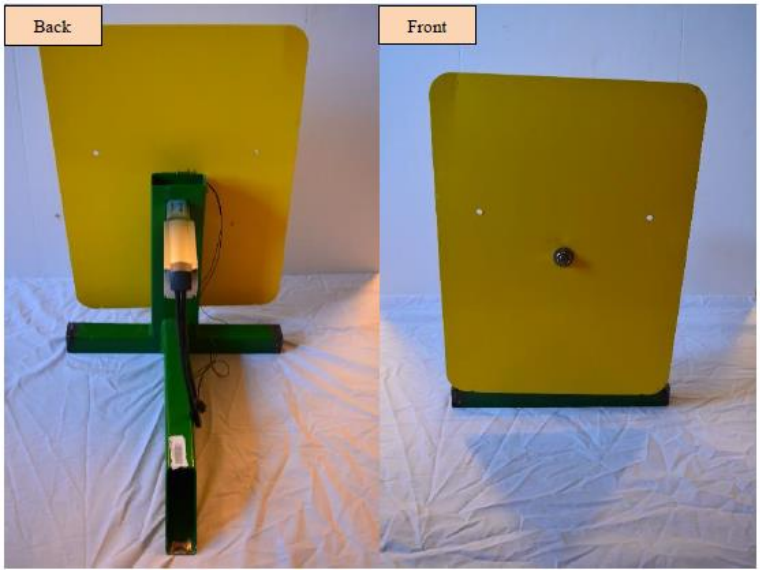

Figure 5.6. Short steel frame with the linear motion actuator and 61 x 46 cm steel target (Alzahrani, 2017).

Figure 5.7. Tall steel frame with the linear motion actuator and 106 x 76 cm target.

The RDS control circuit was based on an Arduino microcontroller and is shown in Figure 5.8 (Alzahrani, 2017). The control circuit allows the linear motion actuator to be operated by remote radio. It can be used to program the linear motion actuator in several different ways for both static and dynamic tests. The control circuit can also be programmed to simulate very slow displacements.

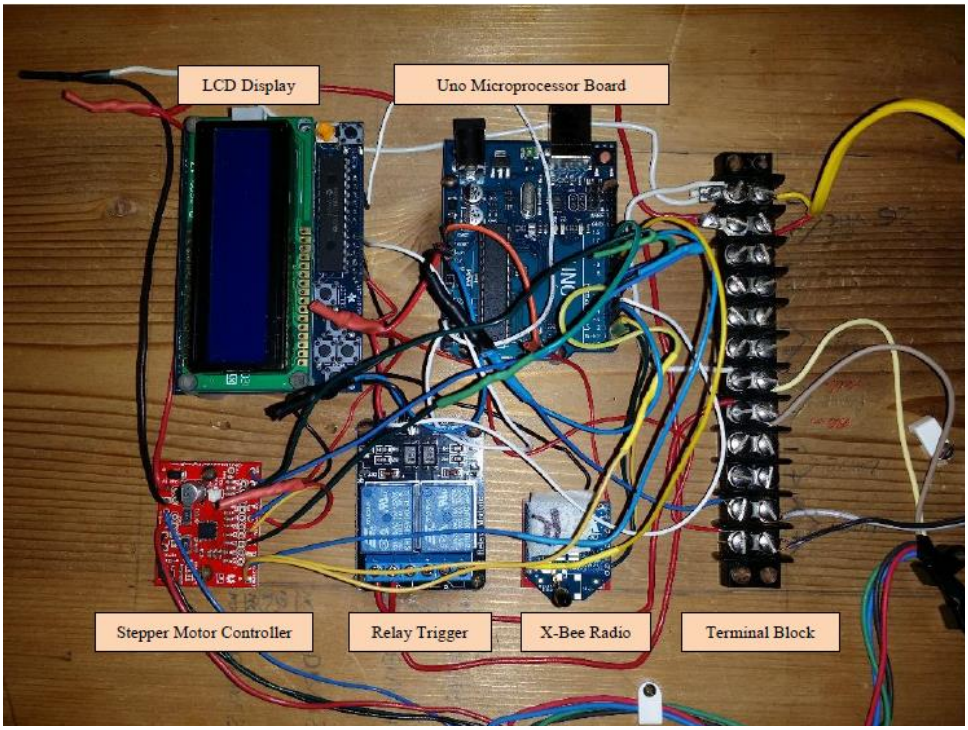

Figure 5.8. Programmable actuator circuit (Alzahrani, 2017).

A graphical user interface (GUI) was developed to operate the RDS (Alzahrani, 2017). Different types of displacements scenarios can be defined using the software controls.

5.2.2. Terrestrial Laser Scanners. The Leica Scan Station II lidar scanner of Missouri University of Science and Technology is shown in Figure 5.9. It consists of the hardware and accompanied software program (Cyclone). The hardware components include the scanner unit as well as a connected laptop to run, operate, and drive the scanner unit in order to scan the target of interest and to record and store the data on range, angles, and intensity of reflection for each reflected and detected laser pulse via a network connection.

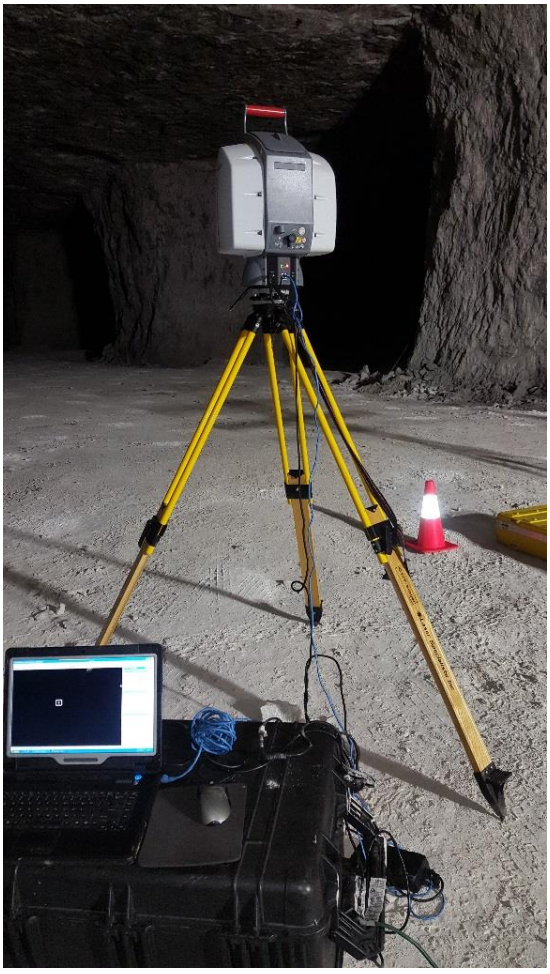

Figure 5.9. A back view of the Leica-ScanStation2 that was used in this research.

The Faro Focus 3D X130 scanner of Missouri University of Science and Technology was used in the first measurement campaign. Figure 5.10 presents the instrument positioned in an adit of Springfield Underground. According to Faro (2019), it has a single point accuracy of ± 2 mm between 10 and 25 m.

Figure 5.10. Back view of the Faro Focus 3D X130 that was used in the first measurement campaign.

The Leica Scan Station P40 lidar scanner of Missouri University of Science and Technology was used in the third measurement campaign, and it is shown in Figure 5.11. According to the manufacturer, the P40 has a range accuracy of 1.2 mm over its full range.

Figure 5.11. From left to right: Leica Scan Station II and Leica Scan Station P40.

5.2.3. Terrestrial Radar Interferometer. The TRI used in this research is owned by the University of Missouri (MU). The instrument is manufactured by Gamma, and it is commercially known as the Ground Portable Interferometric Radar (GPIR). As shown in Figure 5.12, the instrument is composed of: a transmitting antenna, two receiving antennas, a radio frequency controller, a mounting frame, a stepping motor with tribrach, a portable tripod, and a field computer.

5.2.4. Compact Lidar Units. Compact lidar units were used in this research to gather additional data to overcome the two main limitations of the TRI: its single standpoint problem and ambiguities related to large displacements. In the first case, the data collected from the compact lidar units can be used as a geometric phase component (φ_{geom}) to correct errors due to repositioning of the instrument during discontinuous campaigns. In the second case, the data collected from the compact lidar units can be used to identify phase ambiguity

errors when displacement rates exceed one quarter the wavelength ($\lambda/4$) by multiples of the radar wavelength (λ).

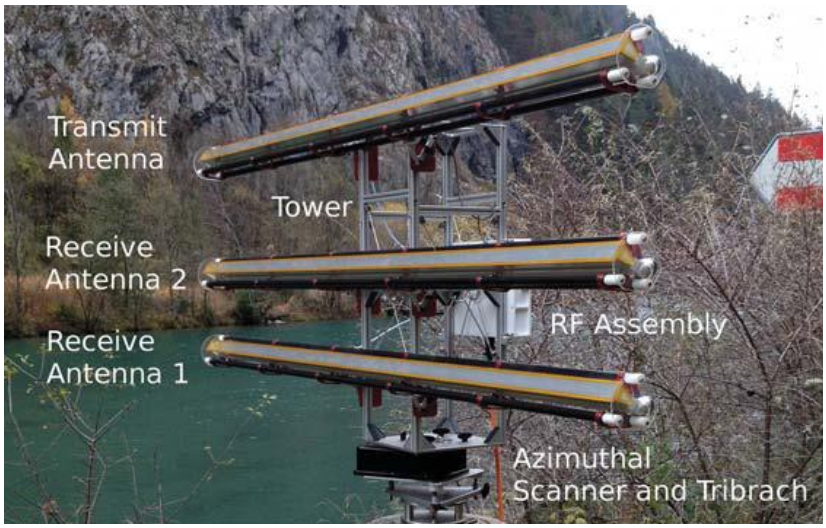

Figure 5.12. Main components of the Gamma GPRI-II (Gamma, 2014).

The end goal was to mount the compact lidar units on one of the T-slotted aluminum bars (Figure 5.13) of the TRI tower using a metal bracket and T-nuts. The following compact lidar units were used in this research: Noyafa NF-2680, and Bosch GLR-825.

The Noyafa NF-2680 is an inexpensive laser distance measurement device manufactured in Shenzhen, China. According to the manufacturer, it can take measurements up to 80 meters away. The device is shown in Figure 5.14, and its specifications are listed in Table 5.1.

Figure 5.13. T-Slotted aluminum framing.

Figure 5.14. Noyafa NF-2680 laser distance measurer (Noyafa, 2018).

Table 5.1. Noyafa NF-2680 specifications (Noyafa, 2018).

Maximum measurement distance	80 meters
Measurement precision	+/- 1 mm
Test time	0.1-3 sec
Laser type	II & 635 nm & < 1 mw
Dimensions	108 x 51x 31 mm
Weight	88 g
Power	2 AAA batteries

The Bosch GLR 825, shown in Figure 5.15, is another laser measurer device. According to the manufacturer, it can be used outdoors to measure distances up to 825 ft (251 m) with an accuracy of 1/25 in. (1 mm). The device specifications are listed in Table 5.2.

Figure 5.15. Bosch GLR 825 laser distance measurer (Bosch, 2018).

Table 5.2. Bosch GLR 825 specification (Bosch, 2018).

Accuracy	0.04 in (1 mm)
Power	4 AAA Batteries
Laser Class	2.0
Laser Diode	630 ~ 670 nm, = 1 mw
Range	2 in (50 mm) to 825 ft (251 m)
Weight	0.5 lb (227 g)

5.2.5. Synthetic Rock. Miles (2018) designed and constructed a synthetic rock (Figure 5.16) to simulate sub-millimeter movements of rocks. The bulk structure of the synthetic rock is composed of Styrofoam and polypropylene. The synthetic rock was covered with a layer of Prolite® tile mortar to simulate a surface roughness and dielectric constant similar to a real rock. The synthetic rock was fixed to the wooden board of a displacement device as shown in Figure 5.17. The displacement device allows the synthetic rock to move in controlled displacement increments. The displacement device was constructed by mounting a wooden frame to a precision drill vice. Displacements of the synthetic rock are achieved by manually rotating a gear at the rear of the vice. The magnitude of displacements was controlled using Starrett ® No. 154A adjustable parallel spacers in the vice, and the vice was closed onto the spacer as shown in Figure 5.18. The spacers were preset to the following lengths: 0.1 mm, 0.25 mm, 0.5 mm, 1 mm, and 2 mm.

5.3. FIRST MEASUREMENT CAMPAIGN

The first measurement campaign was carried out in an adit of Springfield Underground. The TLS and TRI measurement procedures will be presented in the next few sections.

5.3.1. TLS Measurements. TLS measurements were performed during the measurement campaign using both the Missouri S&T Leica Scan Station II (SSII) and the Faro Focus 3D X130. The instruments were installed a few meters to the left and to the right of the TRI as shown in Figure 5.19. The rock displacement simulator was installed at an offset distance of approximately 40 and 90 meters. Figure 5.20 shows the rock displacement simulator with the tall steel frame and the 106 x 76 cm aluminum target. The targets were scanned at a resolution of 1 mm x 1 mm. Three scans of each target movement

were acquired with the SSII with the four targets at an offset distance of 40 m. Also, two scans of each movement of the 106 x 76 cm target installed at an offset distance of approximately 90 m were acquired with the SSII. The displacements used for the rock displacement simulator were the following: 0.05, 0.1, 0.25, 0.5, 1, 2, and 5 mm. Due to difficulties trying to set up the scanning area on the small liquid crystal display of the Faro Focus 3D X130 and due to the time required to scan each target displacement, measurements with the Faro Focus 3D X130 were discontinued after a series of trials. .

Figure 5.16. Picture of the artificial rock mounted on drill vice (Miles, 2018).

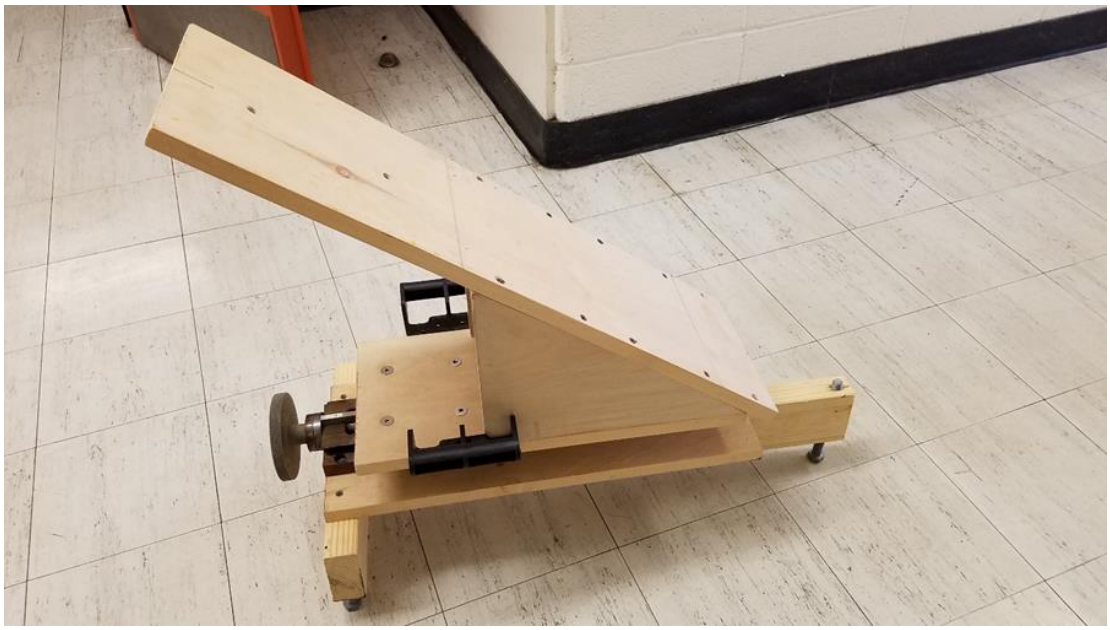

Figure 5.17. Drill vice device with wooden mount attached (Miles, 2018).

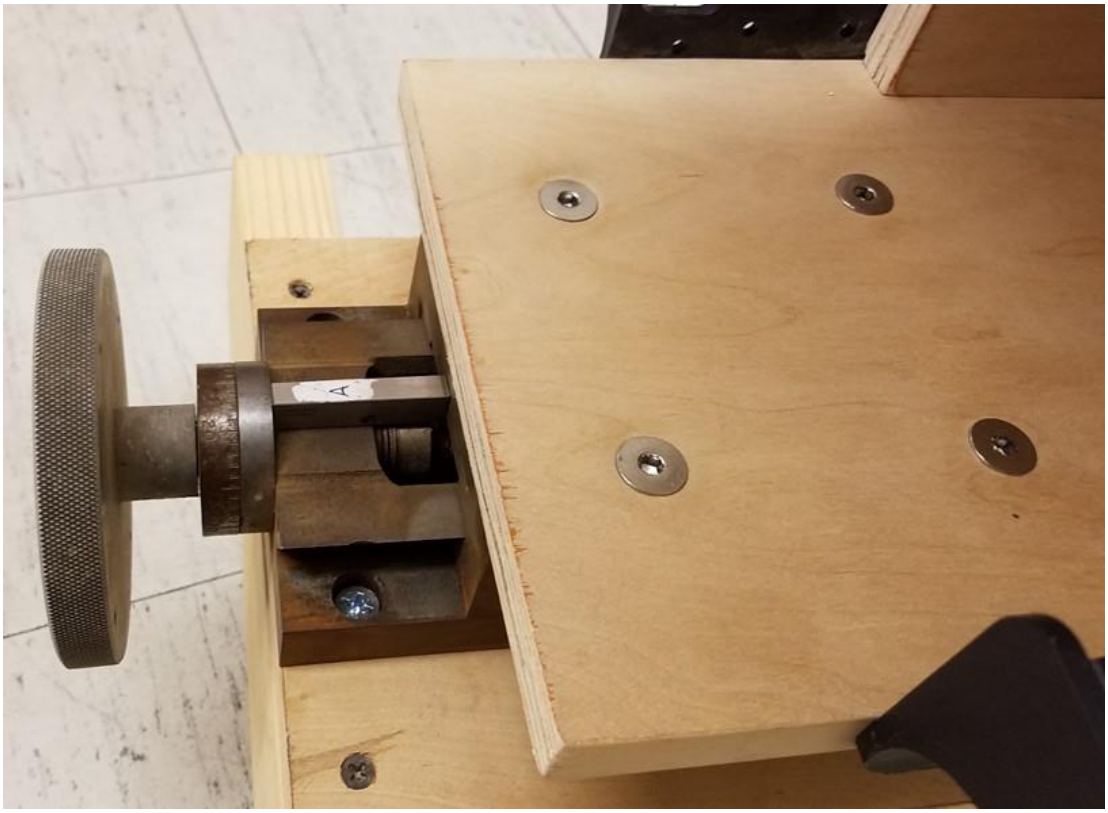

Figure 5.18. Example of a spacer inserted into drill vice (Miles, 2018).

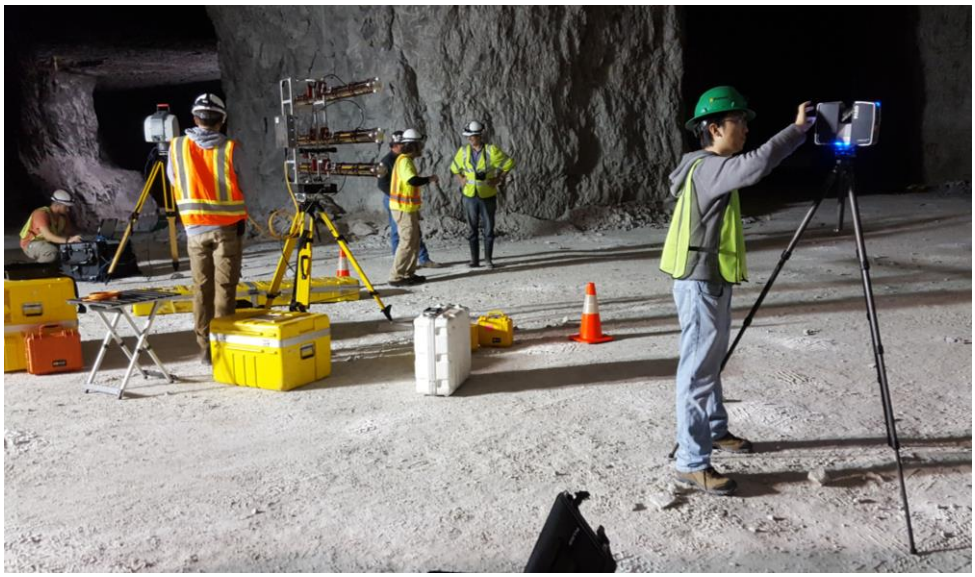

Figure 5.19. Equipment used in Springfield Underground. Missouri S&T Leica Scan Station 2 (to the left), the MU GPIR (center), and the Missouri S&T Faro Focus 3d X130 (to the right).

The TLS data were processed following the same procedure described by Rohrbaugh (2015). First, after every scan of the target was completed, the acquired data were checked on site to confirm that there were no blank spaces in the target. Second, the acquired data were processed at the office using Cyclone (see Section 4.4). In this step, the data is trimmed to include only the area of interest, and then the data is exported to point cloud files in XYZIRGB. Third, the point cloud files are processed using the Missouri S&T lidar software (see Section 4.4). The massive amount of raw data was processed within a week after the measurement campaign.

5.3.2. TRI Measurements. TRI measurements were performed by Dr. Francisco Gómez (Associate Professor and Director of Graduate Studies of the Department of Geological Sciences of the University of Missouri). Dr. Gómez positioned the TRI

perpendicularly to the rock displacement simulator, and he took measurements of the same displacements taken by the TLS.

Figure 5.20. Rock displacement simulator with the 106-cm aluminum target.

5.4. SECOND MEASUREMENT CAMPAIGN

As mentioned in Section 5.1, the second measurement campaign was carried out in Columbia, MO. The TLS and TRI measurement procedures will be presented in the following sections.

5.4.1. TLS Measurements. The TLS scanner was positioned a few meters to the left of the TRI as shown in Figure 5.21. The rock displacement simulator with the short frame was installed at an offset distance of 42 meters. The targets were scanned at a

resolution of 1 mm by 1 mm. One scan of each target movement was performed with the four targets.

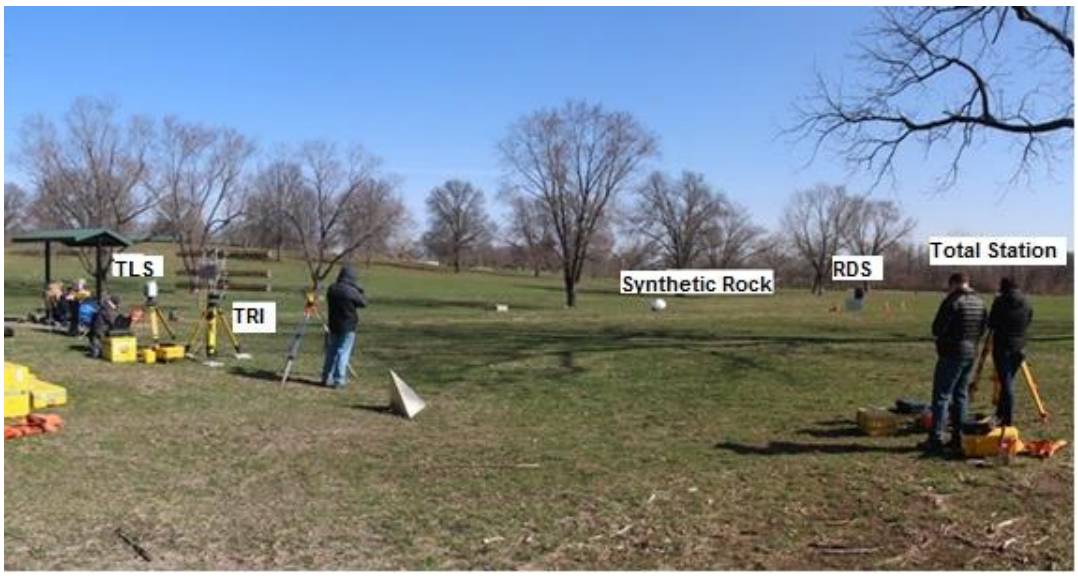

Figure 5.21. Field set-up at Stephen's Lake Park (modified from Miles, 2018).

The displacements used for the RDS were the following: 0.05, 0.1, 0.25, 0.5, 1, 2, and 5 mm. In order to simulate displacements larger than one quarter the wavelength of the TRI, the following displacements were carried out: 7, 9, 18, 26, and 36 mm.

The Noyafa NF-2680 laser distance measurer was positioned on a tripod a few meters to the right of the TLS. At least five readings of every displacement of each target were recorded on a field notebook.

5.4.2. TRI Measurements. The TRI measurements were performed by Dr. Francisco Gómez, as in the first measurement campaign in Springfield, Missouri. The TRI was installed a few meters to the right of the TLS. Dr. Gómez also installed a surveyor total

station to the right of the TRI. Later, Dr. Gómez installed a GPS on the same tripod used for the total station.

5.5. THIRD MEASUREMENT CAMPAIGN

Another controlled experiment was carried out with the Scan Station II, the Scan Station P40, and the TRI. This time, the Bosch laser distance measurement device was used to take readings from the back of the TRI towards a fixed point on a concrete wall and from the front of the TRI towards the RDS. Rock displacements of 0.5, 0.7, 1.0, 2.0, 6.0, 12.0, 15.0, 20.0, and 28.0 mm were simulated using the RDS. The TRI was repositioned after each RDS displacement to simulate a discontinuous measurement campaign. The detailed procedure used for the third measurement campaign was as follows

1. The TLSs and the TRI were installed in the Student Recreational Center of Missouri S&T (please see Figure 5.22). The TRI was placed perpendicular to the targets, and the TLSs were placed to the right of the TRI.
2. A mark was placed on the front (Figure 5.23) and on the back (Figure 5.24) of the TRI to define the placement point of the Bosch GLR-825. Readings were taken from those points towards the RDS and towards a bullseye drawn on the wall just in front of the TRI.
3. All electronic equipment was allowed to warm up for at least 30 min.
4. The RDS was installed at an offset distance of approximately 42 m from the TRI and TLSs (see Figure 5.25 and 5.26).
5. Readings of the 61x61 cm metallic target were taken at the following displacements: 0.5, 0.7, 1.0, 2.0, 6.0, 12.0, 15.0, 20.0, and 28.0 mm. The TRI

was repositioned after every displacement of the RDS, and its position from the wall recorded.

6. Then, the TRI was fixed after taking the 28 mm displacement reading. This time, readings of the 61x61 cm metallic target were taken at the following displacements: 7.0, 9.0, 18.0, 26.0, and 36.0 mm.
7. For every displacement of the RDS, four measurements were taken with the Bosch, three with the Leica Scan Station II and Leica Scan Station P40, and five with the Gama GPIR-II.
8. The TLSs data was post-processed at the office, and the TRI data was processed by Dr. Gómez.

Figure 5.22. Equipment used in the third measurement campaign. From left to right: Leica Scan Station P40, Leica Scan Station II, and Gamma GPIR II.

Figure 5.23. The blue dot on front of the azimuthal scanner of the TRI marks the position from where the RDS displacements were taken.

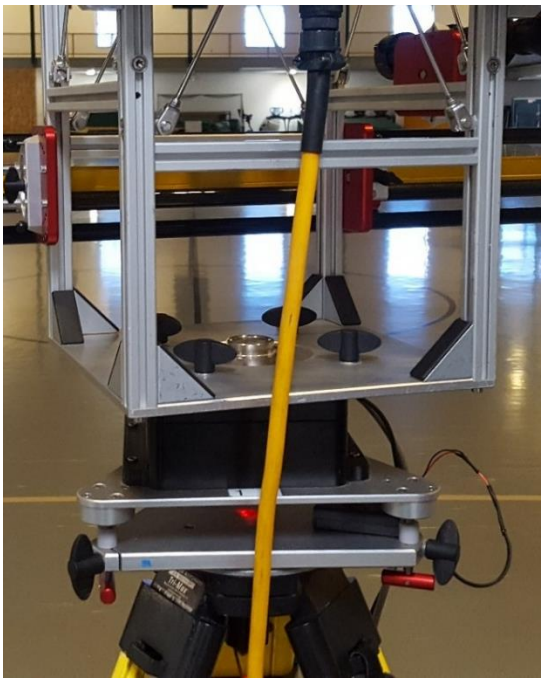

Figure 5.24. The blue dot on rear of the tribrach marks the position from where repositioning displacements were taken.

Figure 5.25. The RDS can be seen at the back and at the center of the picture.

Figure 5.26. Close up of the RDS with the 61 x 61 cm metallic target.

5.6. SUMMARY

This section presented the methodology used in this research to document and evaluate the capabilities of both TLS and TRI systems for detecting and monitoring precursory rock movements of various sizes and at different offset distances from the instruments. The next section will present and discuss the results of the three measurement campaigns. The proposed methodology to overcome both the single standpoint problem of TRI during campaign-wise deformation monitoring and the ambiguity of the interferometric phase when targets suffer displacements greater than one-quarter their wavelength ($\lambda/4$) will also be presented.

6. ANALYSIS AND DISCUSSION OF RESULTS

This section will present and discuss the results of the three measurement campaigns performed to evaluate the capabilities of both TLS and TRI systems for detecting and monitoring precursory rock movements (sub-mm scale) of various sizes and at different offsets distances.

6.1. FIRST MEASUREMENT CAMPAIGN

As mentioned in Section 5.1, the first measurement campaign was carried out in Springfield, MO, on November 5, 2017. As noted in Section 5.3.1, measurements with the Faro Focus 3D X130 were discontinued during this campaign and therefore are not presented in this research. The TLS (Leica Scan Station II) data were post-processed within a week, and the results are presented in Figures 6.1 to 6.5 and Tables 6.1 to 6.5. Figure 6.1 and Table 6.1 show that the average error of the measured displacements of the 106 x 76 cm target at an offset distance of 41.58 m can be estimated as 0.249 mm. Figure 6.2 and Table 6.2 show the results of the 61 x 61 cm target at an offset distance of 41.58 m, and the estimated average error is 0.742 mm. It must be pointed out that this target 61 x 61 cm target presented the greatest average error during this measurement campaign. Figure 6.3 and Table 6.3 present the results of the 46 x 31 cm target at an offset distance of 41.58 m, and the estimated average error is 0.431 mm. Figure 6.4 and Table 6.4 present the results of the 20 x 20 cm target at an offset distance of 41.58 m, and the average error is 0.126, which represents the smallest average error measured in this campaign. Finally, the measurements of the 106 x 76 cm target at an offset distance of 90.75 m are presented in Figure 6.5 and Table 6.5, and the average error is 0.230 mm.

From the results presented before, TLS measurements are greatly improved by using post-post processing software. Furthermore, the accuracy of the TLS during the first measurement campaign was approximately 1 mm or better.

The results of the first TRI measurement campaign conducted on November 6, 2017, are not presented in this work because they were not submitted for evaluation. However, on March 12, 2018, Dr. Gómez reported that the phase measurements were off by a factor of two.

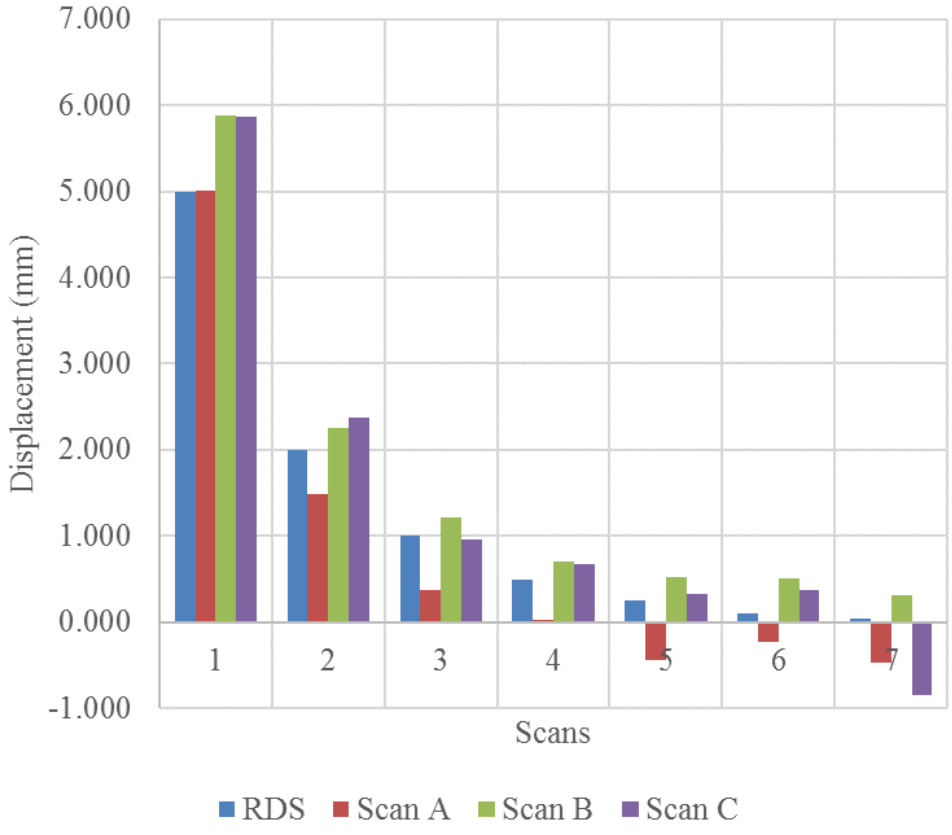

Figure 6.1. TLS results for the 106 x 76 cm steel target at 41.58 m. Rock displacement simulator (RDS) displacements are the actual or ground truth displacements.

Table 6.1. Average error for the 106 x 76 cm steel target at 41.58 m. RDS displacements are the actual displacements.

Reading No	RDS (mm)	Scan A (mm)	Scan B (mm)	Scan C (mm)	Avg Disp (mm)	Error (mm)
1	5.000	5.004	5.885	5.869	5.586	0.586
2	2.000	1.483	2.254	2.380	2.039	0.039
3	1.000	0.375	1.223	0.963	0.854	-0.146
4	0.500	0.035	0.707	0.683	0.475	-0.025
5	0.250	-0.438	0.521	0.327	0.429	0.179
6	0.100	-0.229	0.517	0.379	0.375	0.275
7	0.050	-0.462	0.320	-0.841	0.541	0.491
					Avg. Error =	0.249

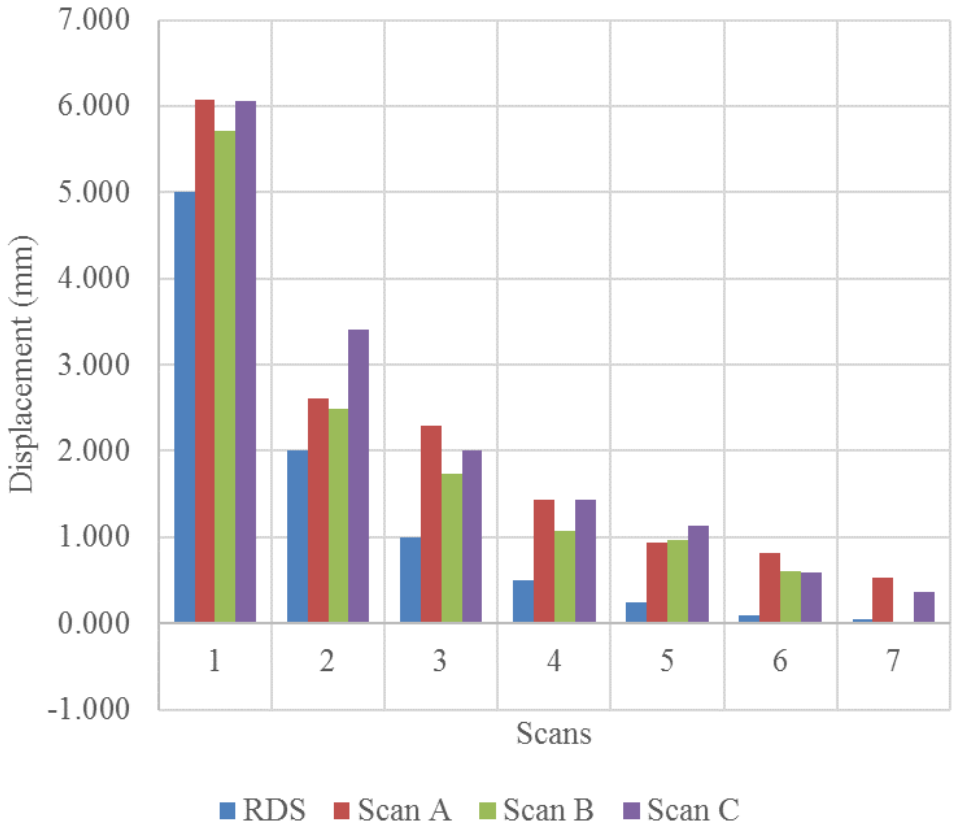

Figure 6.2. TLS results for the 61 x 61 cm steel target at 41.58 m. Rock displacement simulator (RDS) displacements are the actual or ground truth displacements.

Table 6.2. Average error for the 61 x 61 cm steel target at 41.58 m. RDS displacements are the actual displacements.

Reading No	RDS (mm)	Scan A (mm)	Scan B (mm)	Scan C (mm)	Avg Disp (mm)	Avg Error (mm)
1	5.000	6.077	5.710	6.058	5.948	0.948
2	2.000	2.609	2.486	3.402	2.832	0.832
3	1.000	2.296	1.741	2.009	2.015	1.015
4	0.500	1.440	1.074	1.433	1.315	0.815
5	0.250	0.931	0.963	1.129	1.007	0.757
6	0.100	0.812	0.608	0.596	0.672	0.572
7	0.050	0.528	0.008	0.367	0.301	0.251
					Avg. Error =	0.742

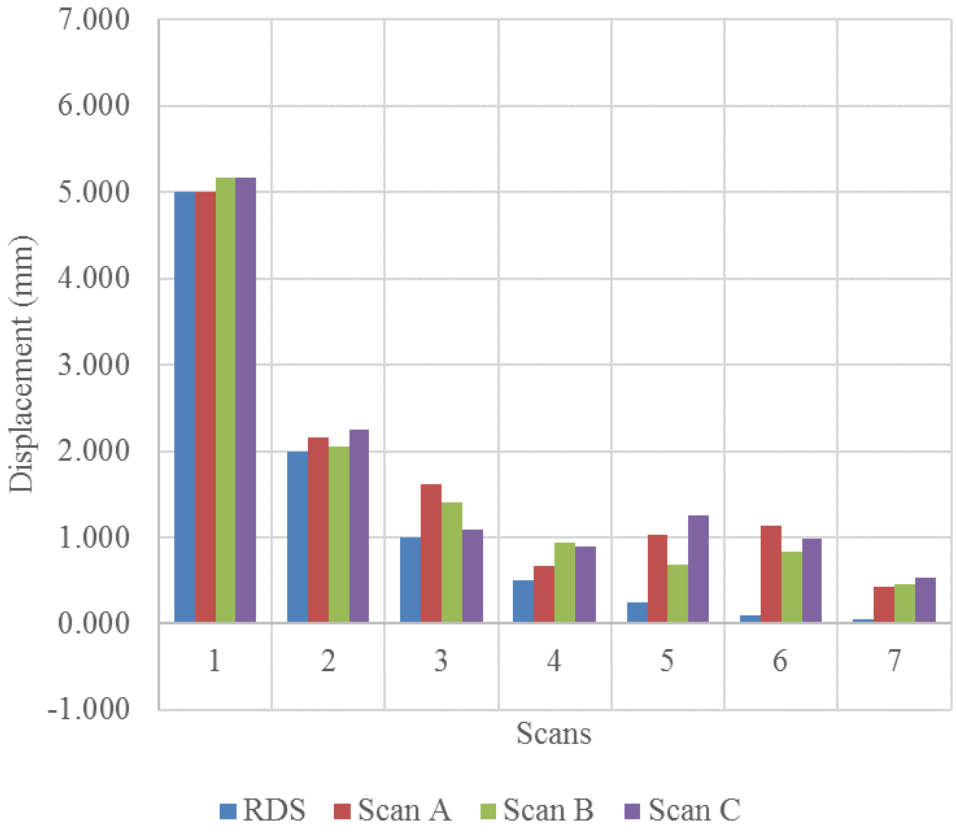

Figure 6.3. TLS results for the 46 x 31 cm steel target at 41.58 m. Rock displacement simulator (RDS) displacements are the actual or ground truth displacements.

Table 6.3. Average error for the 46 x 31 cm steel target at 41.58 m. RDS displacements are the actual displacements.

Reading No	RDS (mm)	Scan A (mm)	Scan B (mm)	Scan C (mm)	Avg Disp (mm)	Avg Error (mm)
1	5.000	4.994	5.162	5.169	5.108	0.108
2	2.000	2.155	2.051	2.255	2.154	0.154
3	1.000	1.614	1.411	1.090	1.372	0.372
4	0.500	0.671	0.938	0.892	0.834	0.334
5	0.250	1.034	0.688	1.259	0.994	0.744
6	0.100	1.141	0.835	0.992	0.989	0.889
7	0.050	0.422	0.452	0.534	0.469	0.419
					Avg. Error =	0.431

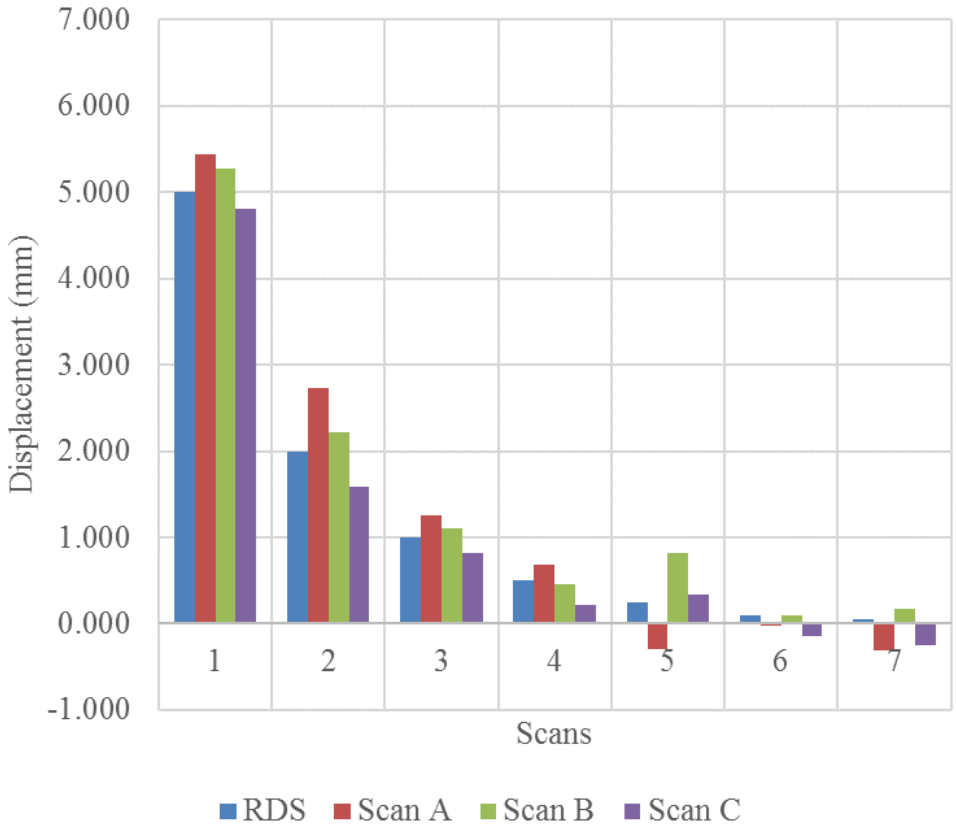

Figure 6.4. TLS results for the 20 x 20 cm steel target at 41.58 m. Rock displacement simulator (RDS) displacements are the actual or ground truth displacements.

Table 6.4. Average error for the 20 x 20 cm steel target at 41.58 m. RDS displacements are the actual displacements.

Reading No	RDS (mm)	Scan A (mm)	Scan B (mm)	Scan C (mm)	Avg Disp (mm)	Avg Error (mm)
1	5.000	5.432	5.266	4.800	5.166	0.166
2	2.000	2.732	2.218	1.583	2.177	0.177
3	1.000	1.252	1.109	0.817	1.059	0.059
4	0.500	0.679	0.458	0.224	0.454	-0.046
5	0.250	-0.288	0.817	0.336	0.480	0.230
6	0.100	-0.023	0.102	-0.142	0.089	-0.011
7	0.050	-0.311	0.170	-0.242	0.241	0.191
					Avg. Error =	0.126

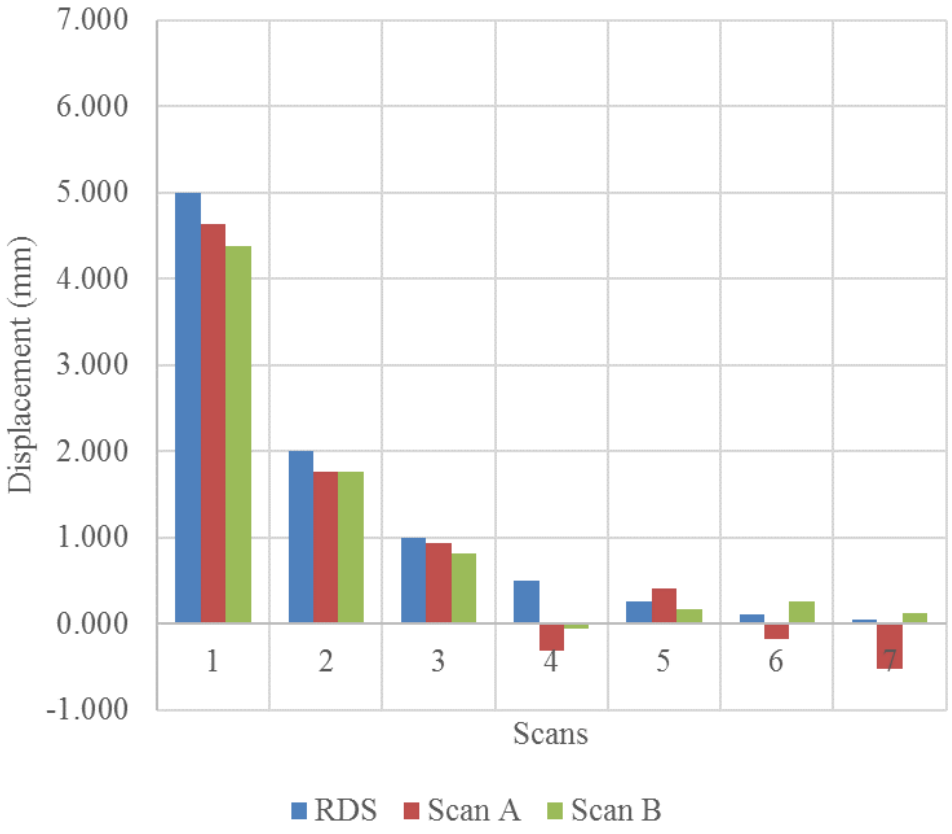

Figure 6.5. TLS results for the 106 x 76 cm steel target at 90.75 m. Rock displacement simulator (RDS) displacements are the actual or ground truth displacements.

Table 6.5. Average error for the 106 x 76 cm steel target at 90.75 m. RDS displacements are the actual displacements.

Reading No	RDS (mm)	Scan A (mm)	Scan B (mm)	Scan C (mm)	Avg Disp (mm)	Avg Error (mm)
1	5.000	4.630	4.371	4.501	4.501	-0.499
2	2.000	1.761	1.754	1.757	1.757	-0.243
3	1.000	0.936	0.810	0.873	0.873	-0.127
4	0.500	-0.322	-0.054	0.188	0.188	-0.312
5	0.250	0.409	0.173	0.291	0.291	0.041
6	0.100	-0.181	0.252	0.216	0.216	0.116
7	0.050	-0.519	0.119	0.319	0.319	0.269
					Avg. Error =	0.230

6.2. SECOND MEASUREMENT CAMPAIGN

As presented in Section 5.1, the second measurement campaign was carried out in Columbia, MO, on April 5, 2018. TLS measurements were performed by Missouri S&T, and they were post-processed within a week. Results of the measurements taken by the Noyafa NF-2680 laser distance measurer were very sporadic, and they are not included in this section. Weather conditions were likely the main factor that caused the Noyafa to malfunction. TRI measurements were taken by MU students under the supervision of Dr. Francisco Gómez. Partial results of the TRI test were submitted to the author on June 4, 2018, and the rest of the results on June 27, 2018 (see Table A.1). The results and comparisons of both TLS and TRI tests are presented in Figures 6.6 to 6.9.

The results of the measured displacements of the 106 x 76 cm target at an offset distance of 42 m are presented in Figure 6.6 and Table 6.6. Six of the seven displacements measured by the TLS instrument are closer to ground truth displacements than those displacements measured by the TRI. TLS errors vary from 0.019 to 0.484 mm, with an

average error of 0.156 mm, while TRI errors vary from 0.099 to 0.311 mm, with an average error of 0.204 mm.

Figure 6.7 and Table 6.7 present the results of the 61 x 61 cm target at an offset distance of 42 m. As can be seen in this figure, the TLS measured displacements for actual displacements of 5, 2, and 1 mm are closer to ground truth displacements than those measured with the TRI. However, the TLS tends to overpredict ground truth displacements of 0.5, 0.25, 0.1, and 0.05 mm, while the TRI tends to underpredict them. TLS errors vary from 0.006 to 0.629 mm, with an average error of 0.305 mm, and TRI errors were estimated between 0.031 to 0.399 mm, with an average error of 0.201 mm.

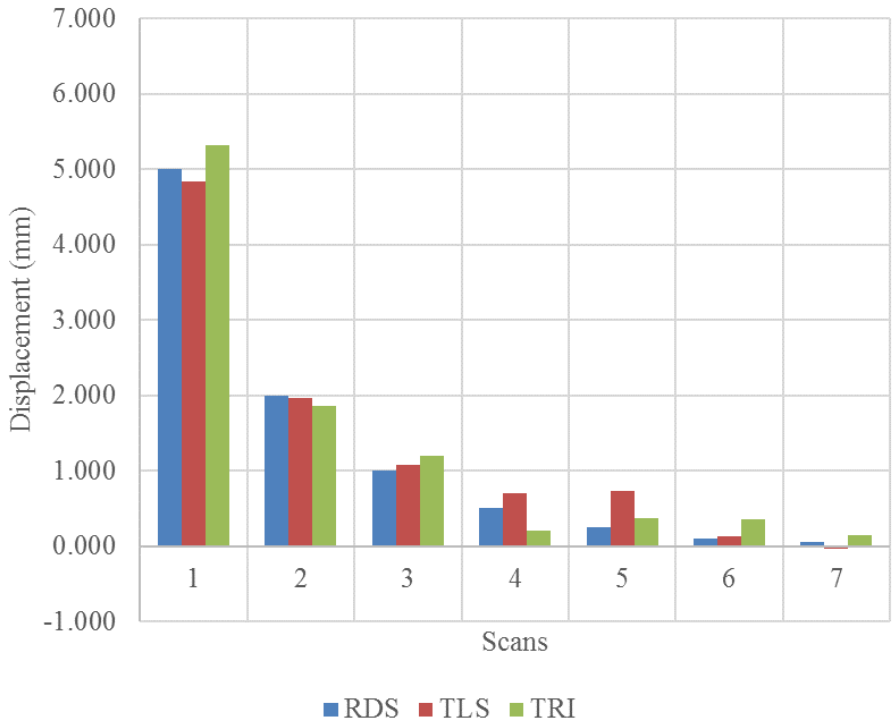

Figure 6.6. Measured displacements of the 106 x 76 cm target at 42 m. Rock displacement simulator (RDS) displacements are the actual or ground truth displacements.

Table 6.6. TLS versus TRI error for the 106 x 76 cm steel target at 42 m. RDS displacements are the actual displacements.

Reading No	RDS (mm)	TLS (mm)	TRI (mm)	TLS Error (mm)	TRI Error (mm)
1	5.000	4.836	-5.311	-0.164	0.311
2	2.000	1.957	-1.852	-0.043	-0.148
3	1.000	1.082	-1.195	0.082	0.195
4	0.500	0.703	-0.197	0.203	-0.303
5	0.250	0.734	-0.366	0.484	0.116
6	0.100	0.133	-0.356	0.033	0.256
7	0.050	-0.031	-0.149	-0.019	0.099
			Avg. Error =	0.156	0.204

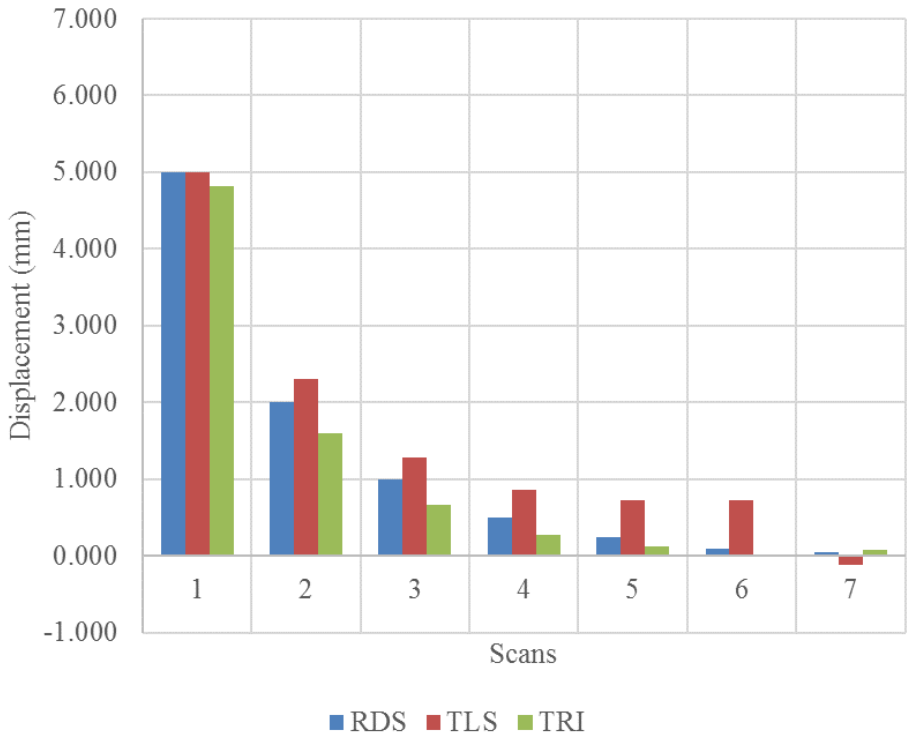

Figure 6.7. Measured displacements of the 61 x 61 cm target at 42 m. Rock displacement simulator (RDS) displacements are the actual or ground truth displacements.

Table 6.7. TLS versus TRI error for the 61 x 61 cm steel target at 42 m. RDS displacements are the actual displacements.

Reading No	RDS (mm)	TLS (mm)	TRI (mm)	TLS Error (mm)	TRI Error (mm)
1	5.000	5.006	-4.817	0.006	-0.183
2	2.000	2.303	-1.601	0.303	-0.399
3	1.000	1.291	-0.669	0.291	-0.331
4	0.500	0.865	-0.276	0.365	-0.224
5	0.250	0.729	-0.118	0.479	-0.132
6	0.100	0.729	0.011	0.629	-0.089
7	0.050	-0.111	-0.081	0.061	0.031
			Avg. Error =	0.319	0.201

Results of the induced displacements on the 46 x 31 cm target at an offset distance of 42 m are shown in Figure 6.8 and Table 6.8. In this case, TLS measured displacements for 5 and 2 mm of movements are closer to ground truth displacements than TRI measurements. TLS errors were estimated between 0.03 to 0.283 mm, with an average error of 0.146 mm, and TRI errors were estimated between 0.008 and 0.140 mm, with an average error of 0.055 mm

The results for the smallest target, 20 x 20 cm at an offset distance of 42 m, are presented in Figure 6.9 and Table 6.9. For ground truth displacements of 5, 2, 1, 0.5, and 0.25, the TLS measurements are in closer agreement to the actual displacements. Nevertheless, the TRI measurements for 0.1 and 0.05 mm of displacements are in closer agreement to the actual displacements. TLS presented an average error of 0.344 mm while TRI presented an average error of 0.658 mm.

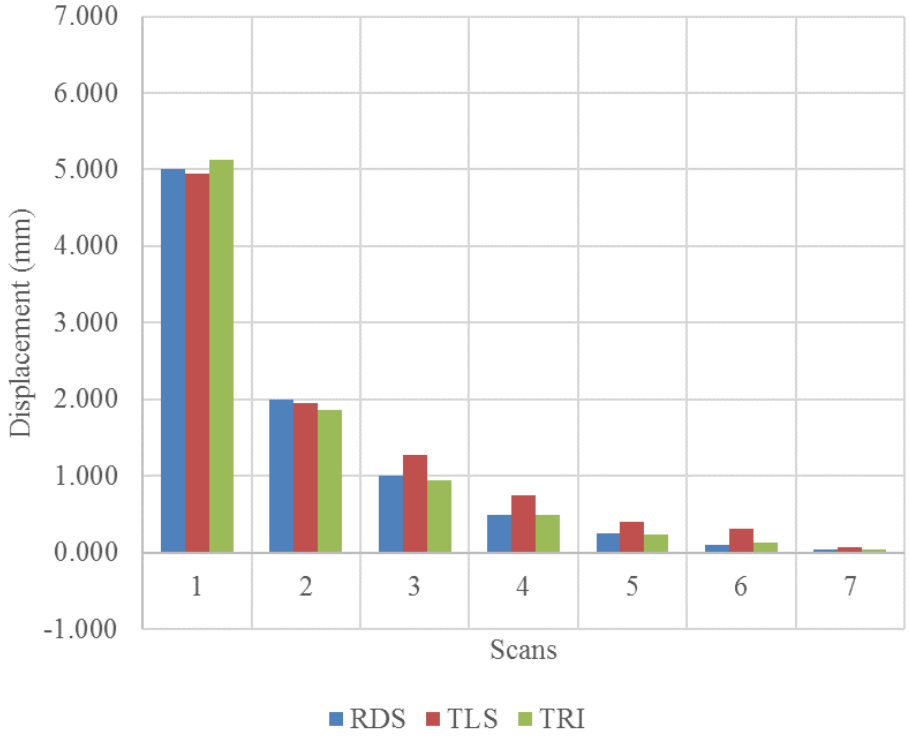

Figure 6.8. Measured displacements of the 46 x 31 cm target at 42 m. Rock displacement simulator (RDS) displacements are the actual or ground truth displacements.

Table 6.8. TLS versus TRI error for the 46 x 31 cm steel target at 42 m. RDS displacements are the actual displacements.

Reading No	RDS (mm)	TLS (mm)	TRI (mm)	TLS Error (mm)	TRI Error (mm)
1	5.000	4.947	-5.123	-0.053	0.123
2	2.000	1.951	-1.860	-0.049	-0.140
3	1.000	1.283	-0.940	0.283	-0.060
4	0.500	0.756	-0.502	0.256	0.002
5	0.250	0.396	-0.232	0.146	-0.018
6	0.100	0.307	-0.137	0.207	0.037
7	0.050	0.080	-0.042	0.030	-0.008
			Avg. Error =	0.146	0.055

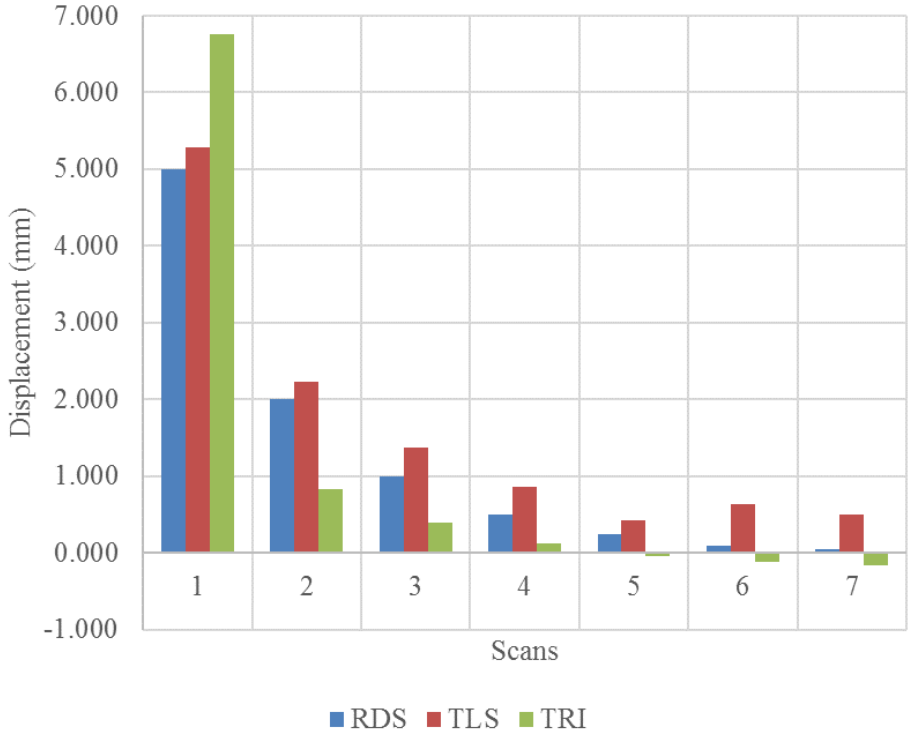

Figure 6.9. Measured displacements of the 20 x 20 cm target at 42 m. Rock displacement simulator (RDS) displacements are the actual or ground truth displacements.

Table 6.9. TLS versus TRI error for the 20 x 20 cm steel target at 42 m. RDS displacements are the actual displacements.

Reading No	RDS (mm)	TLS (mm)	TRI (mm)	TLS Error (mm)	TRI Error (mm)
1	5.000	5.283	-6.752	0.283	1.752
2	2.000	2.232	-0.836	0.232	-1.164
3	1.000	1.369	-0.396	0.369	-0.604
4	0.500	0.861	-0.120	0.361	-0.380
5	0.250	0.424	0.034	0.174	-0.216
6	0.100	0.635	0.113	0.535	0.013
7	0.050	0.502	0.160	0.452	0.110
			Avg. Error =	0.344	0.658

As discussed above, the TLS system estimated ground truth displacements greater than 0.5 mm very accurately. TLS measurements for 5, 2, and 1 mm are closer to ground truth data than TRI measurements. TRI measurements are slightly closer to ground truth displacement for 0.5, and 0.25 mm. Gómez (June 4, 2018), stated the following: "I think we can safely say that the radar cannot really detect the 0.10 and smaller displacements. In general, it seems to detect movement at the 0.25 mm displacement, although it is noisy." Furthermore, TRI measurements for the smallest target (20 x 20 cm) present the biggest errors of the four targets used in this research.

As presented in Section 5.4.1, displacements larger than one quarter the wavelength ($\lambda/4$) of the TRI were simulated using the RDS. These tests were performed using the 61 x 61 cm target at an offset distance of 42 m. The target was displaced at the following displacements: 7, 9, 18, 18, 26, and 36 mm. Gómez (June 27, 2018) reported that TLS results were used to calculate the number of wavelength cycles in order to calculate the total target displacements (see Table A.2). The results are presented in Figure 6.10 and Table 6.10. As can be seen in Table 6.10, TLS errors vary between 0.512 and 1.043 mm, while TRI errors vary between 0.2 and 7.4 mm.

The results presented in Figure 6.10 are of particular importance for this research. Even with TLS data, TRI errors were calculated in the order of millimeters due to phase ambiguities. This problem has been pointed out in Section 2 and 4 and is a limitation of TRI systems in addition to the time required to reduce the data. TLS data can be post-processed in a week compared to TRI data that takes from two to three months to post-process. The amount of time required to post-process TRI data may not be acceptable in

real slope stability problems along highway corridors (i.e., user's safety, economic impact of keeping a highway corridor closed, etc.).

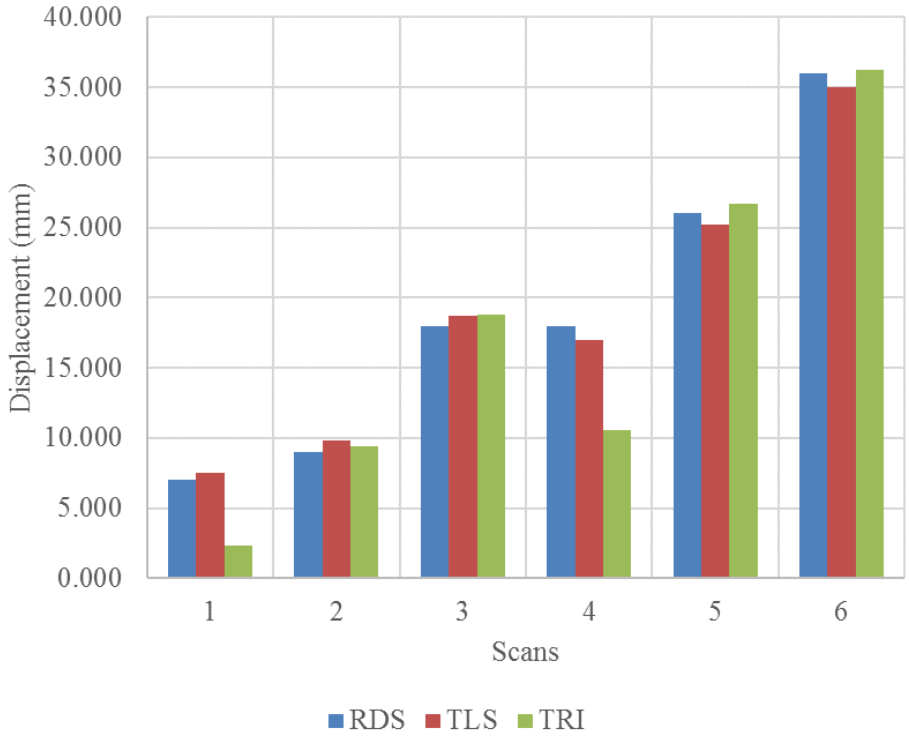

Figure 6.10. Results of measured displacements greater than one quarter the wavelength of the TRI. The 61 x 61 cm target was positioned an offset distance of 42 m. Rock displacement simulator (RDS) displacements are the actual or ground truth displacements.

The results of the measured displacements of the pseudo rock are presented in Figure 6.11. As it can be seen, both the TLS and TRI show measured displacements very close to ground truth displacements. The measured errors for both scanners are less than 0.2 mm as shown in Table 6.11. These results show that sub-millimetric displacements can be detected using TLS and post-processing software.

Table 6.10. TLS and TRI results and errors for displacements greater than one quarter the wavelength of the TRI.

Reading No	RDS (mm)	TLS (mm)	TRI (mm)	TLS Error (mm)	TRI Error (mm)
1	7.000	7.512	-2.300	0.512	-4.700
2	9.000	9.793	-9.400	0.793	0.400
3	18.000	18.730	-18.800	0.730	0.800
4	18.000	16.957	-10.600	-1.043	-7.400
5	26.000	25.215	-26.700	-0.785	0.700
6	36.000	34.992	-36.200	-1.008	0.200
			Avg. Error =	0.812	2.367

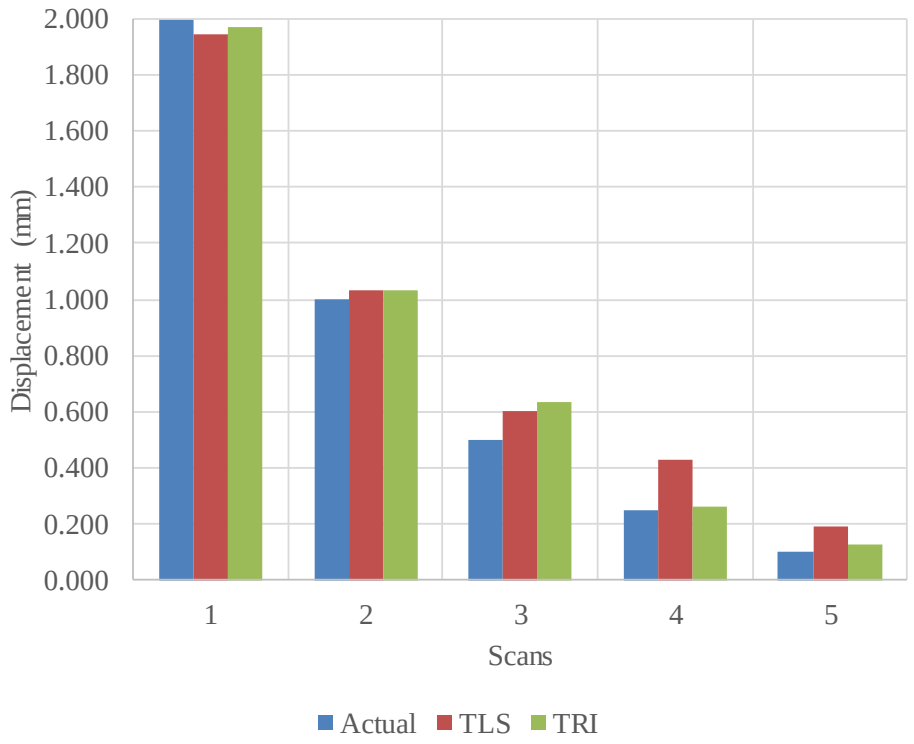

Figure 6.11. Results of the pseudo rock displacements.

Table 6.11. Pseudo rock measurements 43 m.

Reading No	Actual	TLS	TRI	TLS Error	TRI Error
1	2.000	1.943	-1.969	-0.057	-0.031
2	1.000	1.033	-1.031	0.033	0.031
3	0.500	0.604	-0.636	0.104	0.136
4	0.250	0.432	-0.264	0.182	0.014
5	0.100	0.189	-0.126	0.089	0.026
			Avg. Error =	0.093	0.048

6.3. THIRD MEASUREMENT CAMPAIGN

As presented in Section 5.1, the third measurement campaign was carried out in the Student Recreation Center of Missouri S&T, on January 2018. TLS measurements were performed by Missouri S&T students and post-processed within a week. TRI measurements were taken by Dr. Francisco Gómez from MU with help from his students. The results and comparisons of both TLS and TRI tests are presented in this section.

Before analyzing the results of this measurement campaign, the following terms must be defined:

1. ΔRDS is the RDS displacement. It is the ground truth data. A negative number means the target is moving towards the TRI or TLS. A positive number means the target is moving away from the TLS or TRI.
2. RDS_n is the average distance between the TRI and the RDS measured with the Bosch GLR 825 for an n observation.
3. TRI_n is the average distance between the TRI and a reference target behind the TRI measured with the Bosch GLR 825 for an n observation.

4. ΔRDS_{Bosch} is the RDS displacement measured with the Bosch GLR 825. It can be determined using the following equation:

$$\Delta RDS_{Bosh} = RDS_{n+1} - RDS_1 \quad (6.1)$$

where the subscript *1* is the base or first reading and *n+1* is the subsequent reading.

5. ΔTRI is the TRI displacement measured with the Bosch GLR 825. It can be determined using the following equation:

$$\Delta TRI = TRI_{n+1} - TRI_1 \quad (6.2)$$

where the subscript *1* is the base or first reading and *n+1* is the subsequent reading. A negative number means that the TRI is moving towards a reference target behind the TRI. A positive number means that the TRI is moving away from a reference target behind the TRI.

6. ΔRDS_C is the RDS displacement corrected for TRI repositioning error. It can be estimated using the following equation:

$$\Delta RDS_C = \Delta RDS_{Bosh} + \Delta TRI. \quad (6.3)$$

7. ΔRDS_E is the measured RDS error. It is the difference between the ground truth displacement and ΔRDS_C. It can be computed as

$$\Delta RDS_E = \Delta RDS - \Delta RDS_C. \quad (6.4)$$

8. The average measurement errors ($\Delta RDS_{E\text{-}Avg}$) can be computed using the following equation:

$$\Delta RDS_{E-Avg} = \frac{\sum \Delta RDS_E}{n} \quad (6.5)$$

where *n* is the number of observations.

9. The true phase integer and the experimental phase integer can be computed using the following equations:

$$True\ Phase\ Integer = \frac{RDS}{\lambda/2} \tag{6.6}$$

$$Bosh\ Phase\ Integer = \frac{\Delta RDS_{Bosh-Rev}}{\lambda/2} \tag{6.7}$$

where λ is the wavelength of the TRI, which is 17.2 mm for the TRI used in this research.

10. . TLS_n is the average distance between the TLS and the RDS measured with the Leica Scan Station II or P40 for an *n* observation.
11. ΔTLS is the RDS displacement measured with the Leica Scan Station II or P40. It can be determined using the following equation:

$$\Delta TLS = TLS_{n+1} - TLS_1 \tag{6.8}$$

where the subscript *1* is the base or first reading and *n+1* is the subsequent reading. A negative number means that the RDS is moving towards the TLS. A positive number means that the RDS is moving away from the TLS.

12. ΔTLS_E is the measured RDS error. It is the difference between the ground truth displacement and ΔTLS. It can be computed as

$$\Delta TLS_E = \Delta RDS - \Delta TLS. \tag{6.9}$$

13. The average TLS measurement errors ($\Delta TLS_{E\text{-}Avg}$) can be computed using the following equation:

$$\Delta TLS_{E-Avg} = \frac{\sum \Delta TLS_E}{n}. \tag{6.10}$$

14. The average TLS base ($\Delta TLS_{B\text{-}Avg}$) is the average reading for zero RDS displacements, and it can be computed as

$$\Delta TLS_{B-Avg} = \frac{TLS_{Test\ K} + TLS_{Test\ R}}{2}. \quad (6.11)$$

Test A was discarded as a base reading because of human error.

Table 6.12 presents the *ΔRDS* displacements measured with the handheld Bosch measurement device (ΔRDS_{Bosch}). For such a small and relatively inexpensive device, compared to the TRI and TLSs used in this research, its accuracy is very good. As we can see in Table 6.12, the accuracy of the Bosch GLR 825 is below the wavelength (λ = 17.2 mm) of the radar used in this research. Furthermore, ΔRDS_{Bosch} can be used to constrain ambiguities when displacements are greater than one quarter of the wavelength *(λ/4*) of the radar, as suggested by Caduff et al. (2015).

Table 6.13 presents the measured TRI displacements after repositioning the apparatus over a mark on the floor using a laser plummet. Repositioning errors varied from 0.6 mm to 1.4 mm. This finding agrees with what Wujanz et al. (2013) called the TRI single standpoint problem. According to the authors, even when the precision of TRI systems can be assumed to be less than 1 mm, such precision cannot be attained during discontinuous measurements campaigns. Monserrat et al. (2014) also pointed out that TRI data can contain errors due to the repositioning of the TRI between different campaigns. The authors stated the following: "These errors are usually non-negligible, especially if "light positioning" is performed, e.g. by simply materializing the GBSAR location using some marks." Nevertheless, as pointed out in Section 3.1.7, ΔTRI can be used as a geometric phase component in Equation 3.13 to correct for repositioning errors between two discontinuous measurement campaigns.

Table 6.12. Results of the measured displacements of the 61x61 cm target using the Bosch GLR 825.

Reading No	ΔRDS (mm)	Test Name	Bosch Readings (m)				RDS_n (m)	ΔRDS_{Bosch} (mm)
			1	2	3	4		
1	0.0	A-F	41.609	41.609	41.606	41.608	41.608	0.0
3	-0.5	B-F	41.607	41.607	41.608	41.606	41.607	-1.0
5	-0.7	C-F	41.605	41.604	41.605	41.606	41.605	-3.0
7	-1.0	D-F	41.606	41.608	41.608	41.606	41.607	-1.0
9	-2.0	E-F	41.605	41.605	41.606	41.606	41.606	-2.5
11	-6.0	F-F	41.600	41.600	41.600	41.600	41.600	-8.0
13	-12.0	G-F	41.594	41.595	41.595	41.595	41.595	-13.3
15	-15.0	H-F	41.591	41.592	41.592	41.591	41.592	-16.5
17	-20.0	I-F	41.589	41.586	41.589	41.587	41.588	-20.3
19	-28.0	J-F	41.580	41.582	41.578	41.578	41.580	-28.5
21	0.0	K-F	41.607	41.607	41.607	41.606	41.607	-1.3
23	-7.0	M-F	41.598	41.598	41.598	41.598	41.598	-10.0
24	-9.0	N-F	41.599	41.598	41.597	41.596	41.598	-10.5
25	-18.0	O-F	41.588	41.589	41.589	41.589	41.589	-19.3
26	-26.0	P-F	41.581	41.580	41.579	41.582	41.581	-27.5
27	-36.0	Q-F	41.570	41.572	41.572	41.572	41.572	-36.5
28	0	R-F	41.606	41.605	41.606	41.606	41.606	-2.3

Table 6.14 presents the RDS displacements corrected for TRI repositioning errors (ΔRDS_C). These results are in close agreement to the ground truth displacements (ΔRDS). Test M (Reading 23) presents a high ΔRDS_E. This might have been caused by human error while taking or transcribing the Bosch readings. These kinds of errors can be reduced in future research by attaching the compact lidar unit to the tower of the TRI and using a lidar unit capable of transmitting the data over a wireless connection to a computer or readout unit. Nevertheless, the average measurement error ($\Delta RDS_{E\text{-}Avg}$) is sub-millimetric (0.6 mm).

Table 6.13. Results of the measured repositioning displacements of the TRI using the Bosch GLR 825.

Reading No	*ΔRDS* (mm)	Test Name	Readings (m)				TRI_n (m)	*ΔTRI* (mm)
			1	2	3	4		
2	0	A-B	3.4881	3.4899	3.4898	3.4881	3.4890	--
4	-0.5	B-B	3.4862	3.4857	3.4859	3.4865	3.4861	0.0
6	-0.7	C-B	3.4876	3.4876	3.4871	3.4876	3.4875	1.4
8	-1	D-B	3.4872	3.4873	3.4871	3.4871	3.4872	1.1
10	-2	E-B	3.4866	3.4868	3.4857	3.4868	3.4865	0.4
12	-6	F-B	3.4874	3.4875	3.4873	3.4876	3.4875	1.4
14	-12	G-B	3.4865	3.4869	3.4869	3.4870	3.4868	0.8
16	-15	H-B	3.4866	3.4867	3.4869	3.4867	3.4867	0.7
18	-20	I-B	3.4862	3.4864	3.4867	3.4867	3.4865	0.4
20	-28	J-B	3.4865	3.4866	3.4865	3.4864	3.4865	0.4
22	0	K-B	3.4865	3.4869	3.4869	3.4864	3.4867	0.6
22	-7	K-B	3.4865	3.4869	3.4869	3.4864	3.4867	0.6
22	-9	K-B	3.4865	3.4869	3.4869	3.4864	3.4867	0.6
22	-18	K-B	3.4865	3.4869	3.4869	3.4864	3.4867	0.6
22	-26	K-B	3.4865	3.4869	3.4869	3.4864	3.4867	0.6
22	-36	K-B	3.4865	3.4869	3.4869	3.4864	3.4867	0.6
22	0	K-B	3.4865	3.4869	3.4869	3.4864	3.4867	0.6

Using the computed ΔRDS_C, the phase integer value was computed and presented in the last column of Table 6.14. Except for Test M (Reading 23), the computed phase integers agree with the ground truth phase integers. As presented in Section 3.1.8, phase unwrapping is a critical issue in terrestrial radar interferometry. The computed Bosch phase integers presented in Table 6.14 can be used to constrain the results when displacements exceed multiple wavelengths, as suggested by Caduff et al. (2015).

The RDS displacements measured with the Leica Scan Station II are presented in Table 6.15. The *ΔTLS* were determined by using the average of Readings 21 and 28. Reading 1 was not included in the average because of human error during that reading. As

can be seen in Table 6.15, the measured RDS displacements (ΔTLS) are in very close agreement with ground truth displacements (RDS). Furthermore, the average error ($\Delta TLS_{E\text{-}Avg}$) is 0.18 mm. This agrees with the results presented in the previous section, namely that post-processed TLS data can detect sub-millimetric movements of rock.

Table 6.14. RDS displacements corrected for average TRI repositioning errors using the data collected with the Bosch GLR 825.

Reading No	ΔRDS (mm)	Test Name	ΔRDS_{Bosch} (mm)	ΔRDS_C (mm)	ΔRDS_E (mm)	True Phase Integer	Bosch Phase Integer
1	0	A-F	0.0	--	--	0	0
3	-0.5	B-F	-1.0	-1.0	0.5	0	0
5	-0.7	C-F	-3.0	-1.6	0.9	0	0
7	-1.0	D-F	-1.0	0.1	-1.1	0	0
9	-2.0	E-F	-2.5	-2.1	0.1	0	0
11	-6.0	F-F	-8.0	-6.6	0.6	0	0
13	-12.0	G-F	-13.3	-12.5	0.5	1	1
15	-15.0	H-F	-16.5	-15.9	0.9	1	1
17	-20.0	I-F	-20.3	-19.3	-0.7	2	2
19	-28.0	J-F	-28.5	-28.1	0.1	3	3
21	0.0	K-F	-1.3	-0.7	0.7	0	0
23	-7.0	M-F	-10.0	-9.4	2.4	0	1
24	-9.0	N-F	-10.5	-9.9	0.9	1	1
25	-18.0	O-F	-19.3	-18.7	0.7	2	2
26	-26.0	P-F	-27.5	-26.9	0.9	3	3
27	-36.0	Q-F	-36.5	-35.9	-0.1	4	4
28	0.0	R-F	-2.3	-1.7	1.7	0	0
				$\Delta RDS_{E\text{-}Avg}$	0.6		

The RDS displacements measured with the Leica Scan Station P40 are presented in Table 6.16. The ΔTLS were determined by using the average of Readings 1, 21 and 28.

As can be seen in Table 6.16, the measured RDS displacements (ΔTLS) are in very close agreement with ground truth displacements (RDS). The average error ($\Delta TLS_{E\text{-}Avg}$) is 0.30 mm. One more time, the results indicate that TLS with post-processing software can be used to detect sub-millimetric movements of rock.

Table 6.15. Results of the measured displacements of the 61x61 cm target using the Leica Scan Station II.

Reading No	*ΔRDS* (mm)	Test Name	TLS Readings (mm)			TLS_n (mm)	*ΔTLS* (mm)	ΔTLS_E (mm)
			1	2	3			
1	0.0	A-F	41602.2	41602.2	41602.1	41602.2	--	--
3	-0.5	B-F	41603.3	41603.3	41603.2	41603.3	-0.38	-0.12
5	-0.7	C-F	41602.7	41603.0	41603.0	41602.9	-0.76	0.06
7	-1.0	D-F	41602.6	41602.6	41602.7	41602.6	-1.03	0.03
9	-2.0	E-F	41601.7	41601.6	41601.8	41601.7	-1.97	-0.03
11	-6.0	F-F	41597.3	41597.5	41597.4	41597.4	-6.27	0.27
13	-12.0	G-F	41591.5	41591.4	41591.4	41591.4	-12.25	0.25
15	-15.0	H-F	41588.4	41588.6	41588.6	41588.5	-15.15	0.15
17	-20.0	I-F	41583.6	41583.4	41583.4	41583.5	-20.20	0.20
19	-28.0	J-F	41575.7	41575.6	41575.4	41575.6	-28.11	0.11
21	0.0	K-F	41603.2	41603.6	41603.5	41603.4	-0.24	0.24
23	-7.0	M-F	41596.3	41596.3	41596.4	41596.3	-7.32	0.32
24	-9.0	N-F	41594.4	41594.4	41594.5	41594.4	-9.24	0.24
25	-18.0	O-F	41585.4	41585.5	41585.6	41585.5	-18.13	0.13
26	-26.0	P-F	41577.4	41577.4	41577.3	41577.4	-26.26	0.26
27	-36.0	Q-F	41567.4	41567.5	41567.6	41567.5	-36.18	0.18
28	0.0	R-F	41603.9	41603.9	41603.9	41603.9	0.24	-0.24
					$\Delta TLS_{B\text{-}Avg}$ =	41603.7	$\Delta TLS_{E\text{-}Avg}$=	0.18

TRI results were submitted to us by Dr. Gómez on February 12, 2019 (see Table A.3). These results are compared to both TLS and Bosch results on Figure 6.12 and Table 6.17. As can be seen, TLS errors for the Leica Scan Station II vary between -0.03 to 0.32

mm, and TLS errors for the Leica Scan Station P40 vary from 0.00 to 1.22 mm. On the other hand, TRI errors vary between 0.03 to 8.47 mm. These results are similar to the results presented in Section 6.2. Even with TLS data, TRI can overpredict displacements in the order of several millimeters due to ambiguities related to the direction of movement of the target (i.e. towards or away from the TRI). This is a serious limitation of TRI systems. Furthermore, the time required to process the data (one week versus five weeks) limits the applicability of TRI systems for highway projects.

Table 6.16. Results of the measured displacements of the 61x61 cm target using the Leica Scan Station P40.

Reading No	ΔRDS (mm)	Test Name	TLS Readings (mm)			TLS_n (mm)	ΔTLS (mm)	ΔTLS_E (mm)
			1	2	3			
1	0.0	A-F	41787.1	41787.1	41787.1	41787.1	-0.11	0.11
3	-0.5	B-F	41786.7	41786.8	41786.8	41786.8	-0.45	-0.05
5	-0.7	C-F	41786.6	41786.5	41786.6	41786.6	-0.70	0.00
7	-1.0	D-F	41786.3	41786.3	41786.3	41786.3	-0.97	-0.03
9	-2.0	E-F	41785.4	41785.3	41785.3	41785.3	-1.96	-0.04
11	-6.0	F-F	41781.2	41781.2	41781.2	41781.2	-6.08	0.08
13	-12.0	G-F	41775.5	41775.5	41775.5	41775.5	-11.77	-0.23
15	-15.0	H-F	41772.5	41772.6	41772.5	41772.5	-14.71	-0.29
17	-20.0	I-F	41767.8	41767.8	41767.8	41767.8	-19.49	-0.51
19	-28.0	J-F	41760.1	41760.1	41760.1	41760.1	-27.18	-0.82
21	0.0	K-F	41787.3	41787.2	41787.3	41787.3	0.02	-0.02
23	-7.0	M-F	41780.2	41780.1	41780.2	41780.2	-7.08	0.08
24	-9.0	N-F	41778.4	41778.5	41778.4	41778.4	-8.84	-0.16
25	-18.0	O-F	41769.7	41769.7	41769.7	41769.7	-17.53	-0.47
26	-26.0	P-F	41761.9	41762.1	41762.0	41762.0	-25.26	-0.74
27	-36.0	Q-F	41752.5	41752.5	41752.5	41752.5	-34.78	-1.22
28	0.0	R-F	41787.4	41787.3	41787.3	41787.3	0.10	-0.10
					$\Delta TLS_{B\text{-}Avg}$ =	41787.3	$\Delta TLS_{E\text{-}Avg}$=	0.30

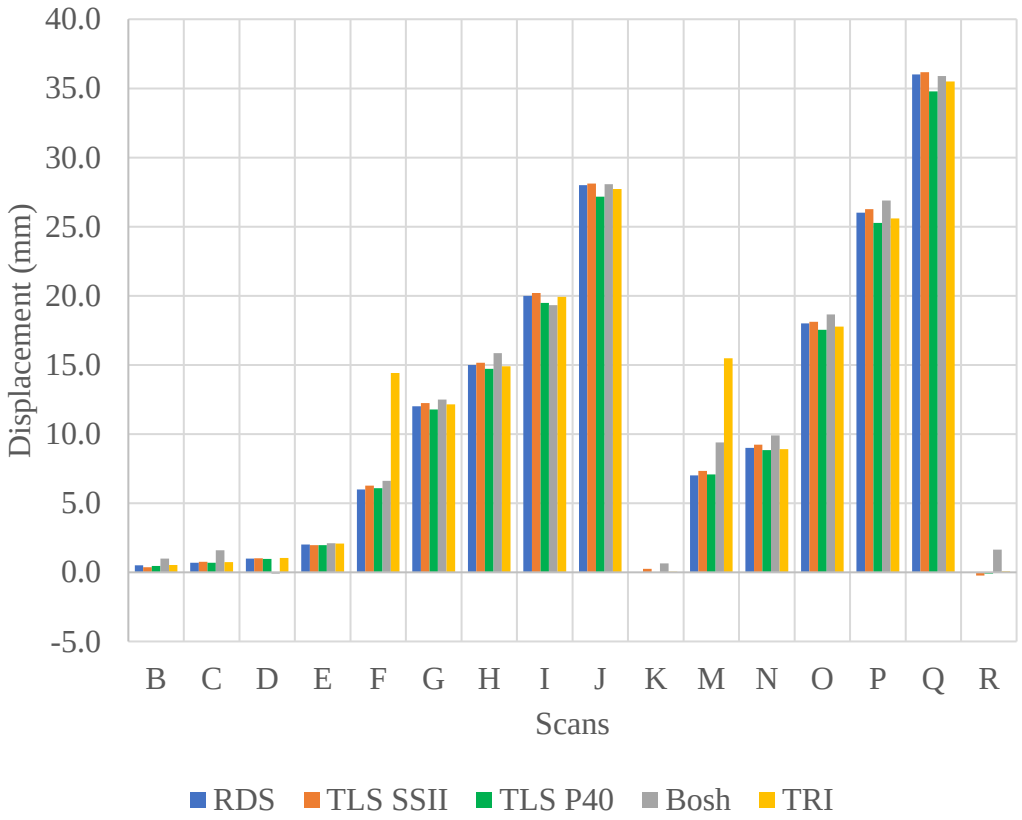

Figure 6.12. Results of measured displacements for the third measurement campaign. The 61 x 61 cm target was positioned an offset distance of approximately 42 m. Rock displacement simulator (RDS) displacements are the actual or ground truth displacements.

6.4. SUMMARY

Results of the three measurement campaigns show that sub-millimetric displacements can be detected with both TLS and TRI systems. TLS data was post processed with the Missouri S&T Lidar Software developed by Boyko (2014). The Missouri S&T Lidar Software computes average displacements of the targets. The Leica Scan Station II has a single point accuracy distance of 4 mm, as can be seen in Table 4.2. However, using the Missouri S&T Lidar Software, sub-millimetric displacements (<0.5

mm) of the RDS were measured. Sub-millimetric displacements were also measured with the TRI. In this research, displacements as small as 0.25 mm were detected with the TRI. Displacements measured with both TLS and TRI were in close agreement with ground truth displacements. Furthermore, TLS accuracy was as good as TRI accuracy.

Table 6.17. TLS SSII, TLS P40, Bosch, and TRI results and errors for the third measurement campaign.

Reading No	*ΔRDS* (mm)	Test Id.	*ΔTLS* SSII (mm)	*ΔTLS* P40 (mm)	*ΔBosch* (mm)	*ΔGPIR* (mm)	*ΔTLS* Error SSII (mm)	*ΔTLS* Error P40 (mm)	*ΔBosch* Error (mm)	*ΔGPIR* Error (mm)
1	0.00	A	--		--	--	--	--	--	--
3	0.50	B	0.38	0.45	1.00	0.53	0.12	0.05	0.50	0.03
5	0.70	C	0.76	0.70	1.60	0.74	0.06	0.00	0.90	0.04
7	1.00	D	1.03	0.97	-0.10	1.03	0.03	0.03	1.10	0.03
9	2.00	E	1.97	1.96	2.10	2.08	0.03	0.04	0.10	0.08
11	6.00	F	6.27	6.08	6.63	14.41	0.27	0.08	0.63	8.41
13	12.00	G	12.25	11.77	12.50	12.15	0.25	0.23	0.50	0.15
15	15.00	H	15.15	14.71	15.85	14.89	0.15	0.29	0.85	0.11
17	20.00	I	20.20	19.49	19.33	19.93	0.20	0.51	0.67	0.07
19	28.00	J	28.11	27.18	28.08	27.71	0.11	0.82	0.08	0.29
21	0.00	K	0.24	-0.02	0.65	0.05	0.24	0.02	0.65	0.05
23	7.00	M	7.32	7.08	9.40	15.47	0.32	0.08	2.40	8.47
24	9.00	N	9.24	8.84	9.90	8.90	0.24	0.16	0.90	0.10
25	18.00	O	18.13	17.53	18.65	17.76	0.13	0.47	0.65	0.24
26	26.00	P	26.26	25.26	26.90	25.58	0.26	0.74	0.90	0.42
27	36.00	Q	36.18	34.78	35.90	35.50	0.18	1.22	0.10	0.50
28	0.00	R	-0.24	-0.10	1.65	0.06	0.24	0.10	1.65	0.06
						Average Errors =	0.18	0.30	0.79	1.19

An independent measurement device, the Bosch GLR 825, with an accuracy below the wavelength of the radar (λ = 17.2 mm) was used to constrain the results of the TRI

when displacements exceeded one quarter the wavelength ($\lambda/4$) of the radar or when displacements exceeded multiple wavelengths of the radar. The independent measurement device can provide valuable information for overcoming the single standpoint problem of the TRI due to repositioning errors during discontinuous measurement campaigns.

7. CONCLUSIONS AND RECOMMENDATIONS

This work presented a comparative experimental study between TLS and TRI. Steel targets of different sizes were constructed and mounted on a rock displacement simulator (RDS) capable of simulating sub-millimetric rock movements. The Leica Scan Station II of the Missouri University of Science and Technology (Missouri S&T) and the Gamma Portable Interferometric Radar (GPIR) of the University of Missouri at Columbia (MU) were the main equipment used in this study. The comparative experimental study shows that both TLS and TRI can be used to detect sub-millimetric displacements. A compact lidar unit (i.e., Bosch GLR 825) was used as an independent measurement device to constrain the results of the TRI when rock displacements exceeded multiple wavelengths of the instrument or when displacements exceeded one quarter the wavelength of the instrument. It is proposed that measurements taken with a compact lidar unit can be used to correct TRI measurement for repositioning errors during discontinuous measurement campaigns.

7.1. CONCLUSIONS

In conclusion, the results of the measurement campaigns carried out in this research extended out knowledge on methods for detecting precursory rock movements. The experiments carried out in this research have shown that both TRI and TLS systems can detect sub-millimetric displacements of single rock targets. Specifically, this research led to the following findings:

1. TLS data post-processed with the Missouri S&T Lidar Software can detect sub-millimetric displacements. The accuracy of the TLS (SSII) improved from its native resolution of 5 mm to less than 0.5 mm.
2. TRI can detect displacements as small as 0.25 mm during continuous measurement campaigns. A compact lidar unit attached to the TRI can be used to solve ambiguities when rock displacements exceed multiple wavelengths or exceed one quarter the wavelength of the TRI.
3. TRI line-of-sight (LOS) position with respect to a fixed target behind the instrument can be acquired and later used to provide information about repositioning errors during discontinuous measurement campaigns.

These findings appear to confirm the hypothesis presented in Section 1.5. That is, TLS measurements can be used to calibrate the TRI method after repositioning, and TLS can be used to identify the approximate range of the target to a resolution of less than the ambiguity range of half the wavelength of the TRI.

The TRI system (Gamma GPIR II) used in this research suffered from several limitations. Some of these limitations were the following:

1. Millimetric changes in the position of the instrument during simulated discontinuous measurement campaigns dramatically reduced the accuracy of the measurements. Repositioning errors in the same order of magnitude as the measured RDS displacements were measured with the Bosch laser measurement device. These errors were non-negligible and could not be avoided by simply materializing the TRI location using marks on the ground.

2. Ambiguities related to the interferometric phases caused biased deformation estimates, especially when the RDS displacements exceeded one quarter the wavelength ($\lambda/4$) of the instrument. In this research, deformation estimates with absolute errors of several millimeters (i.e., 7.4 mm during the second measurement campaign and 8.47 mm during the third measurement campaign) were detected.
3. Post-processing the TRI data took several weeks. This limitation is critical for active landslides or rockslides, and it could seriously limit the applicability of TRI systems for highway corridors or any other project where human lives are at stake.
4. Only displacements parallel to line of sight (LOS) between the TRI and the target of interest can be detected. The TRI had to be placed perpendicular to the targets during this research.
5. The TRI was top heavy, requiring very flat surfaces for its deployment. This limits its applicability on rolling terrain or during windy conditions.
6. No metal objects can be between the TRI and the target. Also, no metal objects can be behind the target of interest. The exposed surfaces of the tall steel bracket system used during the first measurement campaign caused the phase measurements to be off by a factor of two. In this research, this problem was overcome by using a short frame and by using a target large enough to cover all the components of the RDS.

Perhaps the main advantage of the TRI system used in this research was the short time required to measure the displacements of the RDS. The TRI was able to take a reading of the RDS in seconds, compared to a couple of minutes required by the TLSs.

The main limitation of the TLS systems used in this research was that their single-point accuracy was in the order of millimeters. However, as presented in Section 6, TLS accuracy was greatly improved by using the Missouri S&T Lidar Software that incorporates averaging techniques. Using this approach, sub-millimetric accuracy was achieved in this research.

TLS systems have several advantages over TRI systems. TLS systems are lighter, cheaper, and easier to operate. In addition, the data can be reduced faster, and the results are easier to visualize. All of these represent big advantages for rock slope evaluation in highway projects, especially when time represents an economic cost for the state and when the press requires timely reports from the state's Department of Transportation.

7.2. RECOMMENDATIONS

Further measurement campaigns under controlled conditions should include measurements at further line-of-sight distances. Only one test at 90 m could be performed due to space limitations in controlled environments. Airplane hangar buildings can be used for such tests.

In this research, sampling densities of 1x1 mm were used. Measurement campaigns with larger sampling densities should be carried out, and the results should be compared with TRI results for the same targets.

The Missouri S&T Lidar Software was used in this research to determine displacements from point clouds. However, other methods have been proposed by Abellán

et al. (2009) and Kromer et al. (2015). Further research using other methods can help to select the best point-cloud displacement method to detect precursory rock movements.

It is commonly taken for granted that setup-repositioning errors are negligible for detecting line-of-sight movements using TRI systems. Repositioning errors in the line of sight of the TRI were measured in this research. As a matter of fact, errors in the same order of magnitude as the measured displacements were measured. Therefore, the possibility of incorporating TRI repositioning errors into the TRI software should be investigated.

The compact TLS used in this research was handheld due to limitations of space in the tower of the TRI. The possibility of attaching a compact TLS to the tower of the TRI should be investigated. This will allow for better precision during measurement campaigns.

Table A.1. TRI results of the second measurement campaign (modified from Gómez, 2018).

ΔRDS Disp.	0.00 (mm)	0.05 (mm)	0.10 (mm)	0.25 (mm)	0.50 (mm)	1.00 (mm)	2.00 (mm)	5.00 (mm)
TRI Measured Disp.	disp (mm)	disp (mm)	disp (mm)	disp (mm)	disp (mm)	disp (mm)	disp (mm)	disp (mm)
Pseudorock	0.10	-0.05	-0.13	-0.26	-0.64	-1.03	-1.97	0.06
106 cm target	-0.15	0.11	-0.36	-0.37	-0.20	-1.19	-1.85	-5.31
cr1	0.00	0.00	0.00	0.00	0.00	0.00	0.00	0.00
Pseudorock	-0.14	-0.16	-0.02	-0.30	-0.57	-1.06	-2.10	-0.05
61 cm target	-0.08	-0.16	0.01	-0.12	-0.28	-0.67	-1.60	-4.82
cr1	0.00	0.00	0.00	0.00	0.00	0.00	0.00	0.00
Pseudorock	0.00	-0.08	-0.07	-0.28	-0.53	-0.98	-2.00	-0.12
46 cm target	-0.04	-0.09	-0.14	-0.23	-0.50	-0.94	-1.86	-5.12
cr1	0.00	0.00	0.00	0.00	0.00	0.00	0.00	0.00
Pseudorock	0.18	0.08	0.11	-0.15	-0.53	-0.97	-1.83	-0.09
20 cm target	0.16	0.27	0.11	0.03	-0.12	-0.40	-0.84	-6.75
cr1	0.00	0.00	0.00	0.00	0.00	0.00	0.00	0.00

Table A.2. Results of measured displacements greater than one quarter the wavelength of the TRI. The 61x61 cm target was positioned at an offset distance of 42 m (modified from Gómez, 2018).

ΔRDS Displacements (mm)	7.000	9.000	18.000	18.000	26.000	36.000
Wrapped displacements (mm)	-2.27	-0.79	-1.64	-2.05	-9.49	-1.77
cr1 (stationary near corner reflector)	0.00	0.00	0.00	0.00	0.00	0.00
Laser displacement (mm)	-7.51	-9.79	-18.73	-16.96	-25.21	-34.99
Phase integer number	0	1	2	1	2	4
Total displacements	-2.30	-9.40	-18.80	-10.60	-26.70	-36.20
Difference (laser - GBIR)	-5.21	-0.39	0.07	-6.36	1.49	1.21

Table A.3. Results of the measured displacements of the 61x61 cm target using the TRI (modified from Gómez, 2019).

LOS disp. (mm)

Test	B	C	C	E	F	G	H	I	J	K	M	N	O	P	Q	R
Reading No	01	02	03	04	05	06	07	08	09	10	11	12	13	14	15	16
Target	-0.49	-1.46	-1.41	-1.72	2.28	-3.45	2.06	-2.96	-2.27	-0.34	1.22	-0.70	-1.08	-0.39	-1.81	-0.37
Target alt. wrap	8.01	7.04	7.09	6.78	-6.22	5.05	-6.44	5.54	6.23	8.16	-7.28	7.80	7.42	8.11	6.69	8.13
cr1	0.04	-0.72	-0.38	0.35	-0.31	0.20	-0.05	-0.03	-0.05	-0.29	-0.31	-0.30	-0.32	-0.31	-0.31	-0.32

Sigma (mm)

Test	B	C	C	E	F	G	H	I	J	K	M	N	O	P	Q	R
Target	0.03	0.04	0.06	0.06	0.07	0.09	0.05	0.09	0.09	0.02	0.04	0.03	0.05	0.02	0.08	0.02
cr1	0.03	0.04	0.06	0.06	0.07	0.09	0.05	0.09	0.09	0.02	0.04	0.03	0.05	0.02	0.08	0.02
Non-moving pixels	0.09	0.11	0.12	0.14	0.14	0.18	0.14	0.16	0.14	0.10	0.13	0.12	0.12	0.11	0.14	0.10

LOS disp. (atmosphere-corrected using cr1)

Test	B	C	C	E	F	G	H	I	J	K	M	N	O	P	Q	R
Target	-0.53	-0.74	-1.03	-2.08	2.59	-3.65	2.11	-2.93	-2.21	-0.05	1.53	-0.40	-0.76	-0.08	-1.50	-0.06
target alt. wrap	7.97	7.76	7.47	6.42	-5.91	4.85	-6.39	5.57	6.29	8.45	-6.97	8.10	7.74	8.42	7.00	8.44

LiDAR disp. (mm) (provided by S&T)

Test	B	C	C	E	F	G	H	I	J	K	M	N	O	P	Q	R
Target	-1.00	-1.60	0.10	-2.10	-6.60	-12.50	-15.90	-19.30	-28.10	-0.70	-9.40	-9.90	-18.70	-26.90	-35.90	-1.70

total disp. (mm) adding integer number of cycles from LiDAR

Test	B	C	C	E	F	G	H	I	J	K	M	N	O	P	Q	R
Target	-0.53	-0.74	-1.03	-2.08	-14.41	-12.15	-14.89	-19.93	-27.71	-0.05	-15.47	-8.90	-17.76	-25.58	-35.50	-0.06
Phase integer	0	0	0	0	-1	-1	-1	-2	-3	0	-1	-1	-2	-3	-4	0

BIBLIOGRAPHY

Abellán, A., M. Jaboyedoff, T. Oppikofer, and J. M. Vilaplana. 2009. "Detection of millimetric deformation using a terrestrial laser scanner: Experiment and application to a rockfall event." *Natural Hazards and Earth System Science* 9 (2): 365-72.

Alba, M., G. Bernardini, A. Giussani, P. P. Ricci, F. Roncoroni, M. Scaioni, P. Valgoi, and K. Zhang. 2008. "Measurement of dam deformation by terrestrial interferometric techniques." *The International Archives of the Photogrammetry, Remote Sensing and Spatial Information Sciences*. Vol. XXXVII. Part B1. Beijing.

Alzahrani, Ali Abdullah M. 2017. Detection of mine roof failure using inexpensive LIDAR technology. Missouri University of Science and Technology.

Aqeel, Adnan Mohammed. 2012. "Measuring the orientations of hidden subvertical joints in highways rock cuts using ground penetrating radar in combination with LIDAR." PhD dissertation, Missouri University of Science and Technology.

Bosch GLR 825. August 21, 2018. https://www.boschtools.com/us/en/boschtools-ocs/laser-measuring-glr-825-35119-p/.

Boyko, Kenneth. 2014. *LiDAR Software Manual*. Missouri University of Science and Technology.

Caduff, Rafael, Fritz Schlunegger, Andrew Kos, and Andreas Wiesmann. 2015." A review of terrestrial radar interferometry for measuring surface change in the geosciences." *Earth Surface Processes and Landforms* 40 (2): 208-28.

Crosetto, M., O. Monserrat, G. Luzi, M. Cuevas-Gonzalez, and N. Devanthery. 2014. "A noninterferometric procedure for deformation measurement using GB-SAR imagery." *IEEE Geoscience and Remote Sensing Letters* 11 (1): 34-8

Daud, R. A. A., and A. F. Abdulla. 2016. "Accuracy assessment of Terrestrial Laser Scanning (TLS), Airborne Light Detection and Ranging (LiDAR), and Interferometric Aperture Synthetic Radar (InSAR) in agriculture." *International Conference on Agricultural and Food Engineering*, 23-25 August 2016.

Davis, Michael. 2011. "Radar frequencies and waveforms." *12th Annual International Symposium on Advanced Radio Technologies*.

Faro Focus 3D X130. March 13, 2019. https://knowledge.faro.com/Hardware/3D_Scanners/Focus/User_Manuals_for_the_Focus3D_X_130_or_130_HDR.

Fröhlich, C., and M. Mettenleiter. 2004. "Terrestrial Laser Scanning New Perspectives in 3D Surveying." *International Archives of Photogrammetry, Remote Sensing and Spatial Information Services*, Vol XXXVI-8/W2, 7-13.

Gilliam, Joseph T. 2015. "Controlled study of ground-based interferometric radar for rockfall hazard monitoring." MS thesis, University of Missouri-Columbia.

Gómez, Francisco. March 20, 2018. Re: GPIR Testing. [email].

Gómez, Francisco. June 4, 2018. 2018. Results of the experiments in the park for known displacements. [email]

Gómez, Francisco. June 27, 2018. 2018. Blind test results. [email]

Gómez, Francisco. February 12, 2019. Results. [email]

Hecht, Jeff. 2008. *Understanding lasers: An entry-level guide*. 3rd ed. Vol. 21. Piscataway, N.J; Hoboken, N.J. IEEE Press.

Heritage, George, and Andy Large. 2009. *Laser scanning for the environmental sciences*. US: Wiley-Blackwell.

Hoeksman, Gerben. 2007. "Antenne karakteristiek met openingshoek."

Intrieri, Emanuele, Giovanni Gigli, Luca Lombardi, Federico Raspini, Teresa Salvatici, and Giovanni Bertolini. 2016. "Integration of ground-based interferometry and terrestrial laser scanning for rockslide and rockfall monitoring." *Rendiconti Online Della Società Geologica Italiana* 41: 243-6.

Jenkins, Wyatt S. 2013. "Evaluation of ground-based interferometric radar for civil engineering applications." MS thesis, University of Missouri, Columbia.

Kromer, R. A., Antonio Abellán, D. J. Hutchinson, Matt Lato, M. Chanut, L. Dubois, and M. Jaboyedoff. 2017. "Automated terrestrial laser scanning with near real-time change detection - monitoring of the séchilienne landslide." *Earth Surface Dynamics Discussions*, 1-33.

Kromer, Ryan, Antonio Abellán, D. Hutchinson, Matt Lato, Tom Edwards, and Michel Jaboyedoff. 2015. "A 4D filtering and calibration technique for small-scale point cloud change detection with a terrestrial laser scanner." *Remote Sensing* 7 (10): 13029-52.

Leica Scan Station P40. March 13, 2019. https://leica-geosystems.com/en-US/products/laser-scanners/scanners/leica-scanstation-p40--p30.

Lingua, A., D. Piatti, and F. Rinuado. 2008. "Remote monitoring of a landslide using integration of GB-InSAR and LiDAR techniques." *The International Archives of the Photogrammetry, Remote Sensing and Spatial Information Sciences*. Vol. XXXVII. Part B1. Beijing.

Maerz, N. H., Kenneth J. Boyko, B. J. Hill, Benjamin J. Herries, M. Hopkins, and C. Lu. 2016. "Displacement measurements of slow moving landslide using sub-mm LiDAR scanning." *Proceedings of the 67th Highway Geology Symposium*, July 2016, Colorado Springs, Colorado.

Miles, Charels Prentice. 2018. Personal communication. [email]

Monserrat, O., M. Crosetto, and G. Luzi. 2014. "A review of ground-based SAR interferometry for deformation measurement." *ISPRS Journal of Photogrammetry and Remote Sensing* 93: 40-8.

Noyafa NF-2680. August 21, 2018. http://www.noyafa.com/show.php?contentid=100.

Otoo, James Nii Aboh. 2012. "Surface expressions of discontinuities, and the estimation of their 3-D orientations using combined LiDAR and optical imaging." PhD diss., Missouri University of Science and Technology.

Oxford Dictionaries, s.v. "lidar," accessed July 3, 2018, https://en.oxforddictionaries.com-/definition/lidar.

Richards, M. A. 2014. *Fundamentals of radar signal processing*. 2nd ed. Chicago, Ill: McGraw-Hill Education LLC.

Richards, Mark A. Scheer, James A. Holm, William A. 2010. *Principles of Modern Radar, Volume I - Basic Principles.* SciTech Publishing.

Ring, J. 1963. "The Laser in Astronomy". *New Scientist*. 672–673.

Rohrbaugh, Nathan Bradley. 2015. A new technique for modeling the geomorphology of a slow moving, soft-slope landslide using terrestrial LiDAR.Missouri University of Science and Technology.

Rosenblad, B. L., Francisco Gómez, J. Erik Loehr, and Joseph Gilliam. 2016. "Observations of Rockfall and Earth Slope Movements using Ground-Based Interferometric Radar." *Proceedings of the 67th Highway Geology Symposium*, July 2016, Colorado Springs, Colorado.

Rosser, N. J., D. N. Petley, M. Lim, S. A. Dunning, and R. J. Allison. 2005. "Terrestrial laser scanning for monitoring the process of hard rock coastal cliff erosion." *Quarterly Journal of Engineering Geology & Hydrogeology* 38 (4): 363-75.

Tapete, Deodato, Nicola Casagli, Guido Luzi, Riccardo Fanti, Giovanni Gigli, and Davide Leva. 2013. "Integrating radar and laser-based remote sensing techniques for monitoring structural deformation of archaeological monuments." *Journal of Archaeological Science* 40 (1): 176-89.

Truckle, Timothy. 2008. Sidelobes.

Werner C, A. Wiesmann, T. Strozzi, A. Kos, R. Caduff, U. Wegmüller. 2012. "The GPRI multi-mode differential interferometric radar for ground-based observations." *Proceedings of the 9th European Conference on Synthetic Aperture Radar*; 304–307.

Wujanz, D., F. Neitzel, H. P. Hebel, J. Linke, and W. Busch. 2013. "Terrestrial radar and laser scanning for deformation monitoring: First steps towards assisted radar scanning." *ISPRS Annals of the Photogrammetry*: 325-30.

VITA

Ricardo Javier Romero-Ramírez was born in Mayagüez, Puerto Rico, USA. After earning his high school diploma from the Presbyterian College Pablo Casasús in Mayagüez, Puerto Rico, he received a Bachelor of Science in civil engineering in 1993 and a Master of Engineering in civil engineering (geotechnical engineering) in 1996 from the University of Puerto Rico at Mayagüez. After this, he worked for five years as a geotechnical engineer with the Soils Engineering Office of the Puerto Rico Highway and Transportation Authority. Then he attended the University of Missouri at Columbia where he received the degree of Doctor of Philosophy in civil engineering (geotechnical engineering) in December 2003. In 2004, he returned to Puerto Rico to work for the Soils Engineering Office of the Puerto Rico Highway and Transportation Authority, and in 2009 he earned the position of Chief of the Office. He later became interested in geological engineering (rock mechanics) and began his studies as a distance education student in geological engineering in 2014 at the Missouri University of Science and Technology. After being a distance student for three years, he moved to Rolla to begin his research. He received the degree of Doctor of Philosophy in geological engineering (rock mechanics) in May 2019.